Study of Neutrino Oscillation in the Long Baseline Neutrino Experiment

Shuei Yamada

February 18, 2003

Abstract

The KEK to Kamioka long baseline neutrino oscillation experiment (K2K) took data successfully both at KEK and Super-Kamiokande to investigate neutrino oscillation for the period from Jun 1999 to July 2001. Accumulated are 4.79×10^{19} protons on target at the 12 GeV-PS.

The expected number of events in Super-Kamiokande at 250 km from the target is estimated by extrapolating the number of observed events in the 1kt detector at 300 m from the target. It is estimated to be $80.6 \pm 0.3(stat.)^{+4.8}_{-4.9}(syst.)$ for fully-contained events during the whole run.

In Super-Kamiokande, the neutrino events are clearly isolated in the beam arrival time matching perfectly with the beam spill time of PS. The timing synchronization of Super-Kamiokande clock and the accelerator clock is carried out by using GPS and confirmed by an atomic clock for their relative accuracy. A total of 56 fully-contained events are observed during the whole run. They are background free.

Comparing the expectation and the observation at Super-Kamiokande, the probability of null-oscillation hypothesis was obtained to be 0.7%.

The $\nu_\mu \leftrightarrow \nu_\tau$ oscillation analysis is performed using 30 fully-contained 1-ring muon-like events. The best fit was obtained at $(\sin^2 2\theta, \Delta m^2) = (1.00, 2.7 \times 10^{-3}\text{eV}^2)$. This is consistent with the set of parameters suggested by atmospheric neutrinos.

Acknowledgment

I would like to express my great appreciation to my adviser, Prof. Yoichiro Suzuki, for introducing me to elementary particle physics and supported me on many occasions throughout my graduate studies. He gave me the chance to participate in this experiment from the first stage. I wish to extend my appreciation to Prof. K.Nishikawa, Prof. K.Nakamura, Prof. Y.Totsuka, Prof. M.Sakuda, Prof. C.K.Jung and Prof. R.J.Wilkes. Their management of K2K experiment enables me to accomplish my works.

I would like to express my gratitude to all the K2K collaborators and all the Super-Kamiokande collaborators for sharing daily work of data-taking, help with the experiment and analysis. I am particularly indebted to Prof. K.Kaneyuki for all his close work with me. He kindly helped me on many occasions.

I am deeply grateful to K2K staffs, Prof. Y.Itow, Prof. T.Kobayashi, Prof. K.Scholberg, Dr. Y.Hayato, Dr. T.Hasegawa, Dr. J.Hill and Mr. H.G.Berns for their expertise, comments and insights. I would express my thanks to Prof. T.Nakaya, Dr. M.Miura, Dr. S.Mine, Dr. T.Ishida, Dr. T.Ishii and Dr. Y.Oyama for helpful advice and guidance. Prof. T.Kajita, Prof. M.Nakahata, Dr. A.C.Suzuki, Dr. Y.Takeuchi, Dr. Y.Fukuda, Dr. S.Moriyama, Dr. Y.Koshio, Dr. M.Shiozawa, Dr. Y.Obayashi and Dr. A.Ichikawa gave me many fine suggestions and discussions.

My thanks go to Mr. S.Nakayama, Dr. J.Kameda, Dr. N.Sakurai, Dr. T.Toshito, Dr. T.Namba, Dr. K.Kobayashi, Dr. C.Saji, Mr. Y.Kobayashi, Mr. K.Nitta, Mr. M.Ishitsuka, Mr. Y.Gando, Mr. C.Mitsuda and all the SK graduate students for suggestions, physics discussions and life in Kamioka. Dr. Maruyama, Dr. Kohama, Dr. T.Inagaki, Dr. M.Yoshida, Mr. T.Kadowaki, Mr. T.Iwashita, Mr. I.Kato, Mrs. H.Yokoyama and all the K2K graduate students gave me their expertise, advice and friendship. They always cared about me and assisted with my studies.

I am deeply grateful to KEK-PS accelerator group and beam-channel group, for their hard work on providing stable neutrino beam. I also thank the cooperation of Kamioka Mining and Smelting Company.

Finally, I gratefully acknowledge my family and my best friends, for a lot of encouragement and support throughout my physicist life.

Contents

Chapter 1

Introduction

1.1 Neutrino Mass

In the standard model of the elementary particles, neutrinos are assumed to be massless leptons[1, 2, 3]. Three different neutrinos are expressed as flavor eigenstates, ν_e, ν_μ, and ν_τ, which are identified by the correspondence to e, μ, and τ in the weak interaction.

Direct measurements of neutrino mass have been performed by precise measurement of decay kinematics. They have only succeeded in giving upper limits. The most sensitive measurement of the ν_e mass was the measurement of the end point of the electron energy spectrum of tritium beta decays. The end point must be shifted to a lower value if ν_e has a finite mass. Various experiments have been performed, giving the upper limit of several eV. The mass limit of m_{ν_e} is also estimated from the spread of the arrival time of neutrinos from Supernova-1987A, to be a few 10 eV [4]. The best limit on ν_μ mass of 170 keV was obtained from muon momentum measurement of the pion decay performed by PSI group [5]. The ν_τ mass limit was obtained by the ALEPH collaboration. Results from two kinds of tau decay, $\tau \rightarrow 3\pi\nu_\tau$ and $\tau \rightarrow 5\pi(\pi^0)\nu_\tau$, are combined to obtain the limit of 18.2 MeV at 95% confidence level (C.L.). The best upper limit at present on the mass of the three neutrino species are summarized in Table 1.1

1.2 Neutrino Oscillation

Neutrino oscillation is a flavor changing phenomenon. It is caused by the mixing of the flavor eigenstate and the mass eigenstate, when the neutrino has a non-degenerate mass.

Neutrino	Mass limit (by PDG[4])	Experiment
ν_e	3 eV	^{3}Hβ decay
ν_μ	190 keV (90% C.L.)	pion decay
ν_τ	18.2 MeV (95% C.L.)	tau decay

Table 1.1: Present limit of neutrino mass.

For the two neutrinos case, the flavor eigenstates ν_α、ν_β can be described as following;

$$\begin{pmatrix} \nu_\alpha \\ \nu_\beta \end{pmatrix} = \begin{pmatrix} \cos\theta & \sin\theta \\ -\sin\theta & \cos\theta \end{pmatrix} \begin{pmatrix} \nu_1 \\ \nu_2 \end{pmatrix} \equiv U \begin{pmatrix} \nu_1 \\ \nu_2 \end{pmatrix}, \tag{1.1}$$

where ν_1, ν_2 are the mass eigenstates and θ is the mixing angle. While neutrinos are generated via weak interactions in the flavor eigenstats, their time evolution of the state is described as mass eigenstates in following Schrödinger equation:

$$i\frac{d}{dt}\begin{pmatrix} \nu_\alpha \\ \nu_\beta \end{pmatrix} = H \begin{pmatrix} \nu_\alpha \\ \nu_\beta \end{pmatrix}, \tag{1.2}$$

where H is Hamiltonian for free neutrinos. Since the states ν_i have common momentum p, according to the conservation of momentum, this equation can be solved as following:

$$\begin{pmatrix} \nu_1(t) \\ \nu_2(t) \end{pmatrix} = \begin{pmatrix} e^{-iE_1t} & 0 \\ 0 & e^{-iE_2t} \end{pmatrix} \begin{pmatrix} \nu_1(0) \\ \nu_2(0) \end{pmatrix}, \tag{1.3}$$

where $E_i = \sqrt{p^2 + m_i^2}$ are energy eigenstates. Thus the time evolution of flavor eigenstates can be expressed as following:

$$\begin{pmatrix} \nu_\alpha(t) \\ \nu_\beta(t) \end{pmatrix} = U \begin{pmatrix} e^{-iE_1t} & 0 \\ 0 & e^{-iE_2t} \end{pmatrix} U^{-1} \begin{pmatrix} \nu_\alpha(0) \\ \nu_\beta(0) \end{pmatrix} \tag{1.4}$$

Assume a neutrino is generated as ν_α, its surviving probability at time t, or at distance L, is given as following:

$$\begin{aligned} P(\nu_\alpha \to \nu_\alpha) &= 1 - \sin^2 2\theta \sin^2\left(\frac{\Delta m^2 L}{4p}\right) \\ &= 1 - \sin^2 2\theta \sin^2\left(\pi\frac{L}{L_\nu}\right) \end{aligned} \tag{1.5}$$

where $\Delta m^2 \equiv m_2^2 - m_1^2$ and relativistic approximation $E_i \simeq p + m_i^2/2p$ is used. The oscillation length, L_ν, is defined by neutrino momentum p and Δm^2,

$$L_\nu = \frac{4\pi p}{\Delta m^2} \tag{1.6}$$

$$= 2.48\frac{p[\mathrm{GeV/c}]}{\Delta m^2[\mathrm{eV^2/c^4}]}km. \tag{1.7}$$

The observation of neutrino oscillation proves the existence of different mass eigenstates of neutrinos and the existence of mixing between the mass eigenstate and flavor eigenstate. A long baseline L and low neutrino energy E enables a search of the oscillation and a investigation of the finite Δm^2 much less than eV^2.

	exposure (kt-yr)	R
Kamiokande (sub-GeV)	8.2 kt-yr	$0.60^{+0.06}_{-0.05}$(stat.) ±0.05(syst.)[6]
Kamiokande (multi-GeV)	8.2 kt-yr (FC) 6.0 kt-yr (PC)	$0.57^{+0.08}_{-0.07}$(stat.) ±0.07(syst.)[6]
IMB	7.7	0.54 ±0.05(stat.) ±0.012(syst.)[7]
Super-Kamiokande (sub-GeV)	91.6 kt-yr	0.638 ±0.016(stat.) ±0.050(syst.) [12]
Super-Kamiokande (multi-GeV)	91.6 kt-yr	0.658 $^{+0.030}_{0.028}$(stat.) ±0.078(syst.) [12]
Fréjus	2.0 kt-yr	1.00 ±0.15(stat.) ±0.08(syst.)[9]
NUSEX	0.74 kt-yr	0.99 $^{+0.35}_{-0.25}$[10]
Soudan-2	3.9 kt-yr	0.64 ±0.11(stat.) $^{+0.06}_{-0.05}$(syst.)[11]

Table 1.2: Summary of the measured R values by various atmospheric neutrino experiments. The definition of R is described in the text.

1.3 Atmospheric Neutrino Experiments

Atmospheric neutrinos are produced in decays of pions and kaons generated by the interaction between primary cosmic rays and the upper atmosphere. The energy spectrum of these neutrinos is peaked at about 1 GeV and extends to hundreds of GeV. Their flight length spreads from 15km, for neutrinos produced in the zenith, to 13,000 km, for those produced in the nadir. The measurement of atmospheric neutrinos is sensitive to the neutrino oscillation parameter Δm^2 down to 10^{-4} eV^2.

The main production process of neutrinos around sub-GeV region is a sequence of pion decay as following:

$$\pi^\pm \rightarrow \mu^\pm \overset{(-)}{\nu}_\mu \qquad (1.8)$$

$$\mu^\pm \rightarrow e^\pm \overset{(-)}{\nu}_\mu \overset{(-)}{\nu}_e \qquad (1.9)$$

Thus, the ideal flux ratio $(\nu_\mu + \bar{\nu}_\mu)/(\nu_e + \bar{\nu}_e)$ is 2. It is predicted with a 5% uncertainty, while the uncertainty in the prediction of the total flux of atmospheric neutrino is ∼ 20%.

This ratio has been measured by several underground experiments. Table 1.2 summarizes results of underground water Čerenkov detectors (Kamiokande[6], IMB[7] and Super-Kamiokande[12]) and iron-calorimeter detectors (Fréjus[9], NUSEX[10] and Soudan-2[11]). These measurements are compared to expectations based on Monte Carlo simulations, in order to cancel out systematic uncertainties, as following:

$$R \equiv \frac{(N_\mu/N_e)_{obs}}{(N_\mu/N_e)_{MC}}, \qquad (1.10)$$

where N_μ is the number of muon-like events and N_e is the number of electron-like events. Kamiokande, IMB, Super-Kamiokande and Soudan-2 reported that R was significantly smaller than unity, while Fréjus and NUSEX reported that is was consistent with unity.

Furthermore, Kamiokande and Super-Kamiokande measured the zenith angle dependence, and the Super-Kamiokande experiment reported evidence for oscillations of the atmospheric neutrinos in 1998[8]. Figure 1.1 shows zenith angle distributions for μ-like events, e-like events and multi-ring events for sub-GeV and multi-GeV sample, upward stopping muons and upward through-going muons, observed in Super-Kamiokande[12]. "Sub-GeV (multi-GeV)" indicates the events in which their visible energy is less (more) than 1.33 GeV. Upward-going neutrinos are produced in the nadir and travel more than 10,000 km through the earth, while the downward-going neutrinos travel a few tens of km from the zenith. Since the observed charged particles generally conserve the induced neutrinos' direction, the zenith angle of the observed Čerenkov ring distributions corresponds to the baseline L in Equation 1.5.

The upward-going muon is produced in an energetic ν_μ interactions in the rock underneath the detector. The upward stopping muon crosses the detector partially and stops in the detector and the upward through-going muon pierces the whole detector. The mean energy of their parent neutrinos are typically 10 GeV for upward stopping muons and 100 GeV for through-going muons.

The result of the zenith angle distributions show deficits in upward going μ-like events and upward going muons, while e-like events are consistent with prediction. The deficits are well explained by the $\nu_\mu \leftrightarrow \nu_\tau$ oscillation in the all energy ranges. Figure 1.2 shows the allowed region of parameters $(\sin^2 2\theta, \Delta m^2)$. The 90% C.L. allowed region is:

$$\sin^2 2\theta > 0.92$$
$$1.6 \times 10^{-3} < \Delta m^2 < 3.9 \times 10^{-3}\mathrm{eV}^2$$

The KEK to Kamioka long baseline neutrino oscillation experiment investigates neutrino oscillation with an almost pure ν_μ beam produced by accelerator. The mean neutrino energy of 1.3 GeV and the baseline of 250 km is suitable to confirm the parameter region suggested by atmospheric neutrino experiments.

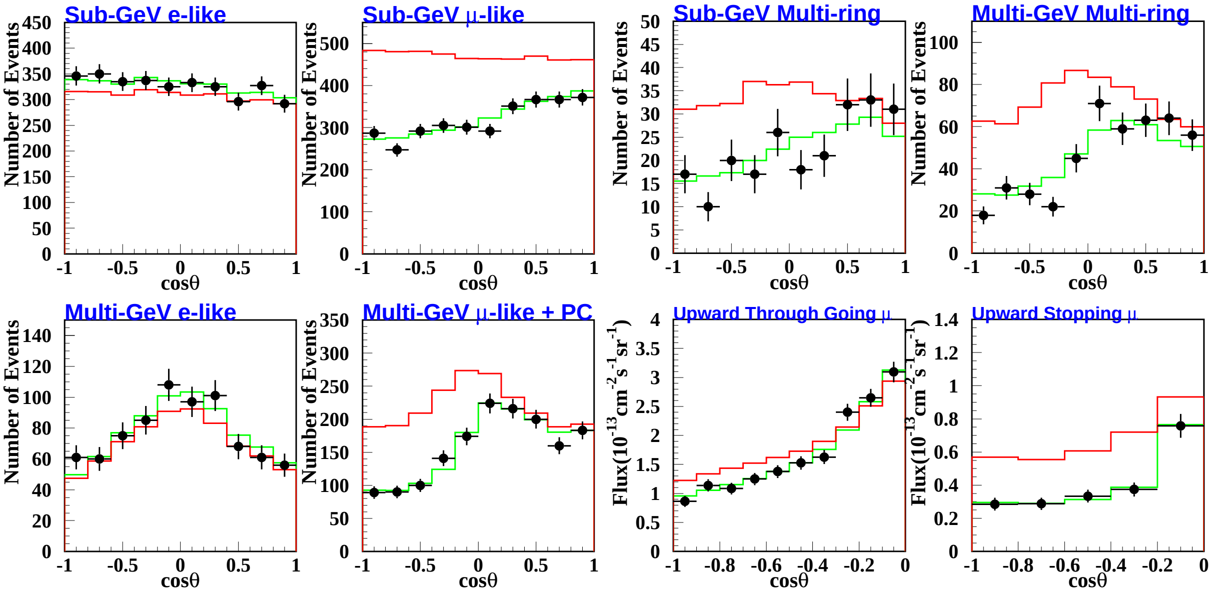

Figure 1.1: Zenith angle distributions for μ-like events, e-like events and multi-ring events for sub-GeV and multi-GeV sample, upward stopping muons and upward through-going muons, observed in Super-Kamiokande. A vertically upward particle has $\cos\theta = -1$ and a vertically downward particle has $\cos\theta = 1$. The red line shows the Monte Carlo expectation for the case of no oscillation. The green line shows the best fit for the case of $\nu_\mu \leftrightarrow \nu_\tau$ oscillations with the overall flux normalization fitted as a free parameter.

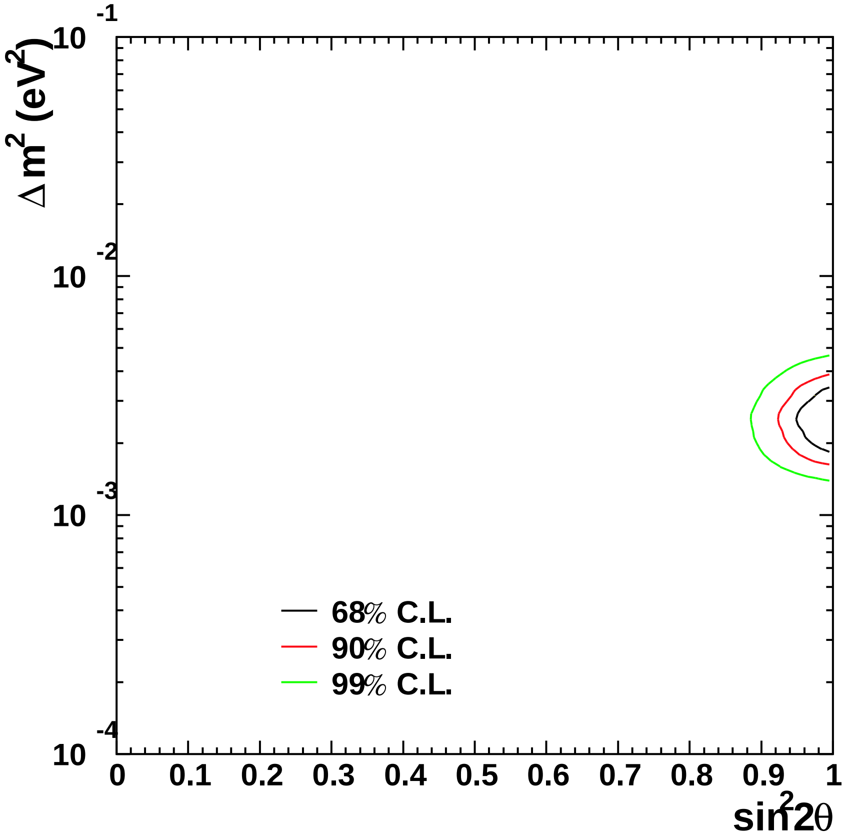

Figure 1.2: Allowed regions of parameters $(\sin^2 2\theta, \Delta m^2)$ in $\nu_\mu \leftrightarrow \nu_\tau$ oscillation. Black, red and green lines show the 68%, 90% and 99% C.L. allowed regions, respectively.

Chapter 2

Overview of the Experiment

The KEK to Kamioka long baseline neutrino oscillation experiment (K2K) is an accelerator-based experiment. K2K focuses on the experimental confirmation of the neutrino oscillation suggested by atmospheric neutrino experiments, using a neutrino beam whose spectrum and flavor are well known.

Muon neutrinos are generated at High Energy Accelerator Research Organization(KEK) and detected at Super-Kamiokande at 250 km distance (Figure 2.1). The neutrino beam is produced with pion decay in flight

$$\pi^+ \rightarrow \mu^+ \nu_\mu \ , \tag{2.1}$$

and its mean energy is 1.3 GeV. Pions are produced by hadron interaction between the high energy proton beam, which is provided by 12 GeV Proton Synchrotron in KEK (KEK-PS), and the target.

Thanks to 1.3 GeV mean neutrino energy and 250 km base line, K2K is sensitive to $\Delta m^2 \sim 10^{-3}\mathrm{eV}^2$ at large mixing angle, where atmospheric neutrino observation asserted that Δm^2 lies (Equation 1.5). Figure 2.2 shows the distortion of the expected neutrino spectrum at Super-Kamiokande for two typical oscillation parameters.

Beam Line Alignment and Beam Aiming

The neutrino beam line at KEK has to be constructed with a correct direction pointing precisely toward Super-Kamiokande. A survey using Global Positioning System (GPS) is performed for the line from the target to the detector [14]. The precision of the survey is better than 0.01 mrad, and the components in the near site are aligned with an accuracy better than 0.1 mrad.

The steering and monitoring of the neutrino beam are carried out by secondary beam monitors. The neutrino beam is controlled to aim at Super-Kamiokande within ±1 mrad accuracy (Section 3.3).

Timing Synchronization

Since it is impossible to connect KEK to Super-Kamiokande with cables, the GPS timestamp is used to identify beam neutrino event at Super-Kamiokande. With this method, selection bias is minimized in the analysis; for example, a low threshold can be applied and any lepton

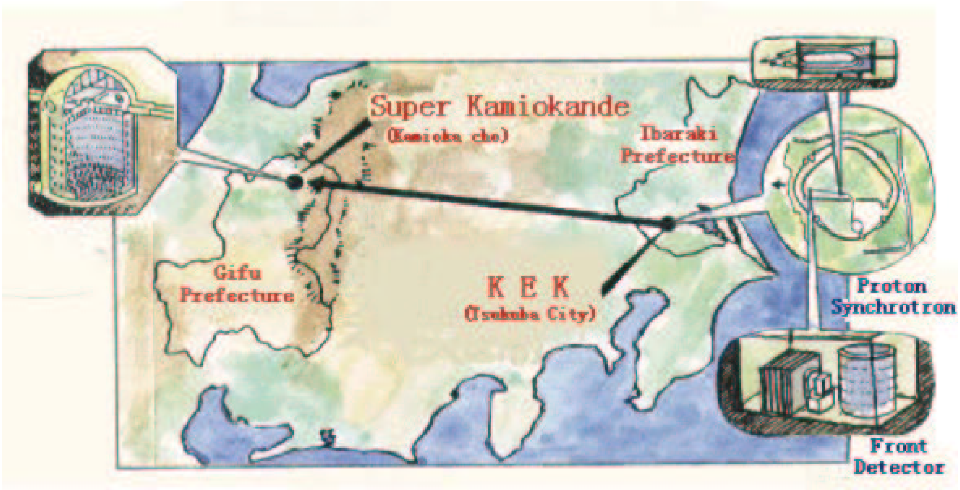

Figure 2.1: Layout of the experiment. Its baseline is 250 km.

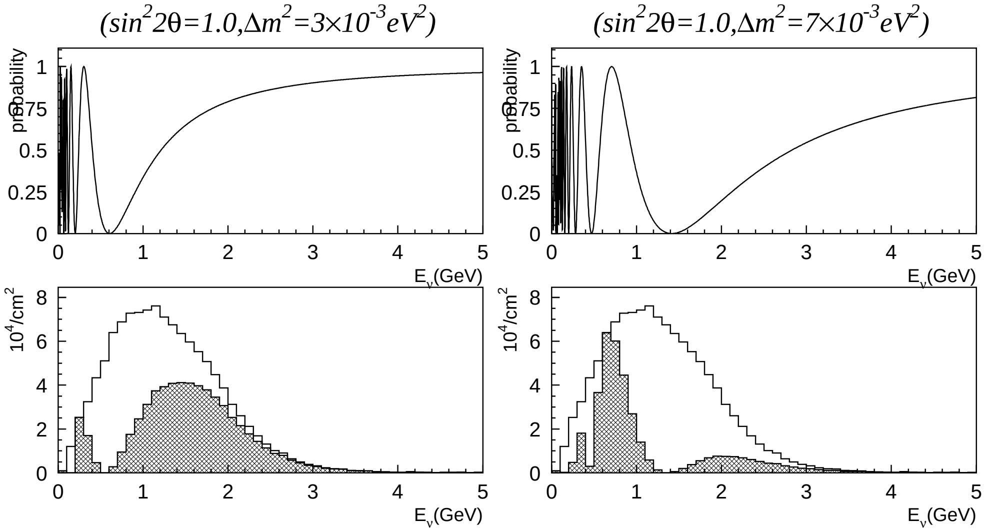

Figure 2.2: Distortion of the expected neutrino spectrum at Super-Kamiokande for two typical oscillation parameters. Left figures are for $(\sin^2 2\theta, \Delta m^2) = (1.0, 3.0 \times 10^{-3}\text{eV}^2)$ and right figures for $(1.0, 7.0 \times 10^{-3}\text{eV}^2)$. Top figures show the oscillation probability of neutrino oscillations as a function of energy. Bottom figures show the expected neutrino flux without neutrino oscillation (open histogram) and the oscillated flux (hatched histogram). Unit of the Y axis is number of neutrinos/cm^2.

direction can be allowed. GPS receivers are installed both at KEK and Super-Kamiokande for time synchronization. Beam firing time at KEK and each event time at Super-Kamiokande are recored. The GPS systems are summarized in Chapter 5.

Number of Expected Events in Super-Kamiokande

The study of the ν_μ disappearance is performed by comparing the number of observed and expected neutrino events in Super-Kamiokande. The expectation is based on near-site measurement and is given by the following formula:

$$N_{exp}^{SK} = N_{int}^{near} \cdot R^{far/near} \cdot \epsilon^{SK}, \tag{2.2}$$

where N_{int}^{near} is the number of neutrino interaction in the near detector, ϵ_{SK} is the event selection efficiency at Super-Kamiokande. $R^{far/ner}$ is the ratio of the neutrino event at the far site to that at the near site. It is given by:

$$R^{far/near} = \frac{\int \Phi^{SK} \cdot \sigma_{H2O} \cdot M_{SK} dE}{\int \Phi^{near} \cdot \sigma_{H2O} \cdot M_{near} dE}, \tag{2.3}$$

where $\Phi^{SK(near)}$ is the expected neutrino flux at Super-Kamiokande (near detector), σ_{H2O} is the neutrino cross section and $M_{SK(near)}$ is the fiducial mass of detector. The energy integrated ratio $R^{SK/near}$ is provided by a beam Monte Carlo simulation. It reproduces well the measurement of the pion momentum and divergence [15].

When the number of observed events has a deficit caused by the neutrino oscillation, the reduction probability depends on the neutrino energy as shown by Equation 1.5. Therefore, the distortion pattern in the measured ν_μ energy spectrum reflects the reduction probability as a function of energy. The oscillation parameters $(\sin^2 2\theta, \Delta m^2)$ can be determined by fitting the distortion pattern with Equation 1.5.

Brief History of the Experiment

The history of the K2K experiment is summarized in Table 2.1. Data has been taken stably since June 1999. In this thesis, the data set from June 1999 to July 2001, which corresponds to 4.79×10^{19} protons on target, is used.

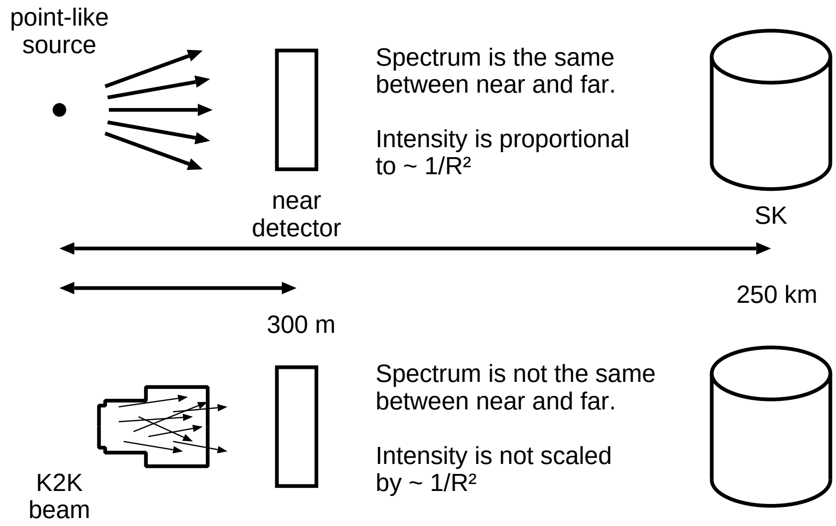

Figure 2.3: Schematic view of the K2K beam.

1995	Proposal [16] was approved at KEK.
	Components design was started.
1996	Construction work started.
1998	Detector components were placed.
	Construction work finished.
Feb., 1999	Proton beam was extracted to the target.
Mar., 1999	Horn operation started.
Jun., 1999	Started stable data taking with 200 kA. horn current.
Oct., 1999	Started stable data taking with 250 kA. horn current.

Table 2.1: History of the K2K experiment.

Chapter 3

Experimental Setup

K2K experiment consist of the neutrino beam line, near detector systems, and the 250 km far detector, Super-Kamiokande, as shown in Figure 3.1. Each component is described in the following section.

3.1 Neutrino Beam Line

3.1.1 KEK 12 GeV Proton Synchrotron

Neutrino beam is produced at the 12 GeV Proton Synchrotron(KEK-PS) in High Energy Accelerator Research Organization(KEK). The schematic view of the KEK-PS is shown in Figure 3.2. Its specifications are summarized in Table 3.1.

More than 6×10^{12} protons per cycle are accelerated up to 12 GeV. Each beam spill has 9 bunches in 1.1μsec spill length. The repetition cycle is 2.2 second.

3.1.2 Primary Proton Beam Transport Line

The proton beam is extracted to the neutrino beam-line from the "EP1" beam channel in a fast extraction mode, through the kicker, septum and bump magnets. Figure 3.2 shows the

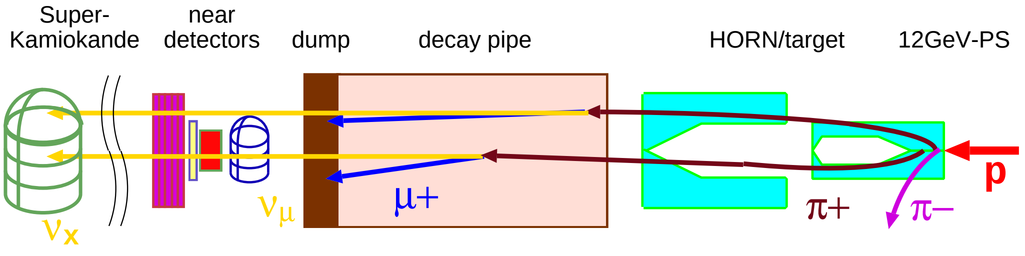

Figure 3.1: Schematic view of the K2K experiment.

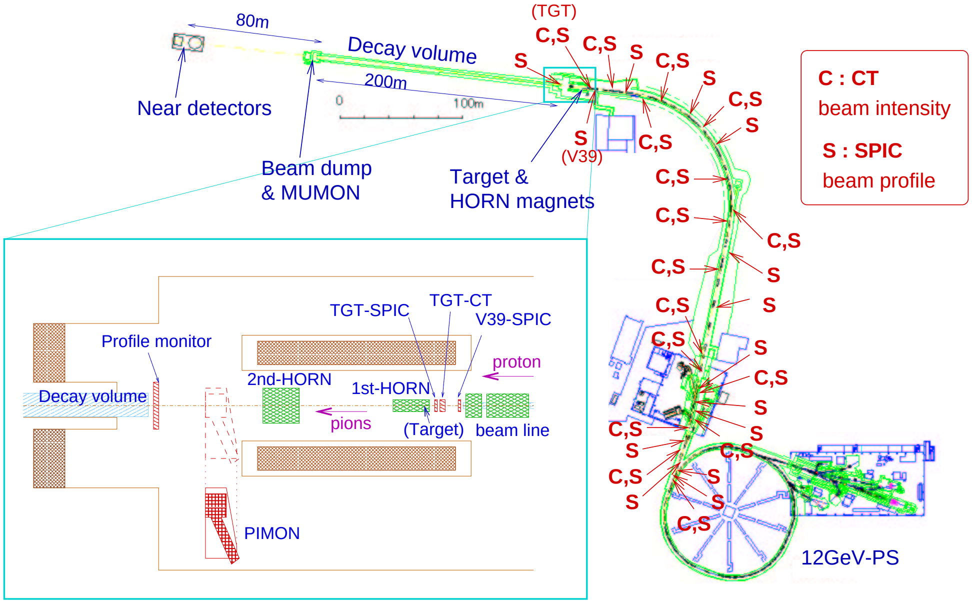

Figure 3.2: Schematic view of the 12 GeV KEK-PS and the neutrino beam line.

Accelerator components	Pre-injector (750 keV, Cockroft-Walton acc.) LINAC (40 MeV) BOOSTER (500 MeV) Main ring (12 GeV in kinetic energy)
Operation mode for K2K	fast extraction (single turn) to EP1-A
Typical intensity in main ring	7×10^{12} protons per spill
Typical intensity after extraction	6×10^{12} protons per spill
Typical intensity at target	5×10^{12} protons per spill
Number of bunches	9
Bunch repetition	about 120nsec
Total spill length	1.1μsec
Repetition cycle	2.2 sec

Table 3.1: Specification summary of KEK-PS for K2K experiment.

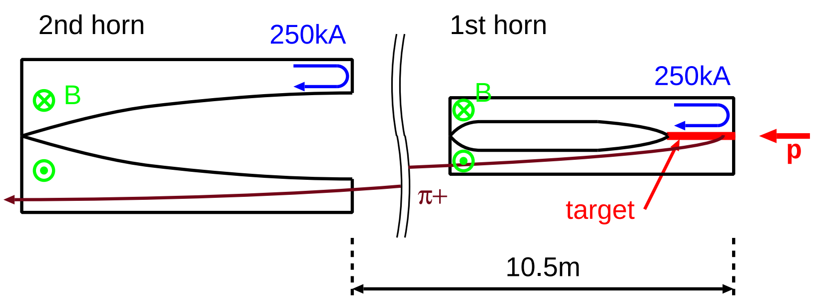

Figure 3.3: Schematic view of the horns.

location of the neutrino production beam line components and the near detector. The proton beam is extracted towards the north and is bent about 90 degrees to the West-North-West in the arc section, towards Super-Kamiokande.

The primary proton beam transport line is newly constructed for the experiment.

3.1.3 Target and Focusing Horn Magnet

Pions, the parent particles of neutrinos, are generated from the hadron interaction of 12 GeV protons at the target. A steering magnet is placed just before the target to point the proton beam to Super-Kamiokande *i.e.*, about 1° downward from the horizontal level. Two magnetic horns are used to efficiently focus the pion, as shorn in Figure 3.3. The first horn has dimensions of 2.37 m in length and 0.70 m in diameter, while the second horn has dimensions of 2.76 m in length and 1.65 m in diameter, located 8 m down stream of the first horn. The target is built in the first horn in order to focus pions more efficiently. It is a part of the first horn through which the current flows and is subject to a strong magnetic force. Its length is 66 cm. The diameter of the target was 20 mm in June 1999 and increased to 30 mm since November 1999, in order to strengthen the weakest part against the electromagnetic force. A Monte Carlo simulation shows that almost all protons interact in the target, including elastic scattering. The target and the horns are made of aluminum alloy, which is chosen for its low density, strength and electrical conduction. Both horns are kept thin as much as strength requirement permits.

The two horns are driven with a pulsed current. The peak current was 200 kA in June 1999 and 250 kA since November 1999 after the modification of the target. The pulse cycle is synchronized to the beam extraction of 2.2 sec repetition cycle. The total pulse length is about 3μsec (Figure 3.4).

The strength of the magnetic filed B(kGauss) in the air at R(cm) distance from the beam center is

$$B = \frac{I}{5.0 \cdot R}, \tag{3.1}$$

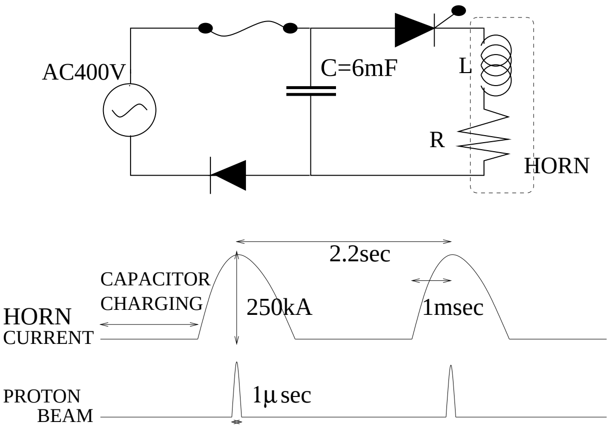

Figure 3.4: The pulse current supplied to the horn magnets.

where I is the current supplied to the horn magnets in unit of kA. Hence the maximum magnetic filed is 33 kGauss at the rod surface ($R = 1.5$ cm) at $I = 250$ kA. This magnetic field focuses the positive charged particles into forward direction and sweeps out the negative charged particles. Thus π^+ is selectively collected to get almost pure ν_μ. The two horns system enhances neutrino flux above 0.5 GeV by 22 times more than the bare target case as shown in Figure 3.5.

Magnetic field inside of the prototype of the first horn was measured using pickup coils [15, 18]. The radial distribution agrees with the designed value and the azimuthal symmetry is confirmed within the measurement error of 15%.

3.1.4 Decay Tunnel and Beam Dump

Pions are sent to the 200 m long decay tunnel in order to make pions decay to neutrinos efficiently. The decay tunnel starts at 19 m downstream from the target. Its diameter is 1.5 m in the first 10 m section, 2 m in the following 90 m section, and 3 m for the remaining 100 m section. Figure 3.6 shows the schematic view of the decay tunnel. The decay tunnel is filled up with helium gas at 1 atm in order to reduce pion absorption and pion production in the gas.

Finally all the charged particles are dumped at the end of the decay tunnel. The dump consists of 3.5 m thick iron block and 2 m thick concrete as shown in Figure 3.7. There are about 60 m of soil between the beam dump and the near detector, so that only the neutrino can pass through to the near detector.

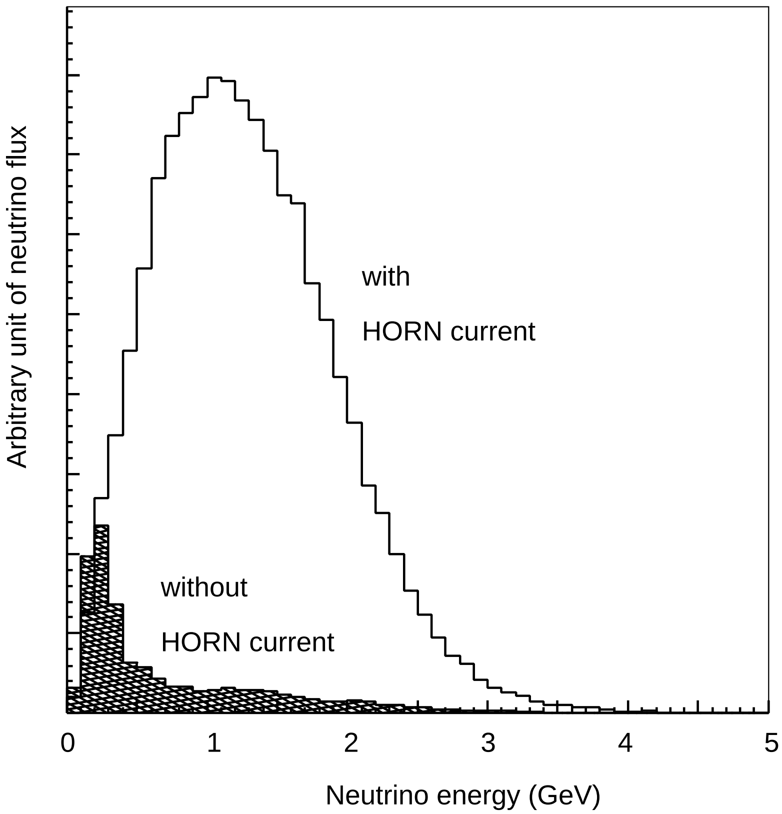

Figure 3.5: Effect of the horn system. The open histogram shows the MC simulated neutrino flux at Super-Kamiokande with 250 kA horn current, and the hatched one that for null horn current. The target diameter is 30mm.

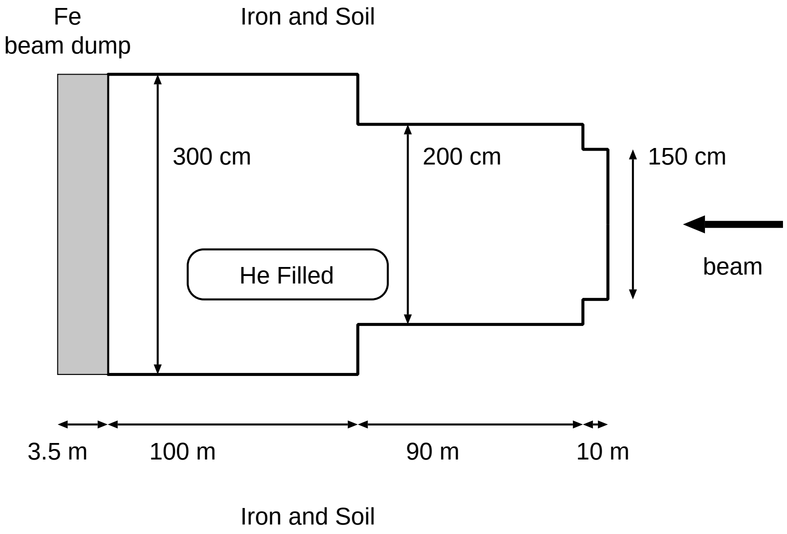

Figure 3.6: Schematic view of the decay tunnel.

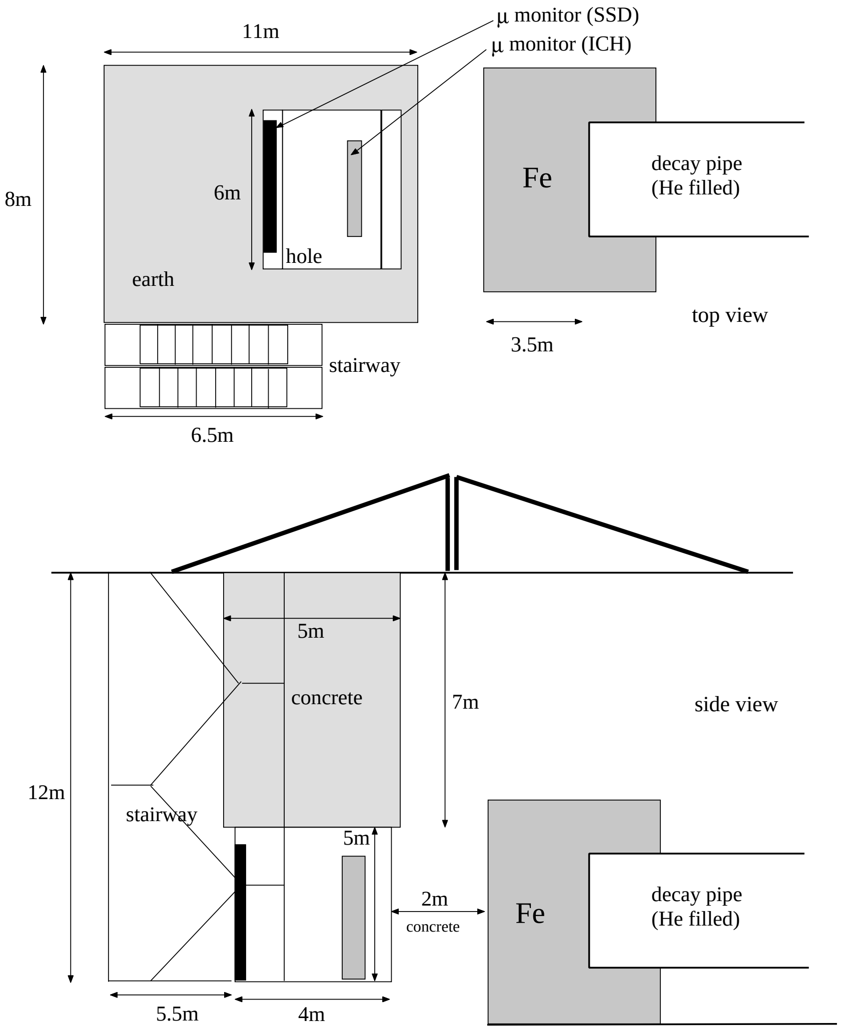

Figure 3.7: Schematic view of the beam dump. A muon monitor is installed in the beam dump.

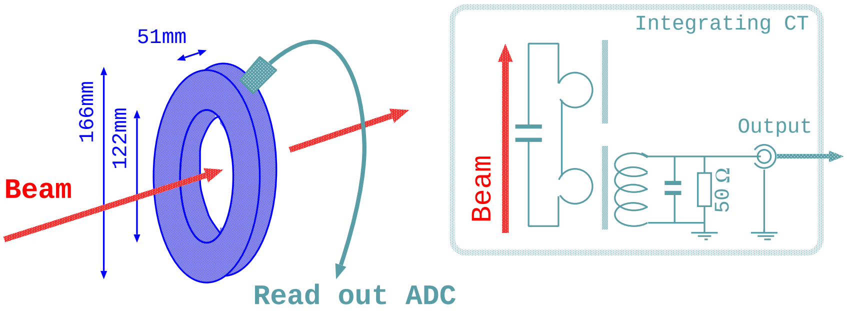

Figure 3.8: Schematic view of the CT.

3.2 Primary Beam Monitors

In order to monitor and control the proton beam, primary beam monitors are installed along the beam line. They are used to monitor proton beam intensity, transport efficiency and particle density distribution. Current Transformers (CTs) and Segmented Plates Ionization Chambers (SPICs) are employed and each of them is described below.

3.2.1 Current Transformer

CT is a kind of pick-up coil sensitive to the electric current. It is used as a proton beam intensity monitor. Figure 3.8 shows the schematic view of a CT. The inner diameter of a CT is about 12 cm, which is the same size as the beam pipe and large enough to contain the proton beam. There are 13 CTs installed in the primary beam line (Figure 3.2). The signals are lead to the control room several 10 m to 100 m far from the radiation area and connected to charge sensitive integrating ADCs. Figure 3.9 shows the typical signal shape of the proton beam.

Comparison among these CT values gives information of the transport efficiency. It is typically $\sim 85\%$ from the extraction point to the target. Each CT is calibrated by pulsed current and beam as well. Its error is within $\pm 10\%$. The CT located just before the target, named “TARGET-CT”, monitors the number of protons on the target (P.O.T.) delivered to generate the neutrino beam. Figure 3.10 shows the accumulated number of P.O.T. since June 1999 which were delivered by KEK-PS.

3.2.2 Segmented Plates Ionization Chamber

SPIC is an ionization chamber with segmented anode (Figure 3.11) to measure the particle density distribution. There are 28 SPICs installed in the beam line (Figure 3.2).

A SPIC consists of three copper sheets. The central one is for the cathode plane, and the outer ones are for horizontal and vertical readout anode planes. Since the proton beam directly hits this chamber, thus the copper is as thin as possible, namely, 28 μm. The gap is filled with helium gas. Out of 28 chambers, 26 have 32 channels with 5 mm pitch for both x and y readout, the chamber just before the target has 32 channels with 1.27 mm pitch for both x and y readout, and the one before the decay pipe, named “P/PI”, has 192 and 160 channels with 20 mm pitch for horizontal and vertical projection. The signals are read by charge sensitive ADCs.

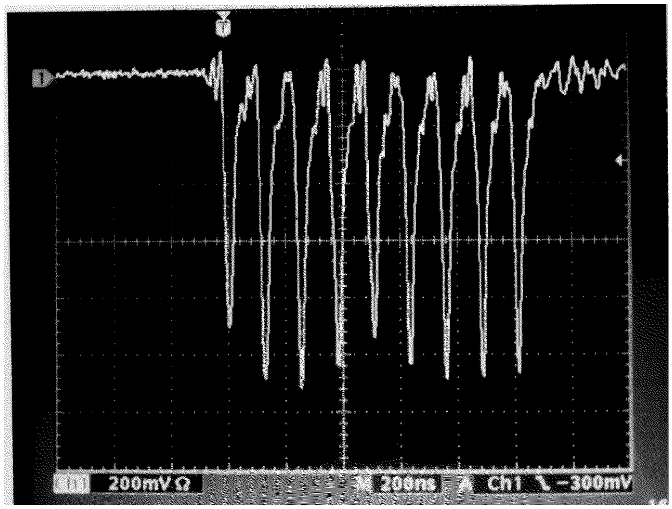

Figure 3.9: Oscilloscope picture of the typical beam time structure from CT. Bunch structure is clearly seen.

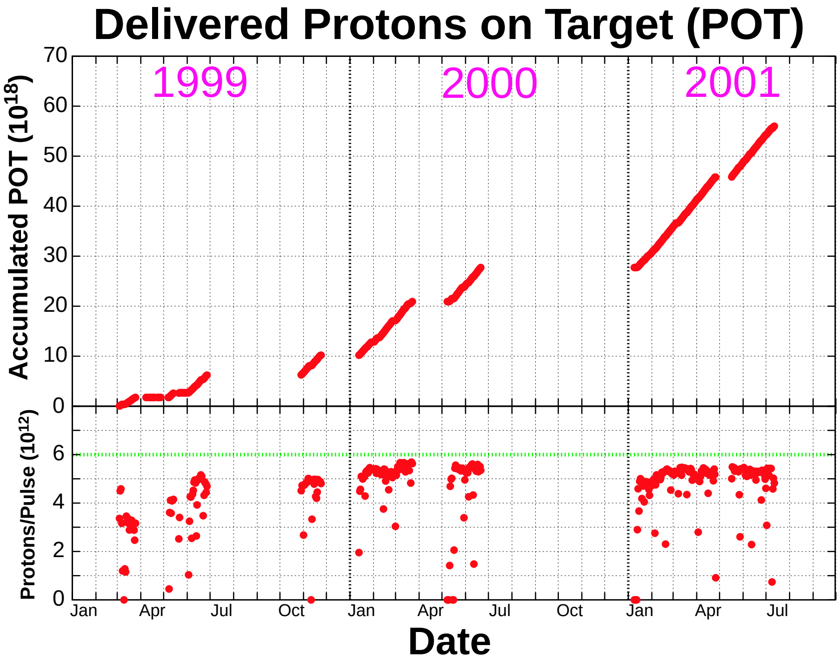

Figure 3.10: Accumulated number of protons on the target, measured by TARGET-CT.

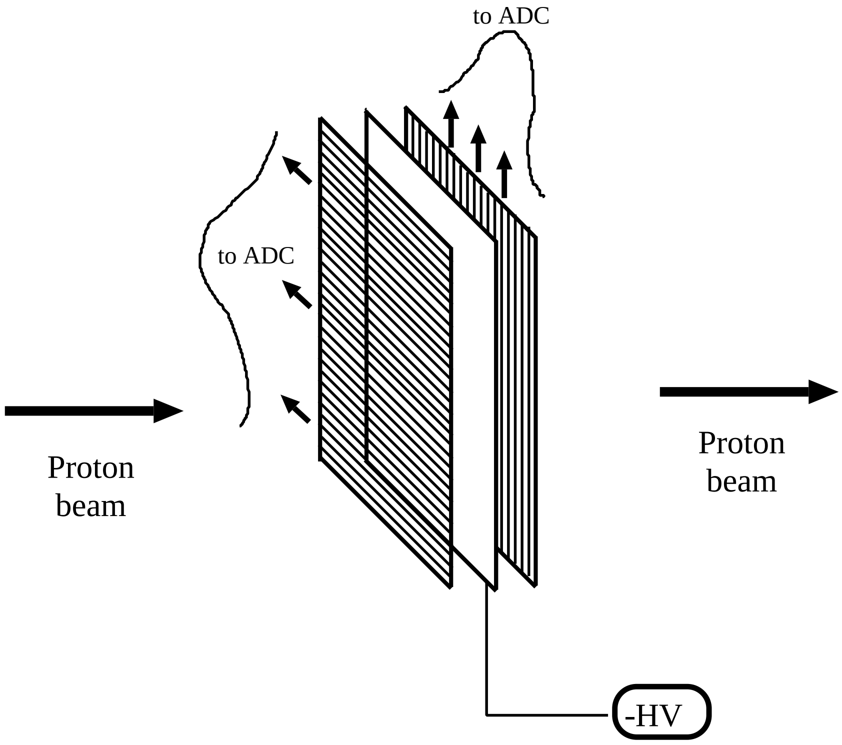

Figure 3.11: Schematic view of the SPIC.

The SPICs are used for steering of the beam. The proton targeting is continuously measured by a SPIC located just before the target, called "TARGET SPIC(TGT-SPIC)" (Figure 3.2). Typical proton beam distribution is shown in Figure 3.12. Figure 3.13 shows the stability of the distribution center fitted with a Gaussian distribution. Its fluctuation is within ± 1.5 mm.

The "P/PI" SPIC is used to monitor proton targeting and pion focusing as well.

3.3 Secondary Beam Monitors

Secondary beam monitors are installed to monitor pions, the parent particles of neutrinos, and muons generated from pion decay. Each of Muon Monitor (MUMON) and Pion Monitor (PIMON) is described below.

3.3.1 Muon Monitor

The MUMON is placed in a pit at the downstream of the beam dump (Figure 3.7,3.14). It consists of two parts; an ionization chamber (ICH) and a silicon solid detector (SSD) array. MUMON monitors the direction of the neutrino spill by spill, by means of monitoring the distribution center of muons, and the stability of the beam intensity and direction spill by spill.

The energy loss in the beam dump is about 5.5 GeV for a minimum ionizing particle. Only 2.1% of muons can reach at the MUMON position due to the energy loss. All the hadrons

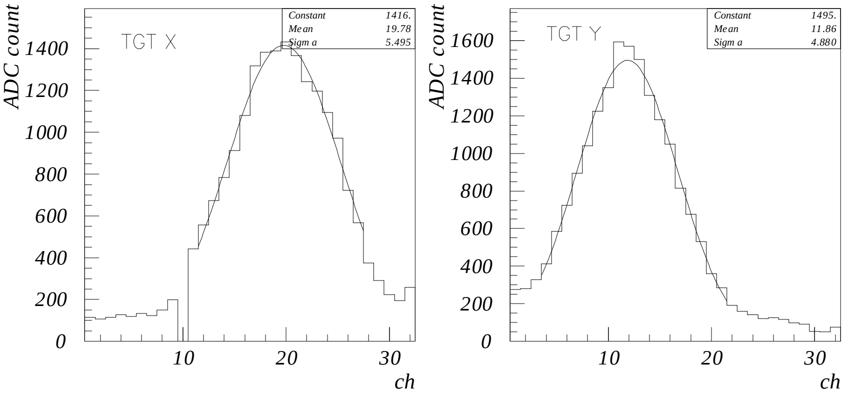

Figure 3.12: Typical proton beam distribution measured by TARGET-SPIC for November 1999 configuration.

are absorbed in the dump except for low energy neutrons. Figure 3.15 shows the momentum distributions of pions, muons and neutrinos before the beam dump. The muon threshold energy to reach to the MUMON, and the momentum distributions of pions and neutrinos corresponding to muons reaching to the MUMON are shown as well. MUMON profile works as a good indicator of the overall beam steering towards Super-Kamiokande, since the high energy muons are more sensitive to the beam direction than the low energy ones. Figure 3.16 shows the radial dependence of the neutrino intensity and energy spectrum at Super-Kamiokande. The predicted neutrino spectrum at Super-Kamiokande is almost same over $\sim$ 1 km, which corresponds to 3 mrad of the direction of the beam.

Ionization Chamber

The ionization chamber (ICH) is a segmented ionization chamber like SPIC. The cross section is 190 cm × 175 cm square to measure the broad muon profile at the beam dump. There are three planes inside the gas vessel filled with Ar gas. The gap between the two planes is 1 cm. Each readout plane is segmented into 5 cm × $\sim$ 200 cm strip lines to measure muon density distribution. The readout planes have 36 channels in the horizontal direction and 32 channels in the vertical direction. Each plane is divided into six sheets with a size of 60 cm × 90 cm, due to the difficulty of making one large sheet. The corresponding horizontal (vertical) readout strips in the vertically (horizontally) adjoining sheets are connected electrically. Each signal is recorded by charge sensitive ADCs. The gaps between those sheets are insensitive. There are two vertical gaps with 15 cm width and also a horizontal one with 25 cm width.

The calibration of the ICH was performed by the muon beam itself. During the stable run, the whole vessel of ICH is moved horizontally or vertically within ± 30 cm to check relative gain. It was performed several times during the long running period. Figure 3.17 shows the relative gain of each channel. The relative gain factor has been stable within several %.

Figure 3.18 shows a typical density distribution after gain correction.

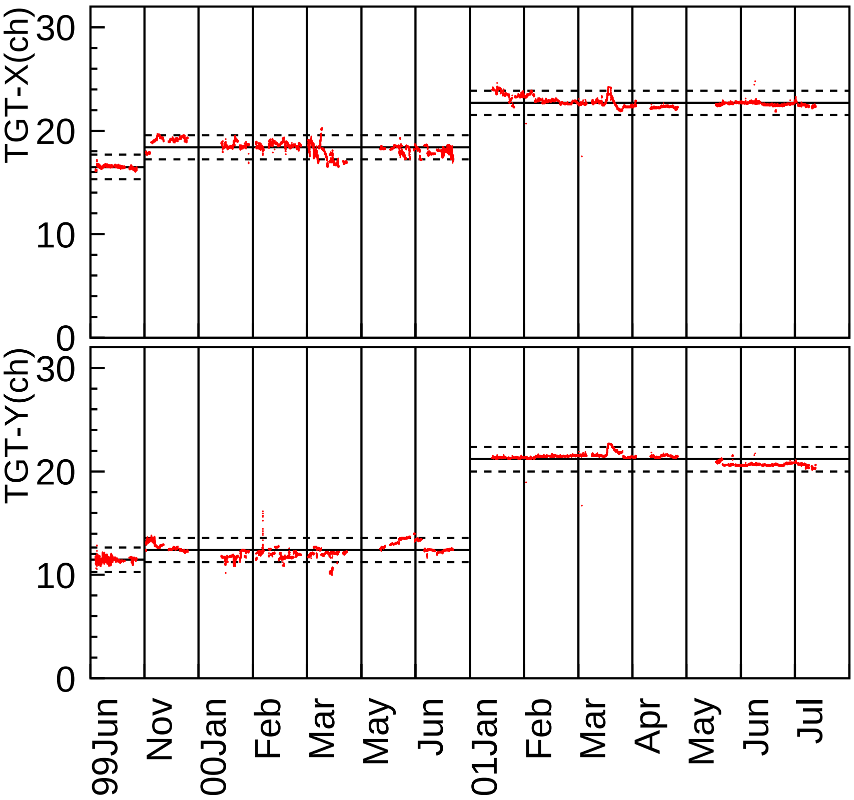

Figure 3.13: Stability of the proton distribution center measured by TARGET-SPIC, along the horizontal axis (upper) and the vertical axis (lower), averaged over 100 spills. The centers are shifted in November 1999 and January 2001 because the position of the SPIC has been changed. The unit of y-axis is channel of the SPIC, which corresponds to 1.27 mm. The dashed line in the figure shows the ± 1.5mm boundary in each period.

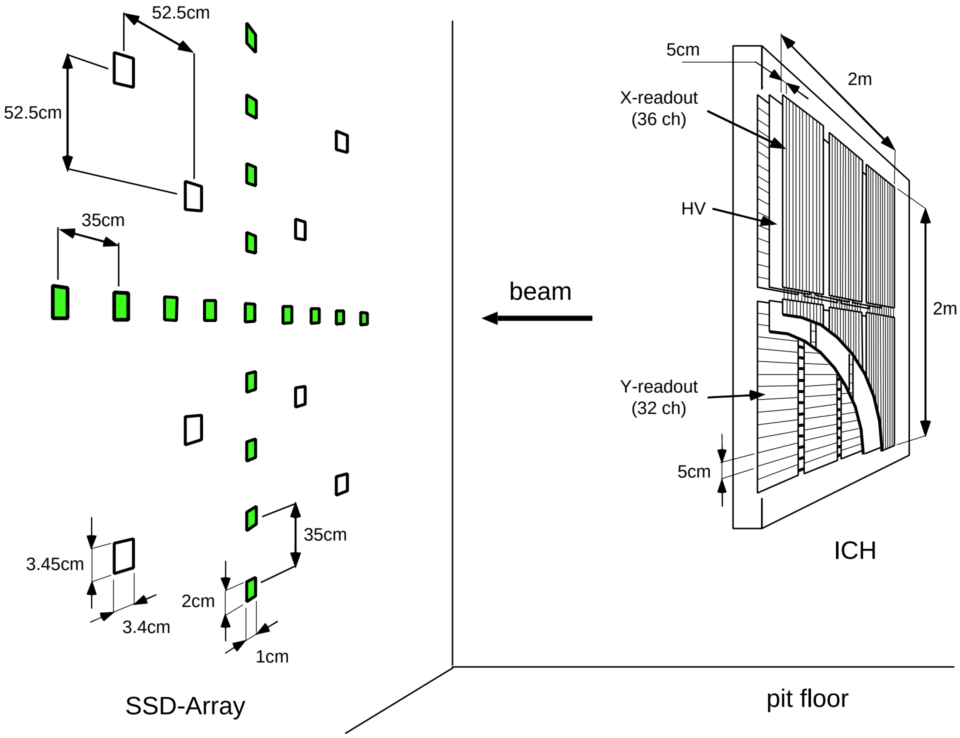

Figure 3.14: Schematic view of the MUMON, silicon solid detectors (SSD) array and ionization chamber (ICH).

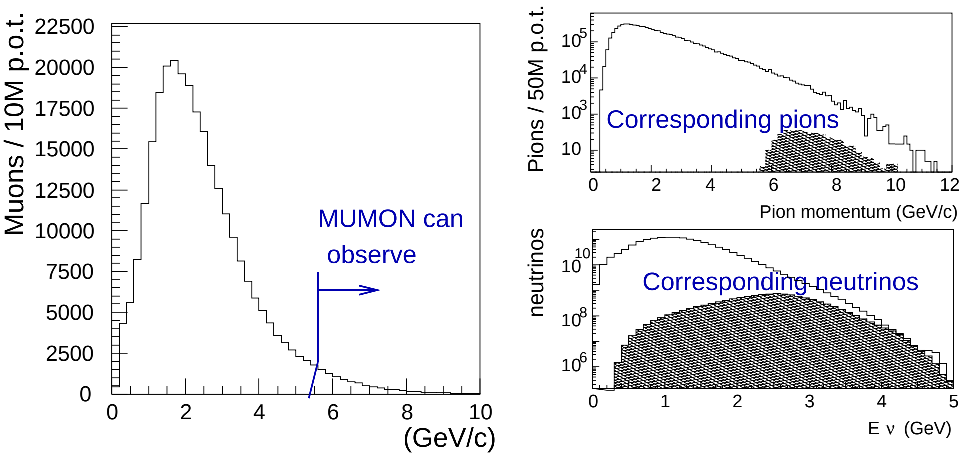

Figure 3.15: Left: Muon momentum distributions before the beam dump. The line indicates the threshold energy for the muons to reach the MUMON. Right-upper: Open histogram shows the momentum spectrum of generated pions, the hatched part shows pions whose produced muons reach to the MUMON. Right-lower: Open histogram shows the energy distributions of generated neutrinos in the beam line, the hatched part corresponds to the hatched area in right-upper figure. All the figures are based on a Monte Carlo simulation.

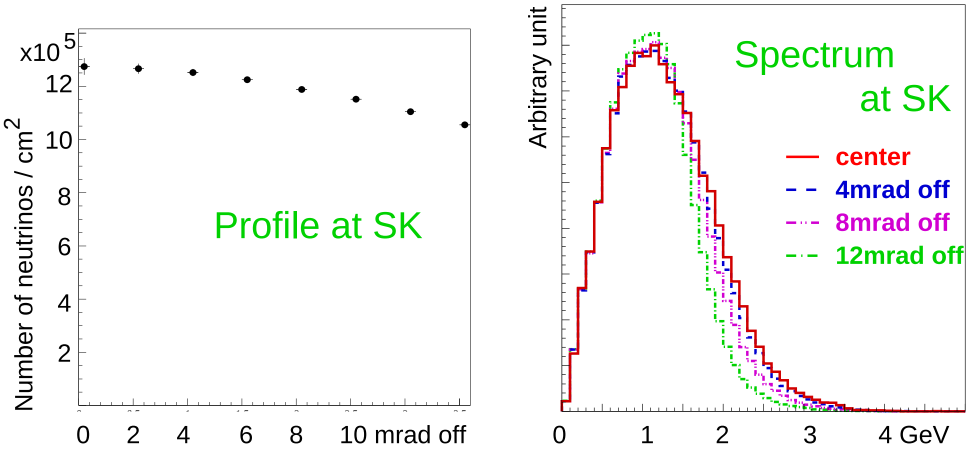

Figure 3.16: Neutrino profile and energy spectrum at Super-Kamiokande. Left: Neutrino spatial profile at SK site. Right: Radial dependence of neutrino energy spectrum at 250 km distance, without oscillation. Both figures are made by a Monte Carlo simulation.

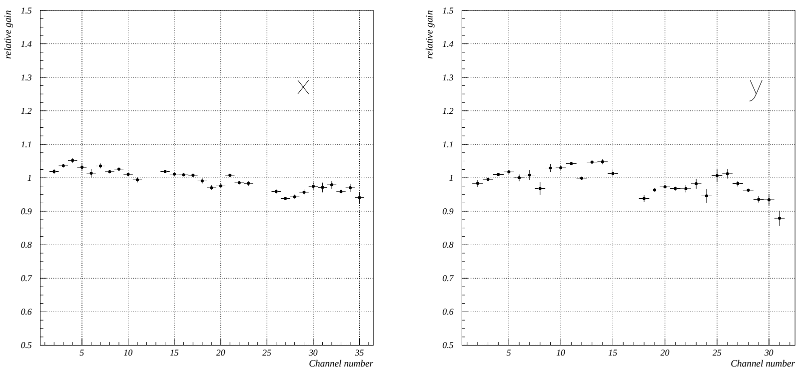

Figure 3.17: Relative gain of each ionization chamber channel, for horizontal(left) and vertical(right) directions. Error bars are the spill-by-spill fluctuations only.

Silicon Detector Array

The silicon detector (SSD) array is installed for redundancy. It gives the 2-dimensional information of the muon profile of 280 cm × 280 cm area. There are 17 small silicon detectors installed along the horizontal and the vertical axis and 9 large silicon detectors installed as diagonal array. The size of the small-type silicon detector is 1 cm × 2 cm with 300 μm of depletion layer, and the large is 3.4 cm × 3.05 cm with 375μm of depletion layer. The signals are read out by charge sensitive ADCs.

The relative gain of the small Si pads were measured using an LED light in the test bench. The result shows the uniformity is within ±6%. The large Si pads were calibrated using the muon beam, with setting all Si pads perpendicular to the beam center. From the comparison of observed charge, relative gains are obtained, although they have 10% level uncertainty form the z dependence of the muon intensity [15].

3.3.2 Pion Monitor

The pion monitor (PIMON) is a gas Čerenkov detector, which measures the momentum and the divergence of pions just after the second horn (Figure 3.2). PIMON is designed to be retractable. It is rolled into the beam-line only during the PIMON measurement run. Otherwise it is hidden at the escape position to avoid being a disturbance of the beam and its radiation damage. Figure 3.19 shows the schematic view of the PIMON.

The neutrino spectrum at an arbitrary distance can be calculated from pion angle and momentum information because the decay kinematics of the two-body decay of pions are completely known. The expected neutrino spectrum at Super-Kamiokande and the near detector (Φ^{SK}, Φ^{near}) were calculated by a Monte Carlo simulation of which results were compared with the PIMON measurement.

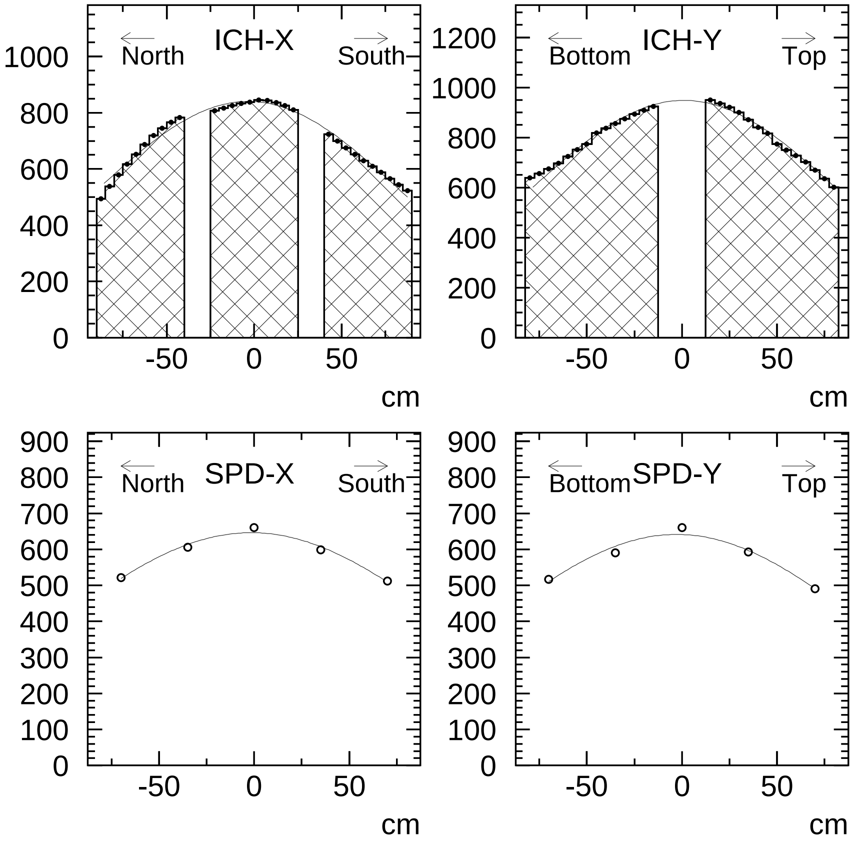

Figure 3.18: Typical muon distribution, for the ionization chamber(top) and the silicon detector array(bottom). The left two figures show the horizontal direction and the right ones show the vertical direction. Vertical axis is ADC count after pedestal subtraction and gain correction. The distribution is averaged over 100 spills. All the distributions are fitted with a Gaussian function to obtain the center.

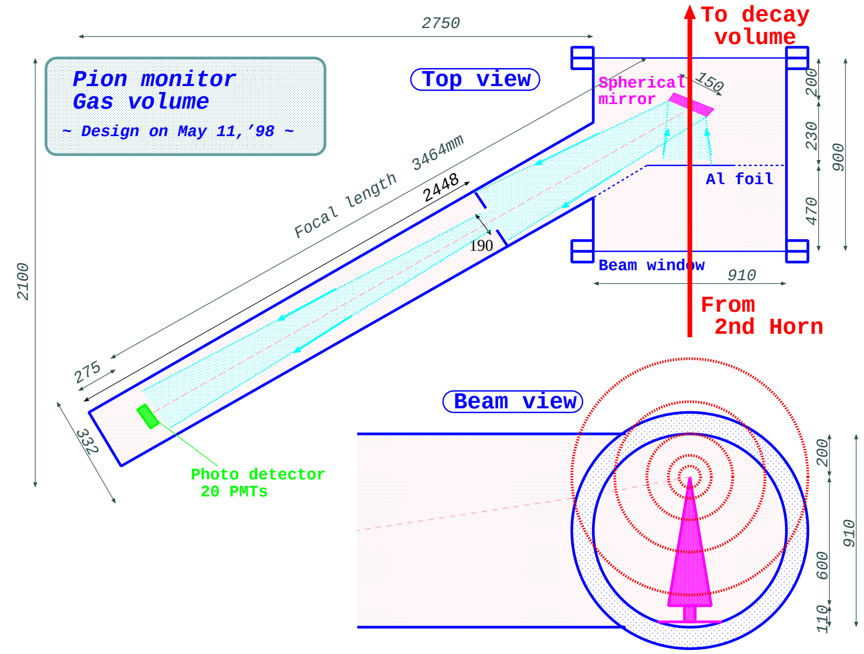

Figure 3.19: Schematic view of the PIMON

Gas Vessel

The gas vessel of the PIMON is a cylinder of 91 cm in diameter and 90cm in length, attached with approximately 3 m arm. Čerenkov lights generated in the gas are reflected by a pie-shaped spherical mirror on the beam line and detected by a photo detector at the focal plane. The gas vessel is made of 5mm thick stainless steel. There are two Aluminum beam windows located at the beam entrance and exit. Their thickness is 1mm in order to reduce interaction in the window, which corresponds to 0.01 radiation length and 0.0025 interaction length. A 50 μm thick aluminum foil is set 23 cm in front of the mirror to define the fiducial area, which is free from the deformation of the beam window.

The gas vessel is filled with freon gas R-318 (C_4F_8) to obtain a high refractive index, which is required to measure the pion momentum as low as possible. It is important to know the low energy neutrino flux to investigate a lower Δm^2 region. In order to avoid severe background from the primary proton, the refractive index should be lower than $n = 1.00264$ (Figure 3.20). The pion momentum threshold determined by the refractive index is 2 GeV, which corresponds to 1 GeV for neutrinos.

Gas pressure can be controlled by an external gas system. Several Čerenkov photon distributions are measured with different Čerenkov threshold, by changing the gas pressure. The absolute refractive index was calibrated by the Čerenkov photon distribution from 12 GeV proton, at the pressure above proton Čerenkov threshold. Diameter of the Čerenkov ring of proton shows that at the 2.11 atm gas pressure the radiator has refractive index of 1.00294 (Figure 3.21).

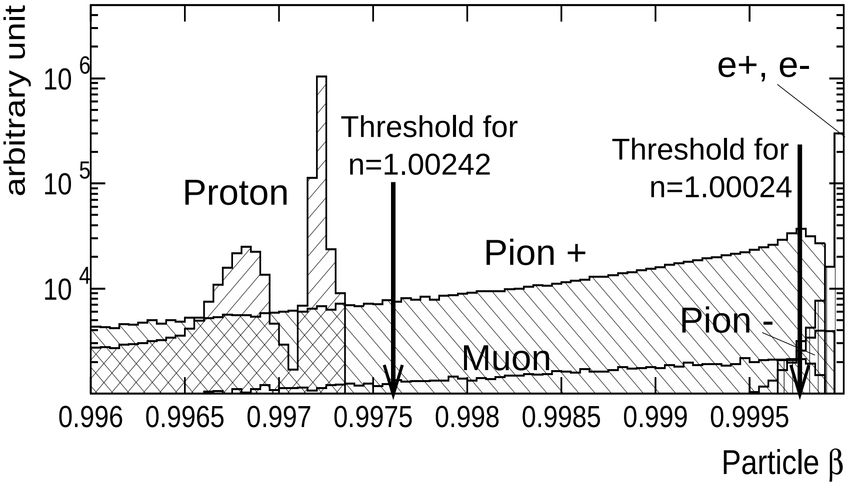

Figure 3.20: Distribution of beta for protons, pions, muons and electrons after the second horn.

Spherical Mirror

Figure 3.23 shows the spherical mirror of the PIMON. It focuses Čerenkov photons on a ring at the focal plane if they are emitted by particles which have the same beta and angle, independent of its emission point (Figure 3.22). The radius of the curvature is 6000 mm and the size is 600 mm × 150 mm. Its thickness is about 8 mm. It is made of Pyrex glass which is partially coated with aluminum and frosted by sand to make a pie-shape.

The mirror must have a large kick angle because the photo detector has to avoid the primary beam. The "kick angle" is defined as the angle between the beam direction and the normal of the spherical mirror around the beam center. It is set to 30 degrees.

The advantage of the pie-shaped mirror is that the reflected image is aligned one-dimensionally, while a simple round spherical mirror makes a distorted image (Figure 3.24). In addition, the pie-shaped mirror has an advantage of detecting only the radial divergence of pions. It is neccesary to know only the radial divergence in order to obtain neutrino flux.

Photo Detector

The photo detector consists of 20 photo multiplier tubes (PMTs), as shown in Figure 3.25. It is kept as far away from the beam line as possible in order to avoid its radiation damage in the beam line area. Signal of each PMT is lead by a 100 m long cable to a charge sensitive ADC placed in the data acquisition room outside.

PMTs are modified-R5600-01Q type made by Hamamatsu Photonics Corporation. The size is 15.5 mm in diameter of the outer socket and 8 mm in diameter of the photo-cathode. They are aligned along the vertical direction with 35 mm steps. These PMTs have 3 notable changes from the standard R5600-01 PMTs;

- Quartz window.
  This is for radiation hardness. The standard BK7 window gets dark under sever radiation

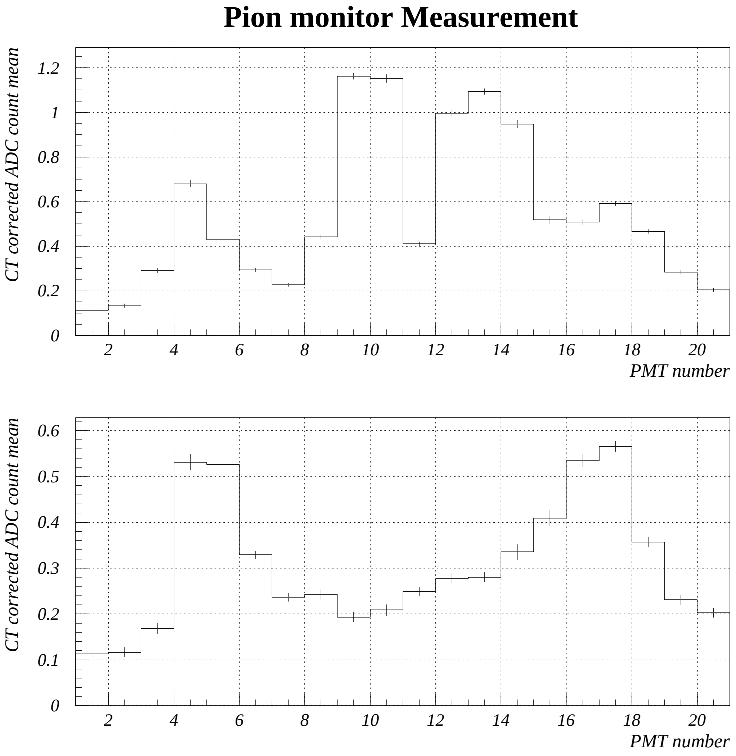

Figure 3.21: Čerenkov photon distribution of 12 GeV proton and pion. Top figure shows the ring of proton mixed with pion (taken above the proton Čerenkov threshold: 2.11 atm). Bottom figure shows only the pion ring (taken below the proton Čerenkov threshold: 1.9 atm).

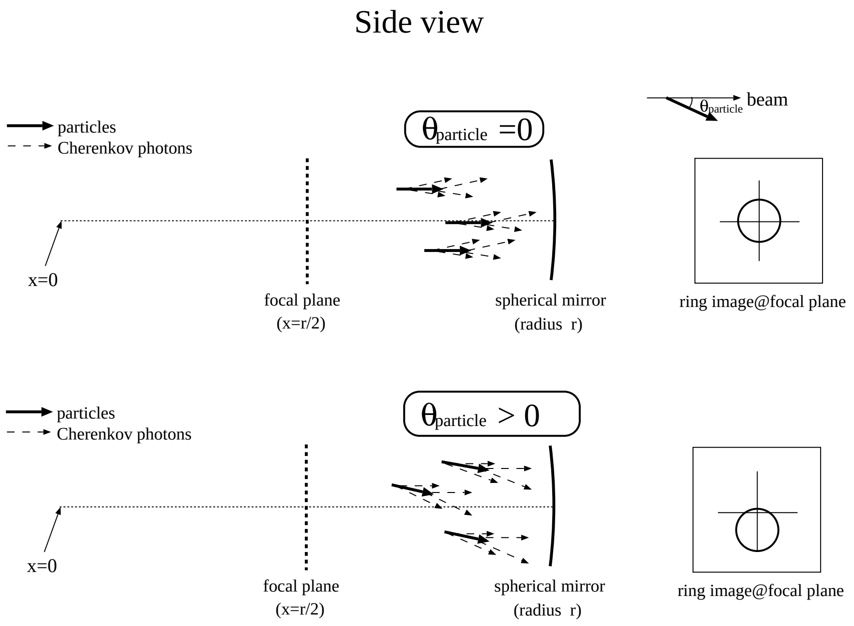

Figure 3.22: Principle of the shperical mirror.

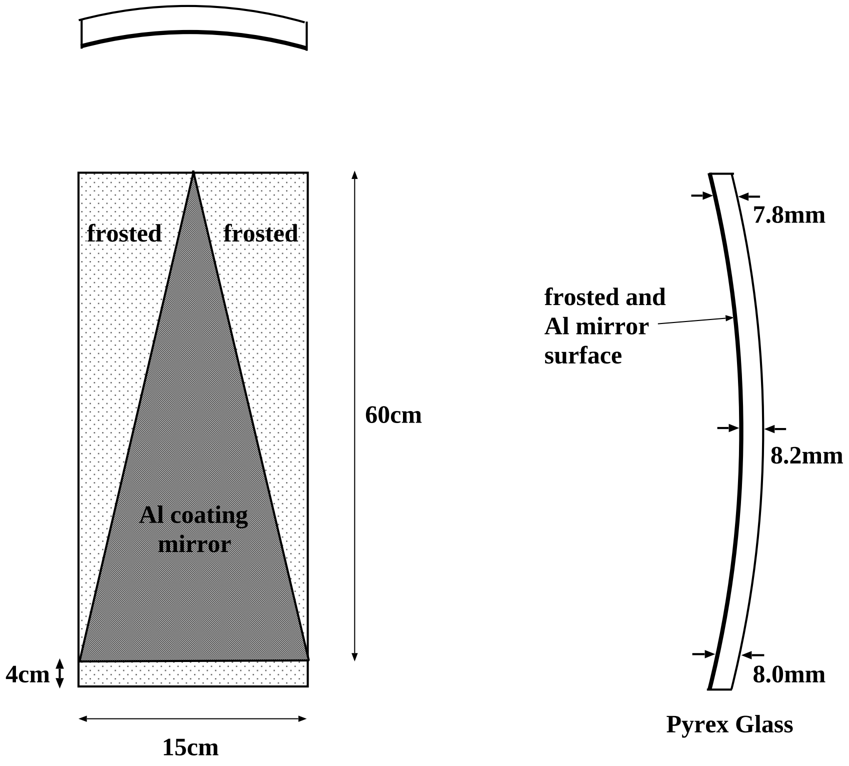

Figure 3.23: The spherical mirror of the PIMON.

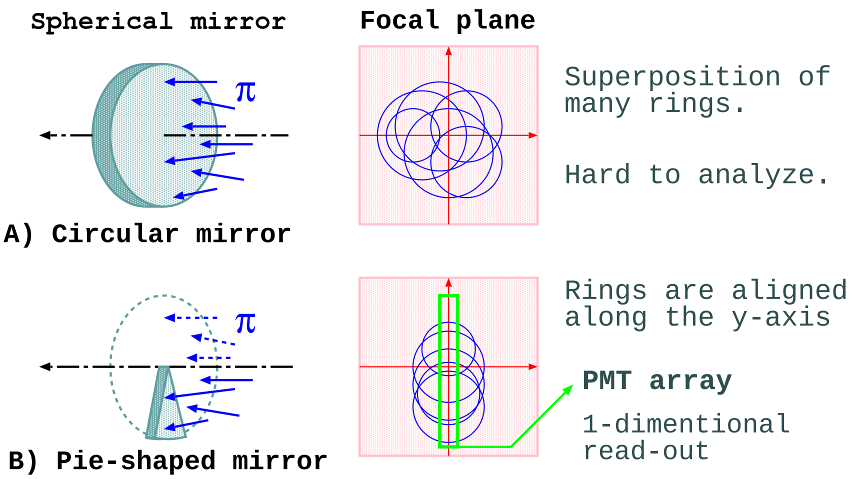

Figure 3.24: The ring images of the Čerenkov light on the focal plane of a spherical mirror.

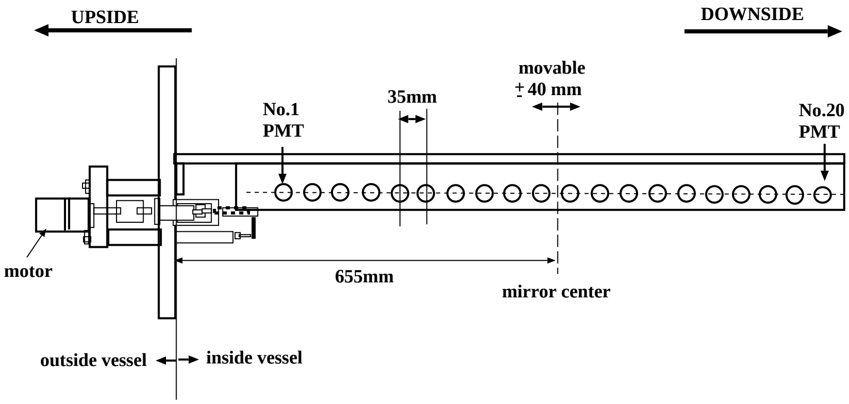

Figure 3.25: Photo detector of the PIMON.

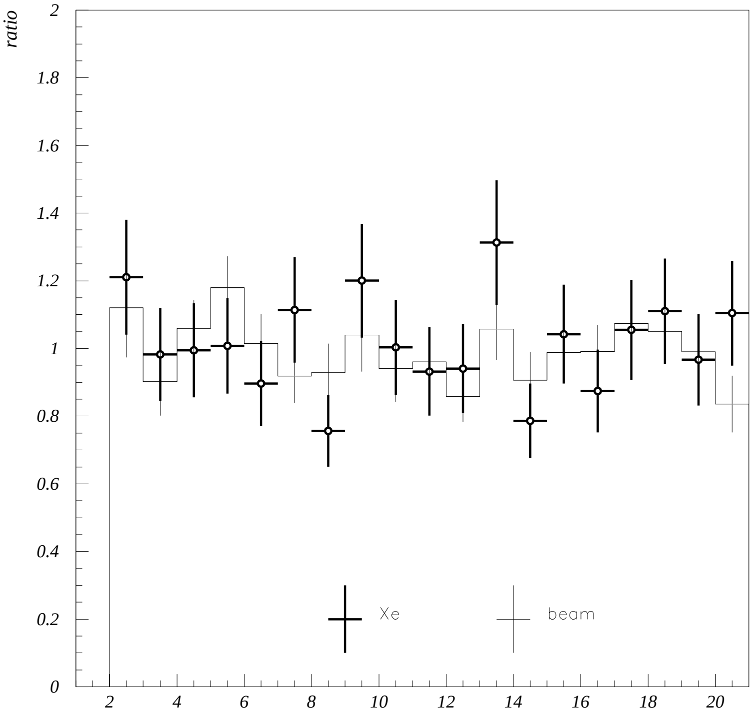

Figure 3.26: Relative gain of neighbouring PMTs of the photo detector.

while quartz is quite strong against radiation. The radiation hardness is tested by an exposure at KEK-PS-K3-beamline [15, 19].

- Multi-alkali(Sb-Na-K-Cs) photo-cathode material.
  This is selected because of its wide dynamic range for intense light. A multi-alkali photo-cathode does not saturate up to 10μA, while a standard bialkali photo-cathode saturates at 0.1μA [20].

- Low gain.
  PMTs should observe large amount of Čerenkov photon ($\sim 10^9$ photons instantly). Low gain PMT is required not only to adjust signal level to ADC but also to avoid the signal saturation. The PMT is modified to reduce the multiplication in each dynode step. The gain of the PMT is set to 300 in June 1999 run. It was lowered to 20 $\sim$ 50 in November 1999 run because signal was saturated in June 1999 run.

The calibration of PMTs was performed by a Xe lamp and Čerenkov photon. The PMT array was moved vertically within ± 40 cm to check relative gain. Figure 3.26 shows the relative gain of each PMT.

Results

PIMON measurements were performed twice, in June 1999 and November 1999. To avoid PMT saturation, the beam intensity was reduced by one order in June and by two in November. Furthermore, the number of bunch was reduced to one for the same reason.

Figure 3.27 shows the neutrino energy spectra at the near and the far site, and the far to the near ratio of the spectrum predicted by the PIMON for the November 1999 configuration. The prediction by the beam simulation agrees with that by PIMON.

3.3.3 Beam-line DAQ

Beam spill trigger is used as a trigger signal for the data acquisiton (DAQ) of the beam monitors and the near detectors. It is provided from the accelarator, 120μsec before the beam extranction. Simultaniously, a 16-bit spill number is distributed to each DAQ site to identify the spill. There is another trigger signal provided 1.1ms before the beam extraction, which is used to excite the horns.

Signals from each detector, CTs, SPICs, MUMON (and PIMON during the PIMON run) are digitized by charge sensitive ADCs spill by spill. The gate widths of ADCs are 1.2μsec full beam spill for CTs and 2.0μsec for the others. There are 6 front-end computers(PCs) along the beam line and one host PC to collect digitized information.

In addition to the charge information, GPS timestamp for each beam firing time is taken by the VME module in the beam control room. This is because the GPS receiver is installed there.

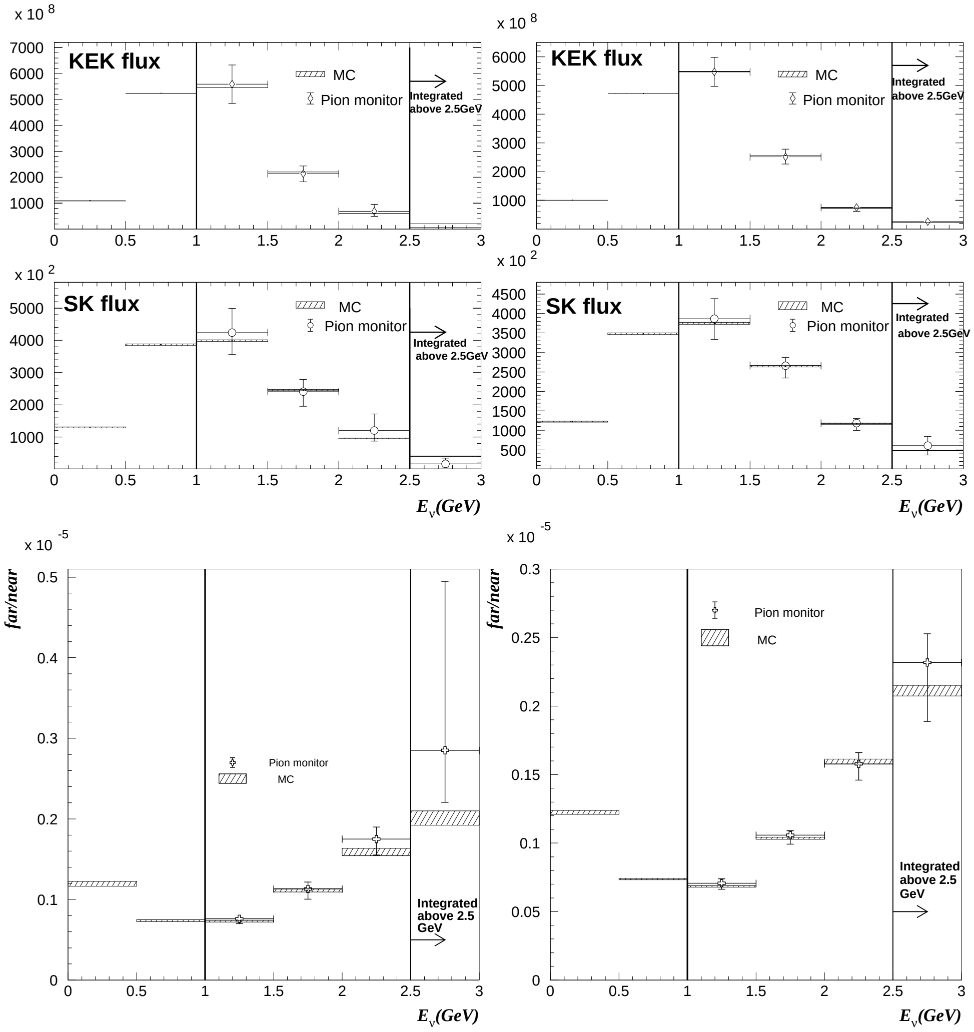

Figure 3.27: The neutrino energy spectrum at near site (top), far site (middle) and the far to the near ratio (bottom). Left figures are for June 1999 and right figures are for November 1999. The crosses represent a prediction by PIMON and the hatched boxes show the prediction by beam Monte Carlo.

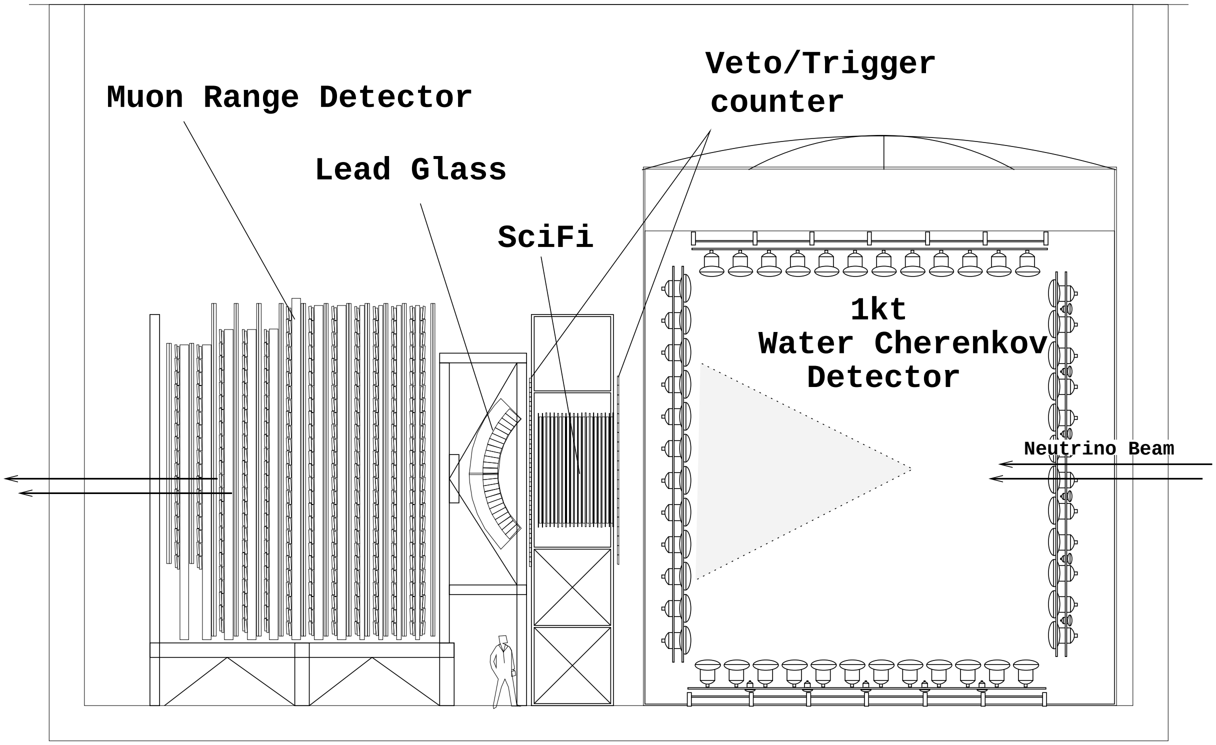

Figure 3.28: Schematic view of the near detectors.

3.4 Near Detectors

Near detectors are located 300 m downstream of the target. The experimental hall accommodating the near detectors is 24 m in diameter and 16 m in depth. The near detectors consist of six components. From upstream to downstream are the 1kt Water Čerenkov detector, the Veto counter, the Scintillating Fiber tracker (Sci-Fi), the Trigger counter, the Lead Glass calorimeter (LG) and the Muon Range Detector (MRD). Figure 3.28 shows the schematic view of the near detectors. The details for each component is described below.

3.4.1 1kt Water Čerenkov Detector

The 1kt Water Čerenkov Detector measures neutrino beam properties such as intensity, vertex distribution and energy. It is located at the most upstream part of the experimental hall. The advantage of the 1kt detector is canceling out of the systematic uncertainties inherent in a water Čerenkov detector since it has the same target material (H_2O), detection principle and analysis algorithm as the Super-Kamiokande.

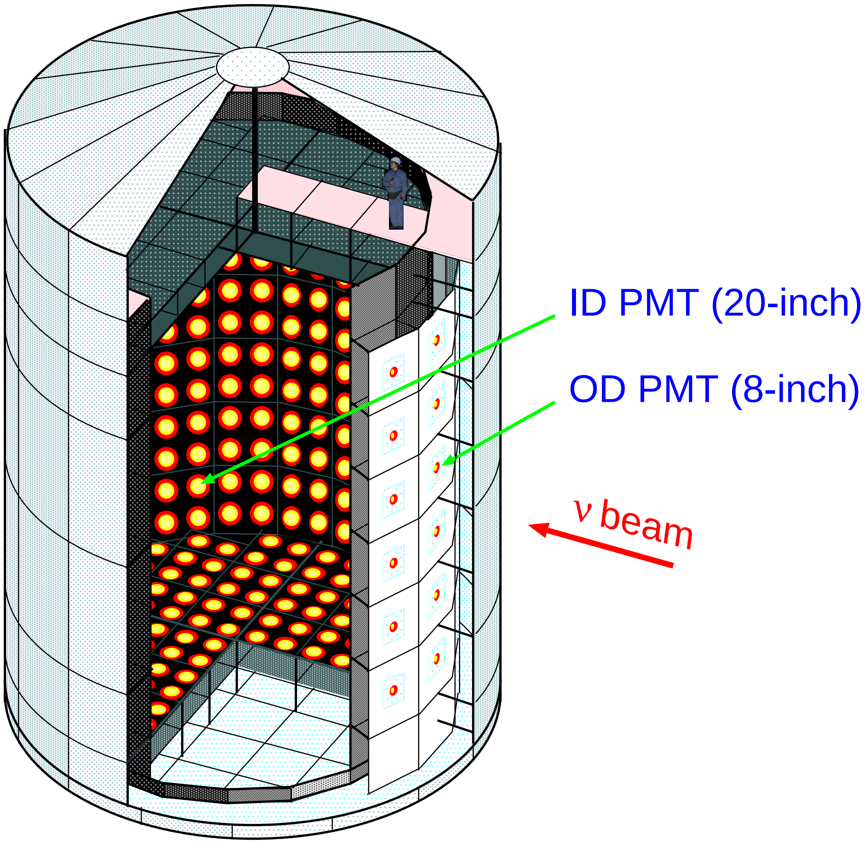

Figure 3.29: Schematic view of the 1kt Water Čerenkov Detector.

Water Tank

The 1kt Water Čerenkov detector consists of the cylindrical tank of 10.8 m in diameter and 10.8 m in height, filled with approximately 1000 tons of pure water. Figure 3.29 shows the schematic view of the 1kt detector.

The inside of the tank is optically separated into two parts; the inner detector (ID) and the outer detector (OD). There are stainless steel frames for supporting the PMTs in the optically insensitive region. The ID is a cylindrical water Čerenkov detector, 8.6 m in diameter and 8.6 m in height. There are 680 20-inch PMTs mounted on the support frame facing inwards; 456 of them are attached to the side wall and the rest are to the top and the bottom walls. The PMT spacing is the same as Super-Kamiokande, *i.e.*70 cm. The space between PMTs are lined with black polyethylene telephthalate sheets to prevent light reflection and for optical separation. The specification of the ID PMT is described in Section 4.3.

The OD is also a water Čerenkov detector. Its thickness is 1 m for the barrel and 0.6 m for

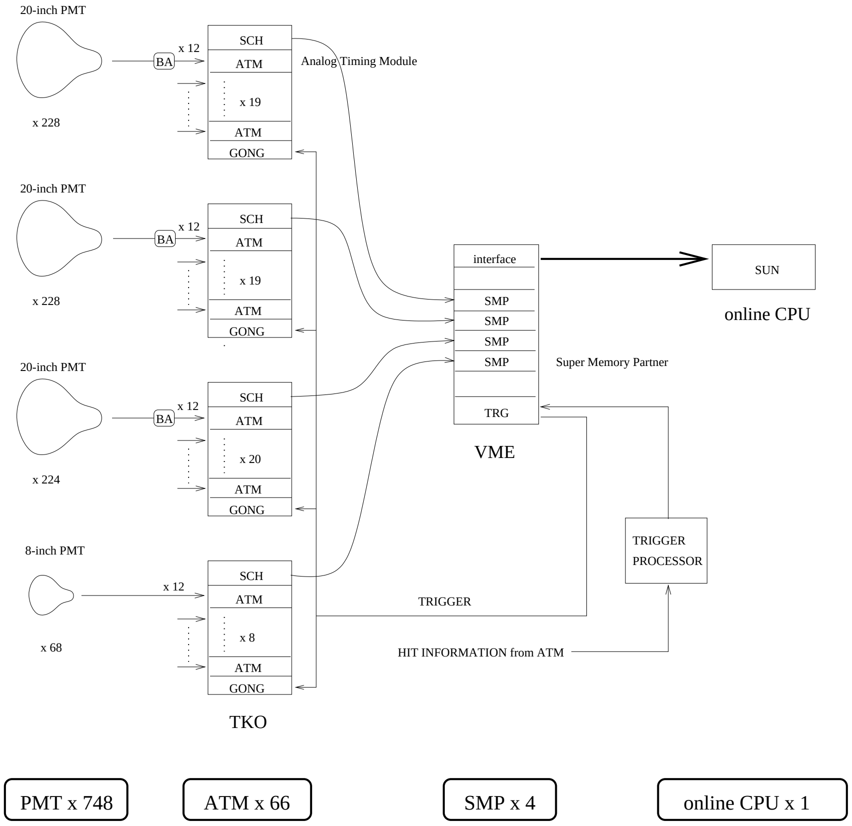

Figure 3.30: Data acquisition system for the 1kt Water Čerenkov Detector.

the bottom. There are 68 8-inch PMTs facing outwards on the support frame, 42 of them are attached to the upstream 1/3 of the barrel part, *i.e.*, ±60 degrees with respect to the neutrino beam. All the rest PMTs are attached to the bottom wall. The PMT spacing is 1.4m. Each PMT is fitted with a 60 cm square plate of wavelength shifter to increase the light collection efficiency. The inner surface of OD is covered with Tyvec sheets, which is known as reflective material, in order to maximize the light detection efficiency.

Data Acquisition System

The electronics and data acquisition system in the 1kt detector are shown in Figure 3.30. They are very similar to those in Super-Kamiokande described in Section 4.5. Only the differences are described here.

In order to cope with multiple events produced within a 1.1 μsec beam spill, the readout electronics (ATM, to be described in Section 4.5) used in the 1kt detector was modified from that of Super-Kamiokande. A signal cable connecting a 20-inch PMT and ATM is 70 m long in Super-Kamiokande. A reflection pulse is induced 700nsec later to ATM, caused by a impedance mismatch. In order to avoid this reflection pulse, each channel in ATM used in Super-Kamiokande has a 900nsec dead time every time it is hit. On the other hand, the dead time of the ATM used in 1kt detector was reduced to 300nsec, since the 900nsec dead time would make it difficult to record multiple events. In 1999 run, the signal cables were extended by 40 m to delay the reflection pulse 1.1 μsec later, out of the beam spill. Since January 2000, buffer amplifiers have been installed for impedance matching. The 40 m delay cables are removed since then because the delay cable caused an additional reflection pulse. A total of 66 ATMs are used for ID and OD.

It is possible for ATM to miss a part of hit signals if multiple events occurred in a beam spill because the dead time exists in ATM and each ATM has only 2 TAC/QAC per channel. A 500 MHz 8 bit Flash-ADC (FADC) module with 16 μsec full scale is installed to record multiple events. An analog sum of all the signals from PMTs are recorded separately for ID and OD by the FADC.

The trigger is made by Trigger Processor module. A linear sum of the hit signals from ID PMTs goes through a discriminator that determines the trigger threshold. The threshold is set to 450 mV, which corresponds to about 40 hits at inner PMTs. In the 1kt detector, the event trigger is permitted being sent during the beam spill.

Calibration

The calibration of the 1kt detector is very similar to that of Super-Kamiokande described in Section 4.6. Only the difference are described here.

In the 1kt detector, the gain of 110 standard inner PMTs were pre-calibrated to ±0.5% in the test bench [21]. The other inner PMTs were calibrated relative to the standard PMTs within 5.7% using a Xe lamp calibration system similar to that of Super-Kamiokande.

The absolute energy scale is checked by the π^0 invariant mass and stopping comic ray muons. They are compared with Monte Carlo simulations. The uncertainty is estimated to be ±5% (Figure 3.31).

3.4.2 Trigger Counter/Veto Counter

The trigger counter/veto counter consists of 60 scintillator units located at the upstream and downstream of the Sci-Fi. The downstream counter is used as the trigger counter for Sci-Fi, LG and MRD. It consists of 40 scintillator units piled on top of one another, covering an area of approximately 4 m × 4 m. Each unit is made of plastic scintillator of 466 cm in length, 10cm in width and 4 cm in thickness. One PMT is attached to each end of the scintillator (Figure 3.32). Both timing and charge information of the PMT signal are recorded to obtain timing and deposit energy of charged particles.

The purpose of the upstream counter is to veto changed particles coming from the 1kt detector and cosmic ray muons. It consists of 20 scintillator units placed on top of one another, covering the same area as the trigger counter. The scintillator plate used for the veto is the same as the trigger counter, but each unit is composed of two plates. Two PMTs are attached as well as the trigger counter.

3.4.3 Scintillating Fiber Tracker

The Scintillating Fiber tracker [22] is used to study neutrino interactions with its fine granularity. It consists of 20 scintillating fiber sheet modules interleaved with 19 water filled aluminum tank layers, as shown in Figure 3.33. Each module has 6 horizontally aligned and 6 vertically aligned fiber sheets, supported by a honeycomb panel. One scintillating fiber sheet has 1142

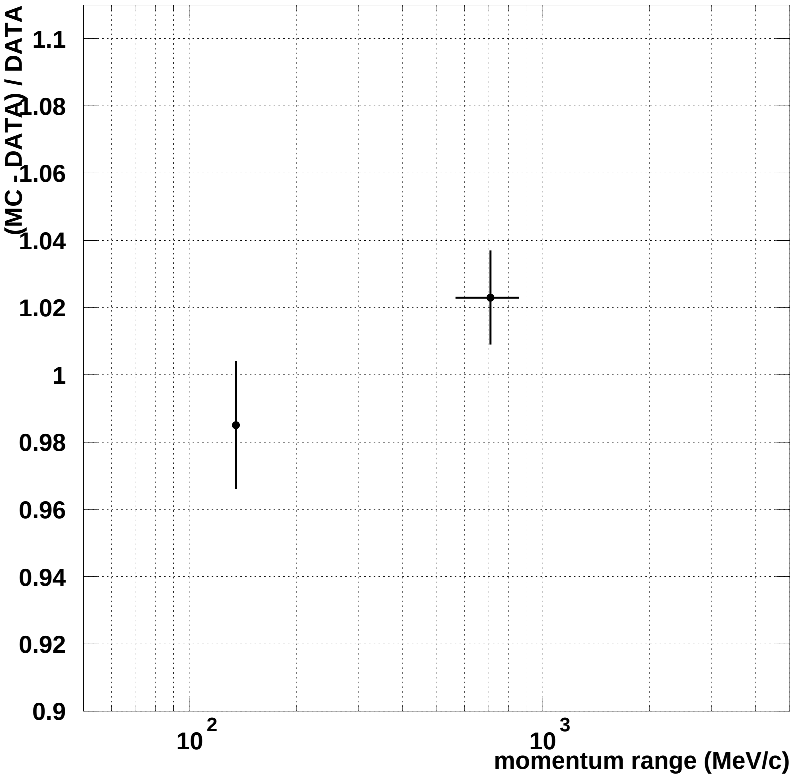

Figure 3.31: Absolute energy scale of the 1kt detector obtained by means of the π^0 invariant mass and stopping muons. In total, the uncertainty is estimated within ±5%.

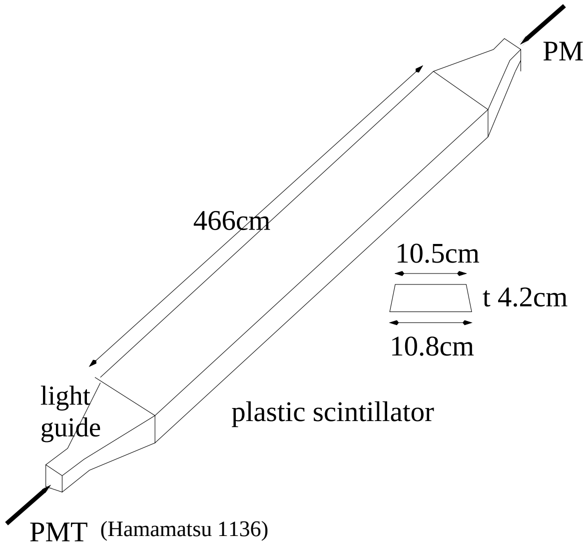

Figure 3.32: The scintillator unit of the Trigger counter and the Veto counter

fibers, each of which is 3.7m in length. The fibers are attached to 24 image intensifiers (IITs) with CCD readouts. Each water layer consists of 15 water tank made of 1.8 mm thick aluminum. The dimension of the water tank is 240 cm × 16 cm × 4 cm. Total target mass is 6.0 tons of water and 1.4 tons of aluminum. For the tracking method in Sci-Fi, refer to [22].

3.4.4 Lead Glass Calorimeter

The purpose of the Lead Glass (LG) calorimeter is to distinguish electrons from muons. It is located downstream of the Sci-Fi. The LG consists of 10 modules, each of which has 60 LG cells (Figure 3.34). The dimension of the cell is about 10cm × 10 cm × 34 cm. A 5-inch PMT is attached at the one end through a light guide, which is also made of cylindrical lead glass of 2.5 inch in radius and 6cm in length. The LG calorimeter was reused from the TOPAZ experiment.

3.4.5 Muon Range Detector

The Muon Range Detector [23] is a range type calorimeter for neutrino induced muons, which is used to measure neutrino beam properties such as intensity, vertex distribution and energy. Figure 3.36 shows the schematic view of the MRD.

It consists of 12 iron absorbers sandwiched with 13 vertical and horizontal drift chambers as shown in Figure 3.35. The size of the layer is approximately 7.5 m × 7.6 m. In order to get a good energy resolution, 4 iron plates in the upstream side are 10 cm thick, and the others are 20 cm thick. The total thickness of 2m covers up to 2.8 GeV/c muons. Its total mass is 864 tons of iron and 51 tons of drift chambers.

There are 829 drift chambers, each of which has 8 cells of 5 cm × 7 cm cross section as shown in Figure 3.36. One drift chamber layer is arranged with 25 modules of 7.6 m length with a 2cm gap between two modules. For some layers, two short modules were combined side-by-side to

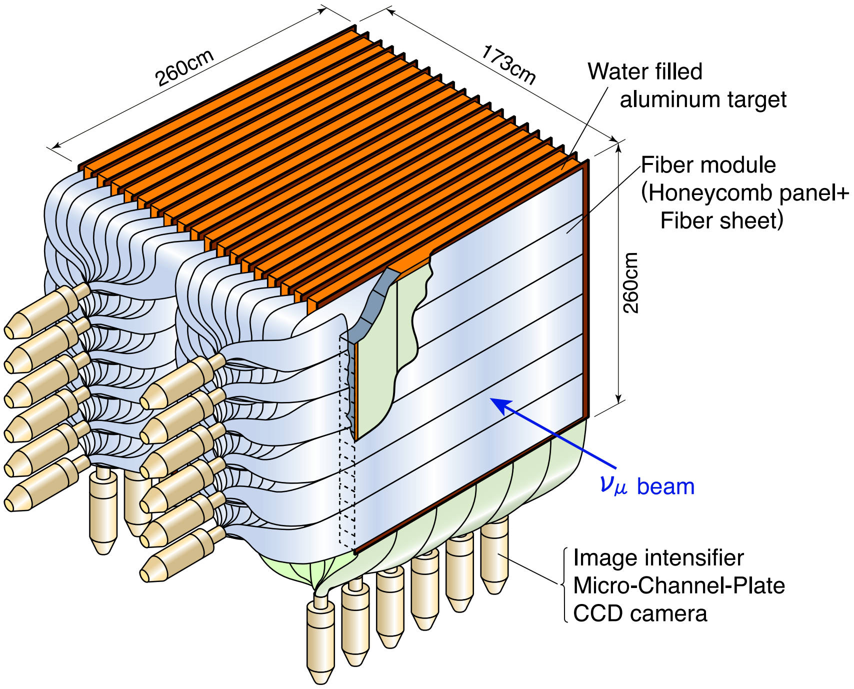

Figure 3.33: Schematic view of the Scintillating Fiber tracker.

make 7.6m sensitive length. The chamber is filled with P10 gas, which is mixture of 90% argon and 10% methane. These chambers were reused from the VENUS experiment [24].

Figure 6.4 shows the vertex distribution in MRD. The neutrino beam is aimed at Super-Kamiokande within 1 mrad accuracy as shown in Figure 6.5.

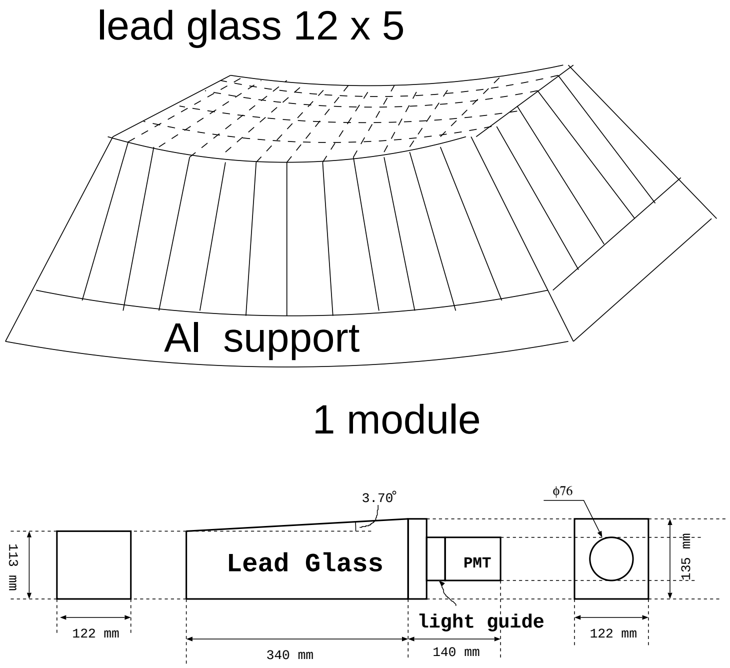

Figure 3.34: Schematic view of one module and the cell of the Lead Glass calorimeter.

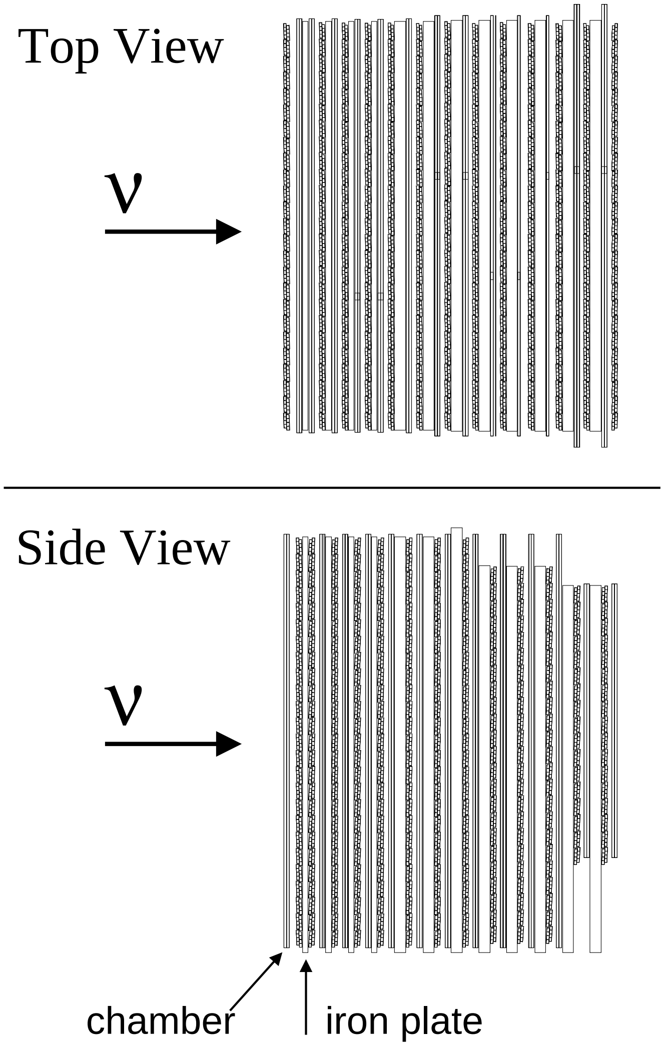

Figure 3.35: Schematic view of one cell of the Muon Range Detector.

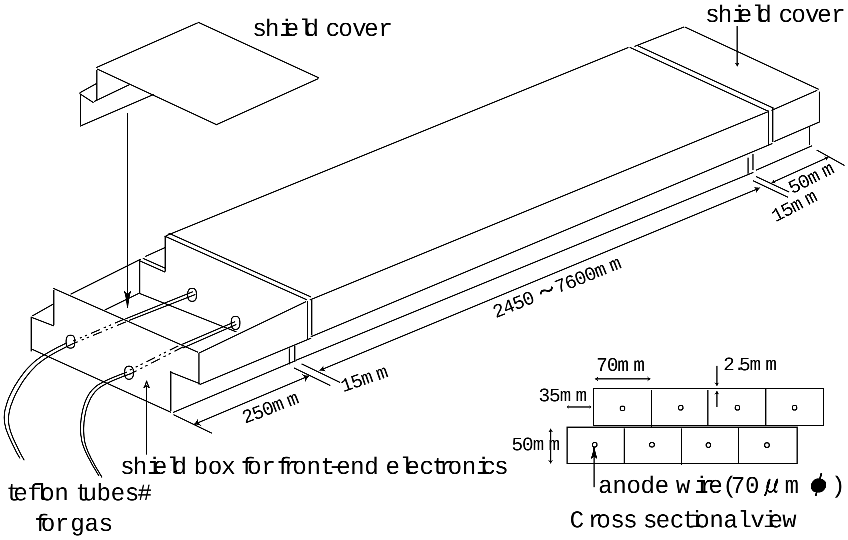

Figure 3.36: Drift chamber of the MRD.

Chapter 4

Super-Kamiokande as the Far Detector

Super-Kamiokande, a cylindrical 50 kiloton ring imaging water Čerenkov detector, is used as the far detector for this experiment. It is located 1000m underground in the Kamioka Observatory of Institute for Cosmic Ray Research, the University of Tokyo, in the Kamioka mine of Gifu Prefecture. The thickness of rock is equivalent to 2700 m of water. Figure 4.1 is the schematic view of the detector and the experiment site. The Super-Kamiokande experiment started taking data on April 1 1996, for the various physical motivation, such as nucleon decay search [25], atmospheric neutrino, solar neutrino measurements [13] and Supernova neutrino observation.

4.1 Detection Principle

Super-Kamiokande detects Čerenkov photons generated by charged particles which propagate in water. Reconstructed are the vertex position, number of rings, direction, momentum and particle type of the charged particle, using the information of the photon arrival time and pulse height of each PMT.

Čerenkov photons are emitted when a charged particle travels in a medium at the velocity faster than the light velocity in the medium. They are emitted on a cone of half angle θ, known as Čerenkov angle, with respect to the direction of the particle track. This θ is determined by

$$\cos\theta = \frac{1}{n\beta} \tag{4.1}$$

where n is the refractive index of the medium ($n \doteqdot 1.33$ in water), $\beta = v/c$ is the velocity of the charged particle and c is the velocity of light. In water, θ is about 42° for a charged particle with $\beta = 1$. The threshold momenta for the Čerenkov radiation are 0.58, 120, 159 and 1070 MeV/c for electrons, muons, pions and protons, respectively.

The number of Čerenkov photons emitted per unit path length x per unit frequency ν is given as following:

$$\frac{d^2N}{dxd\nu} = \frac{2\pi\alpha}{c}\left(1 - \frac{1}{n^2\beta^2}\right), \tag{4.2}$$

where α is the fine structure constant. About 340 photons/cm are emitted in water, in the wavelength region 300nm $\sim$ 600nm where the PMT is sensitive.

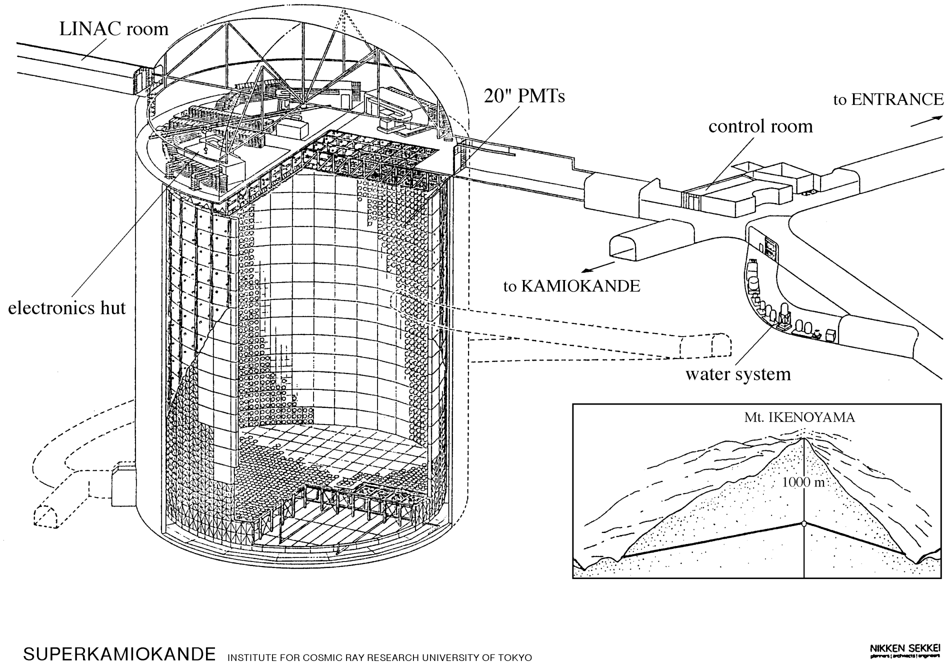

Figure 4.1: Schematic view of Super-Kamiokande.

4.2 Water Tank

Super-Kamiokande is held in a stainless steel cylindrical tank of 39.3 m in diameter and 41.4 m in height, containing 50 kt of pure water. The detector is separated into two part; the inner detector (ID) and the outer detector (OD). The ID is completely surrounded by the OD. Two parts are optically separated by a pair of opaque sheets 55 cm apart which enclose a optically insensitive region of 55 cm in thickness. There are stainless steel frames in this dead region for supporting PMTs (Figure 4.2).

The inner volume is a cylinder of 33.8 m in diameter and 36.2 m in height. Its total volume is 32 kt. There are 11146 20-inch PMTs mounted on the support frame facing inwards, 7650 of them are attached to the side wall and the rest are on the top and bottom walls. The PMT spacing is 70 cm. The space between PMTs are lined with black polyethylene telephthalate sheets to prevent light reflection and for optical separation. The photo cathode coverage is about 40%.

The thickness of OD is 2.0 m for the side, 2.2 m for the top and bottom. There are 1885 8-inch PMTs mounted outwards on the support frame, 1275 of them are attached to the side wall, 302 are attached to the top wall and 308 are to the bottom wall. The inner surface of OD is covered with Tyvec sheets, which is known as a reflective material, in order to maximize the light detection efficiency. The OD is used as a veto-counter to identify incoming cosmic-ray muons. The water of 2 m thickness in OD also acts as a shield against gamma-ray and neutron backgrounds from the surrounding rock.

4.3 Photo Multiplier Tubes

Inner PMT

Figure 4.3 shows the schematic view of the 20-inch PMT (Hamamatsu R3600). It is improved in timing and energy resolution over those used in Kamiokande [26]. Specifications of the PMT are summarized in Table 4.1. The photo-cathode is made by bialkali (Sb-K-Cs) that is suitable for the collection of Čerenkov light. The quantum efficiency is 22% at the wavelength of 390nm (Figure 4.4). A Venetian-blind type dynode is used. The average collection efficiency is about 70%. The PMT can distinguish the single photo-electron (p.e.) as shown in Figure 4.11. Figure 4.5 shows a typical transit time spread. To obtain the uniform response of PMTs, the magnetic filed in the detector is kept less than 100 mG. There are 26 sets of Helmholtz coils arranged in the tank to compensate the geo-magnetic filed.

Outer PMT

The 8-inch PMTs used in the outer detector (Hamamatsu R1408) were adapted from the IMB experiment. The timing resolution of the PMT is about 5.5nsec. A 60 cm × 60 cm × 1.3 cm wavelength shifter is attached to each PMT to increase the light collection efficiency. The wavelength shifter increases the light collection by $\sim 60\%$, while the timing resolution becomes worse to ~ 7.5nsec. Still it is enough for tagging the events.

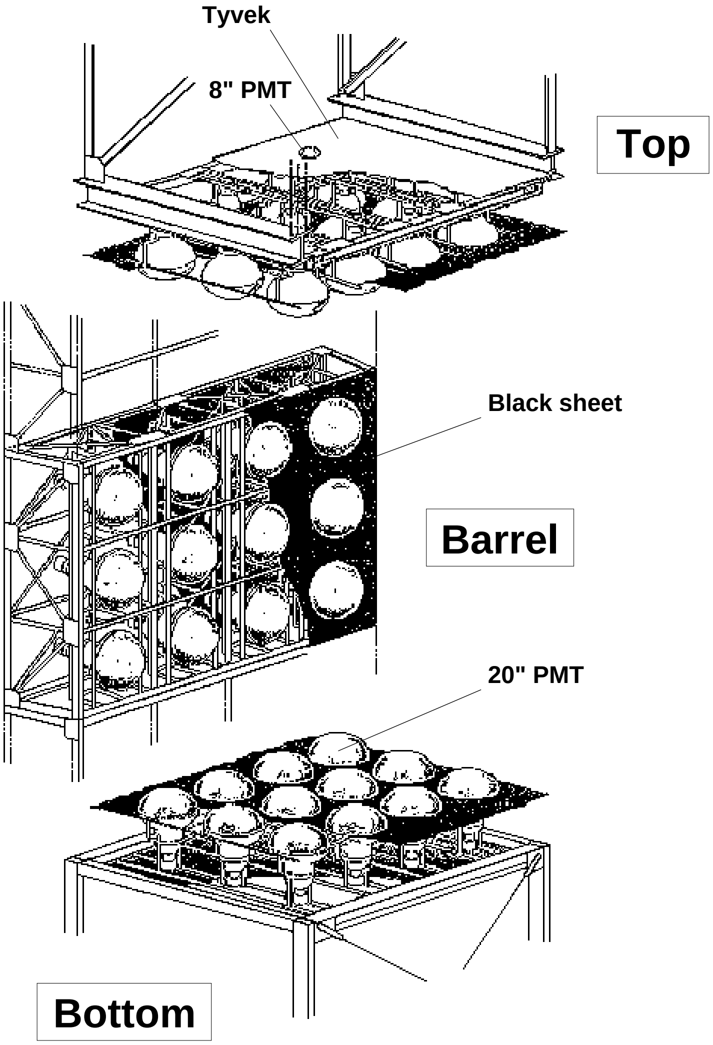

Figure 4.2: Schematic view of the frame for supporting PMTs.

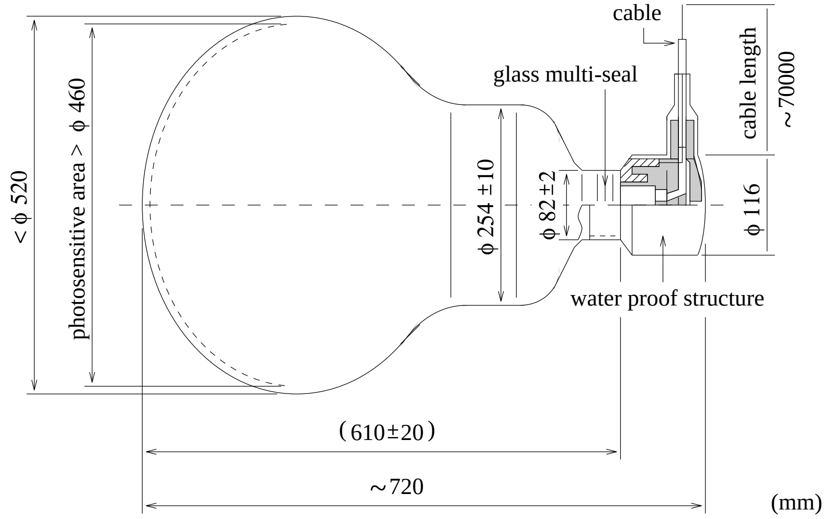

Figure 4.3: Schematic view of the PMT used in Super-Kamiokande.

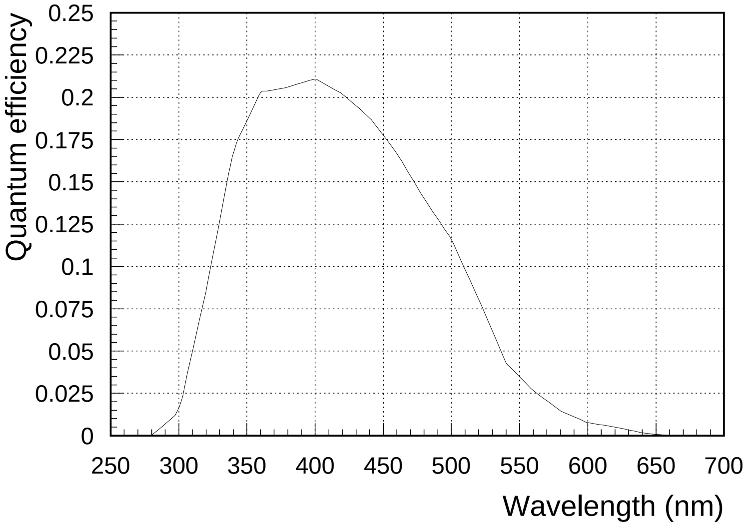

Figure 4.4: The quantum efficiency as a function of the wavelength of the light.

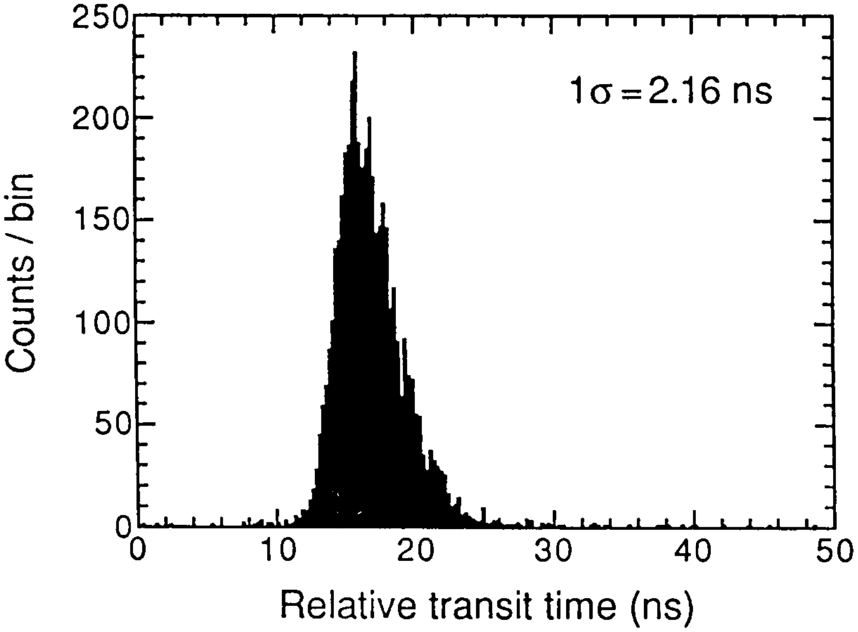

Figure 4.5: Transit time distribution of the PMT used in Super-Kamiokande.

Photo-cathode area	50 cm in diameter
Shape	Hemispherical
Window material	Pyrex glass, $4 \sim 5$ mm
Photo-cathode material	Bialkali (Sb-K-Cs)
Dynodes	11 stages, Venetian blind type
Sensitive wavelength	300 nm to 600 nm, peak at 390 nm
Quantum efficiency	22% at $\lambda = 390$ nm
Typical gain	10^7 at ~ 2000 V
Dark current	200 nA at gain 10^7
Dark noise rate	3 kHz at gain 10^7
Cathode non-uniformity	less than 10%
Anode non-uniformity	less than 40%
manufactured	Hamamatsu Photonics K.K.

Table 4.1: The specifications of the 20-inch PMT.

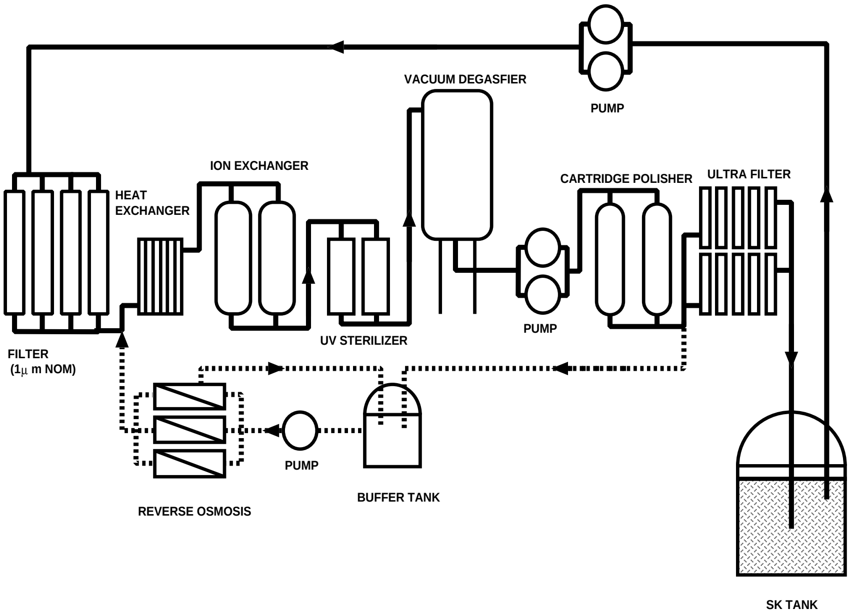

Figure 4.6: Flow diagram of the water purification system.

4.4 Water and Air Purification System

The 50 kt pure water filled in Super-Kamiokande was produced from the natural underground water flowing near the detector site. This water is circulated through a water purification system to keep the water transparency as high as possible and to remove radioactive materials such as Rn, Ra and Th. Radioactive materials, especially ^{222}Rn, become a serious background against the solar neutrino analysis and determines the analysis threshold. There is about 60 cm space between the surface of the water and the top of the tank. Radon free air is sent into this region to prevent Rn not to dissolve in the water.

Water Purification System

Figure 4.6 shows the flow diagram of the water purification system. The solid line shows the main circulation of water and the dotted line shows the supplementary one. The 1 μm filter removes small dusts. The heat exchanger keeps the water temperature at about 13 °C to suppress the bacteria growth. The ion exchanger and cartridge polisher remove metallic ions such as Fe^{2+}, Ni^{2+}, Co^{2+}. The ultra-violet sterilizer kills bacteria in the water. The vacuum degasifier removes gas resolved in the water. It is able to remove about 99% of oxygen gas and 96% of Rn gas. The ultra filter removes finer dust of the order of 10 nm.

The flow rate is about 50 tons/hour. The system keeps the light attenuation length to about 100 m at the wavelength of 420 nm.

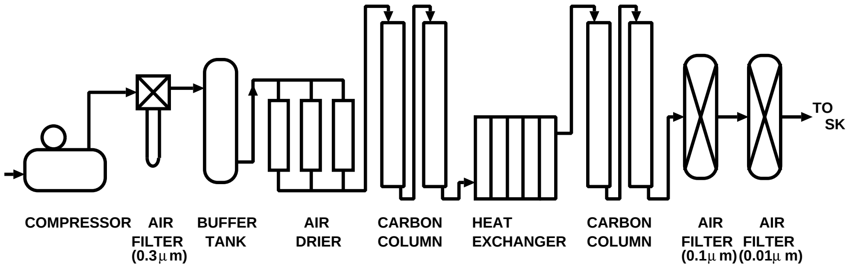

Figure 4.7: Flow diagram of the radon free air system.

Radon Free Air System

Radon free air system is located at the entrance of the mine. Figure 4.7 shows its flow diagram. The compressor compresses the air to 7.0 ∼ 8.5 atm. The air dryer before the carbon column removes moisture in the gas to improve the efficiency of removing Rn by carbon column. The concentration of Rn in the air through this system is reduced to the order of 10^{-3} Bq/m^3, while that of the mine air is of order of 10 ∼ 1000 Bq/m^3, which changes seasonally due to the change of flow of the mine air.

4.5 Data Acquisition System

Inner Electronics

A block diagram of the electronics for ID is shown in Figure 4.8. The system has two types of crates, TKO(TRISTAN/KEK Online) crates [27] and VME crates. There are 48 TKO and 8 VME crates in total and they are distributed in 4 electronics huts. One VME module for the global trigger (TRG module) is located in the central hut. All the huts are constructed on the top of the water tank. Each TKO crate has up to 20 Analog Timing Modules (ATMs) [28], one Go/NoGo (GONG) trigger module and one Super-Controller Header bus interface (SCH) module. A total of 934 ATMs are used.

The main function of ATM is to digitize signals from PMTs and to make trigger signal. Each ATM has 12 PMT input channels. It digitizes both timing and charge information of the PMT signal, providing a 1.3 μsec full range in time with 0.4 nsec resolution and 600 pC full range in charge with 0.2 pC resolution. There are two time-to-analog converters (TAC) and charge-to-analog converters (QAC) for each channel, so that two successive events, such as a stopping muon and a decay electron accompanied to it, can be acquired without dead time.

Each input signal is amplified by factor of 100 and fed to a discriminator. The threshold is set to 100 mV which is equivalent to about 1/4 p.e.s. When input signal exceeds this threshold, a rectangular pulse with 200 nsec in width and 15 mV in height is generated. Simultaneously, a gate window of 900 nsec in width is opened to start time measurement in TAC and charge accumulation in QAC, which accumulates charge in the 400nsec time window. The rectangular pulses from the all the hit PMTs are summed up (called “HITSUM” signal) and sent to the global trigger module in the central hut. If the global trigger does not arrive within 1.3 μsec, the stored information in TAC and QAC is cleared. Otherwise, charge and timing information

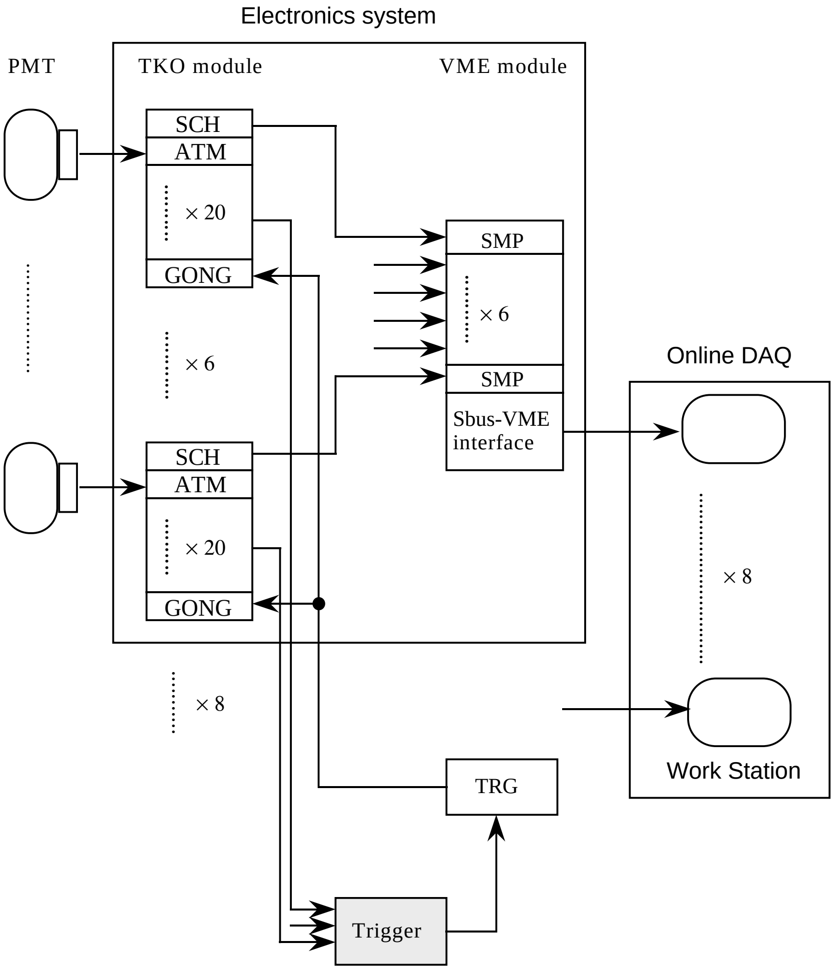

Figure 4.8: Schematic view of ID data acquisition system.

are digitized by ADC and sent to the memory (SMP) in the VME module via SCH.

Pedestals of ATMs are measured every 30 minutes. Only 1/8 of all the ATMs are measured at once in order not to miss supernova neutrino events.

Outer Electronics

Figure 4.9 shows a quadrant of the OD electronics. There are 40 paddle cards, 10 charge-to-timing converter (QTC) modules, 5 time-to-digital converters (TDCs) and one FASTBUS smart crate controller (FSCC) in each quadrant.

The paddle card has 12 PMT channels. It picks up the PMT signal through a high voltage capacitor since the signal and high voltage lines are AC coupled. The QTC module converts a PMT signal into a logic pulse (ECL level), whose leading edge corresponds to the arrival time of signal and its width is proportional to the integrated charge of the PMT pulse. The QTC module also provides a HITSUM signal and sends it to the trigger module located in the central

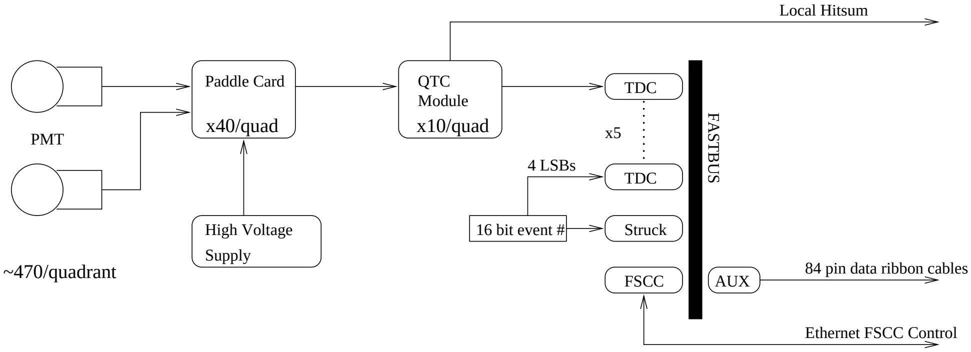

Figure 4.9: Schematic view of OD data acquisition system.

hut. The HITSUM signal is a rectangular pulse with 200 nsec in width and 20 mV in height.

LeCroy model 1877 Multi-hit Time-to-Digital Converter is used for the TDC module. It has up to 96 ECL level inputs per one module. The minimum time unit of the TDC is 0.5 nsec. It serves as a pipeline buffer, which can record 16 of the most recent signals within 32 μsec window. The time window was set to the full 32 μsec centered around the trigger time for the early period of the operation. In September 1996, this width was cut to 16 μsec (-10 to +6 μsec to the global trigger) to reduce the amount of data. The control and read-out of the TDC modules are given by FSCC and the stored data are sent to the online machine through a VME bus.

In addition to the PMT information, GPS timestamps are taken by the VME module for the OD electronics.

Trigger

The Super-Kamiokande detector has three types of triggers for ID, named High Energy (HE) trigger , Low Energy (LE) trigger and Super Low Energy (SLE) trigger, and one trigger for OD. The global trigger is generated independently when any one of these four triggers is generated.

The HE trigger is used mainly to record K2K-beam neutrinos, cosmic ray muons, atmospheric neutrinos and proton decay candidates. Its threshold is set to 340 mV, which corresponds to 31 hits in 200 nsec time window. The trigger rate is about 5 Hz. The LE trigger is used for solar neutrino analysis above 5$\sim$6 MeV in the energy. The threshold is set to 320 mV corresponding to 29 hits in 200 nsec time window, or approximately 6.5 MeV for electrons. Typical trigger rate is about 11 Hz. The OD trigger is used to reject the cosmic ray muons. Its threshold is set to 19 hits in 200 nsec time window. The SLE trigger started from May 1997 in order to push the analysis threshold of solar neutrino energy spectrum down to 4.6 MeV. The SLE triggered events are not used at all in the K2K experiment and removed at the first step of the data reduction.

The GPS timestamp is acquired if an HE trigger or OD trigger is generated and read out through online workstations.

4.5.1 Online and Offline System

The online system consists mainly of eight front-end workstations for collecting data of ID, one front-end workstation for OD and one host workstation to control run status and collect data from 9 front-end workstations. Each front-end workstation reads out the data from electronics when the global trigger is generated, and transfers it to the host workstation via FDDI network. The host workstation merges all the information of hit PMTs for both ID and OD, and records as one event. The sequence of data is written into a data file at every about 90 seconds. The data size is about 200 MBytes. They are then sent from the detector site to an offline computer facility outside of the mine via optical fiber. The offline host computer saves all the data into a magnetic tape library. At the same time, ADC and TDC counts of the PMTs are converted to units of p.e. and nanosecond, respectively, taking account of the pedestal and the calibration constant. Several primary reductions for different physics, including the K2K first reduction, run in parallel with a total of 28 CPUs in order to process a large amount of data speedily. The reduced data are also stored to the tape library and subsequent proper reductions are processed by each analysis group.

4.6 Calibration

4.6.1 Relative Gain Calibration

A Xe lamp and scintillation ball system was used to calibrate the relative gain of PMTs (Figure 4.10). The light from the Xe lamp was passed through a UV filter to adjust the wavelength for which the scintillation ball absorbs, and a ND filter to change light intensity. Then the light is fed into the scintillation ball in the tank via an optical fiber. The scintillator ball is made of acrylic resin, which uniformly contains 50 ppm of BBOT wavelength shifter and 500 ppm of MgO diffuser. The typical wavelength of the light emitted from the scintillation ball is 440 nm, which is similar to that of Čerenkov light.

The high voltage supplied to each PMT is determined so that all the PMTs have a common gain. The distance from the scintillation ball, light attenuation, acceptance of the PMT, and uniformity of the ball are taken into account. To minimize the position dependence, the gain of each PMT is measured by changing the height of the ball at various positions in the detector. The relative gain spread after adjusting high voltage is about 7%. The remaining difference is later corrected by software.

4.6.2 Absolute Gain Calibration

The absolute gain of the PMT is determined by using charge distribution of single p.e. signal, which is obtained by the low energy gamma emission from thermal neutron capture of Ni. ^{252}Cf is used as a neutron source. A cylindrical polyethylene vessel, which contains Ni wires, ^{252}Cf and water, was located at the center of the inner detector. The energy of the gamma ray is about $6 \sim 9$ MeV, corresponding to $50 \sim 80$ p.e.s, therefore the number of photon observed in a PMT is at most one. Figure 4.11 shows the single p.e. distribution. Horizontal axis shows the observed charge in unit of pC. From this calibration, a single p.e. is determined to be 2.055 pC [29].

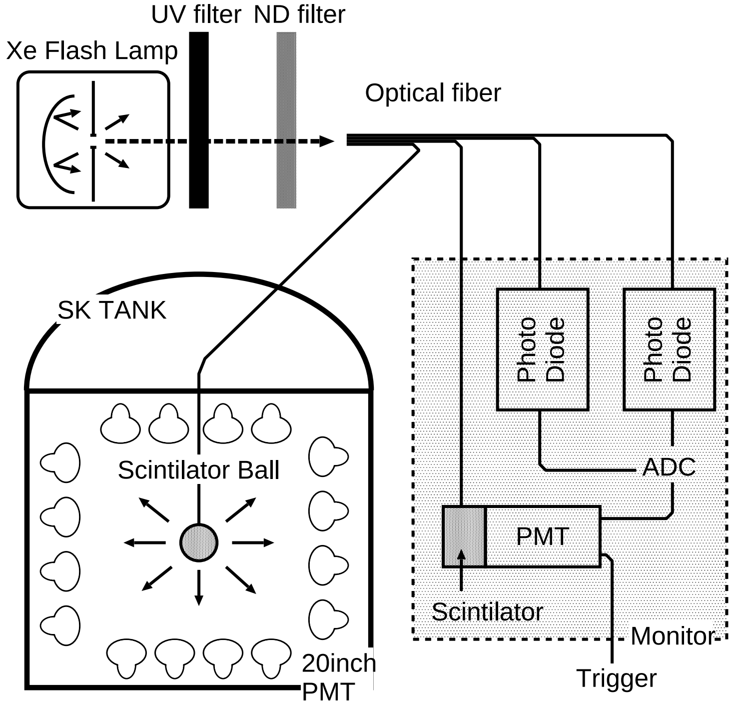

Figure 4.10: Setup of the Xe lamp and scintillation ball system for the relative gain calibration.

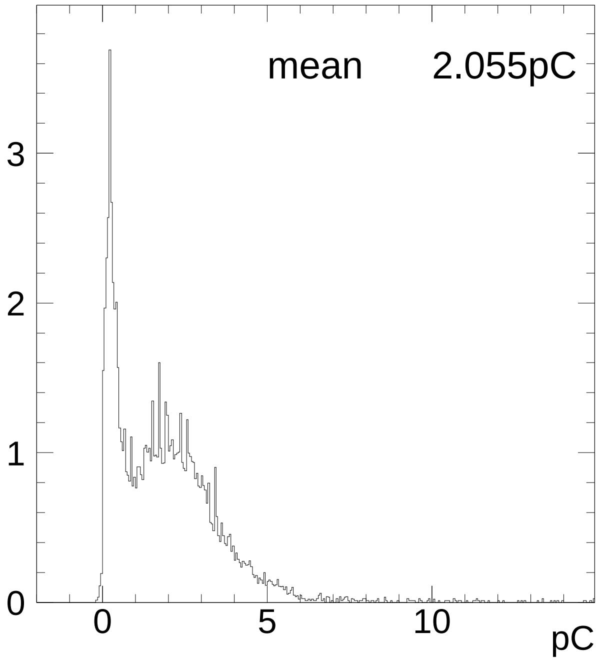

Figure 4.11: Single photo-electron induced charge distribution of the 20-inch PMT. The large spike around 0 is caused by the photo-electron going through the first dynode.

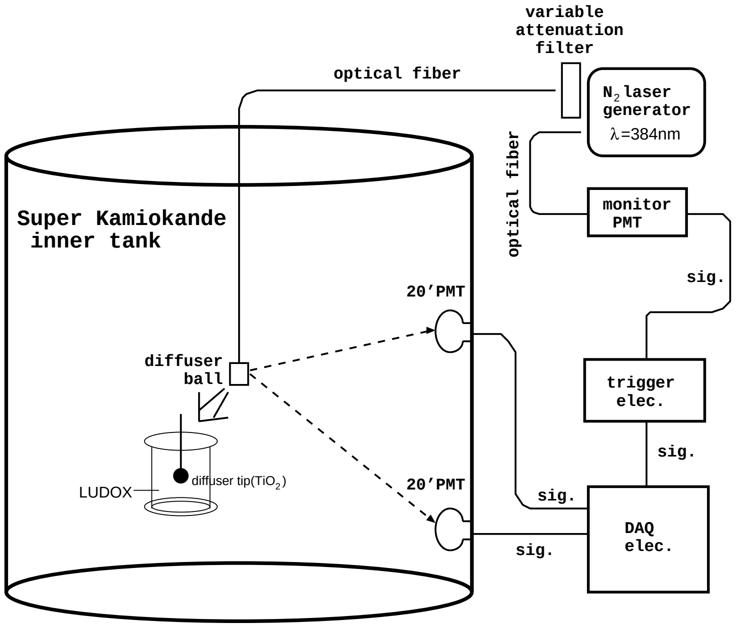

Figure 4.12: Relative timing calibration system using laser light source.

4.6.3 Timing Calibration

The hit timing changes as a function of pulse hight of the PMT caused by the slewing effect in the discriminator. Its calibration is important for reconstruction of vertex position because the vertex fitting largely depends on the timing information of each PMT.

A laser light and diffusing ball is used for the relative timing calibration (Figure 4.12). Light from a dye laser, pumped by a pulsed N_2 laser, is fed into the diffusing ball via an optical fiber. The timing response is measured at various light intensity. The wavelength of the dye laser is 384 nm, which is near to that of Čerenkov light. The time width of laser pulse is less than 3 nsec. Figure 4.13 shows the typical two-dimensional plot of timing and charge.

4.6.4 Water Transparency

The water transparency is an important factor to determine the energy of an event. It was estimated by two independent methods. One is a direct measurement by a dye laser and a CCD camera. This method measures the wavelength dependence of the attenuation length by changing the dye module. The laser light is injected into an acrylic diffuser ball in the tank and its intensity is monitored by the CCD camera at the top of the tank. The light attenuation is measured by changing the height of the ball in the detector. Figure 4.14 shows the attenuation length at various wavelength.

The other method is by comic ray muons. The cosmic ray muons can be used as a calibration

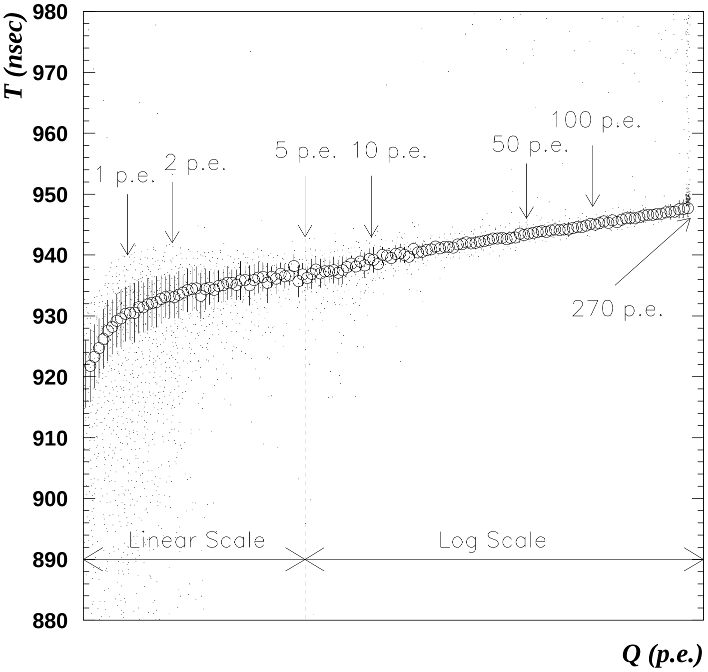

Figure 4.13: Relation between charge(Q) and timing(T) for a typical PMT. Circles and error bars show peak values and resolutions (1σ level).

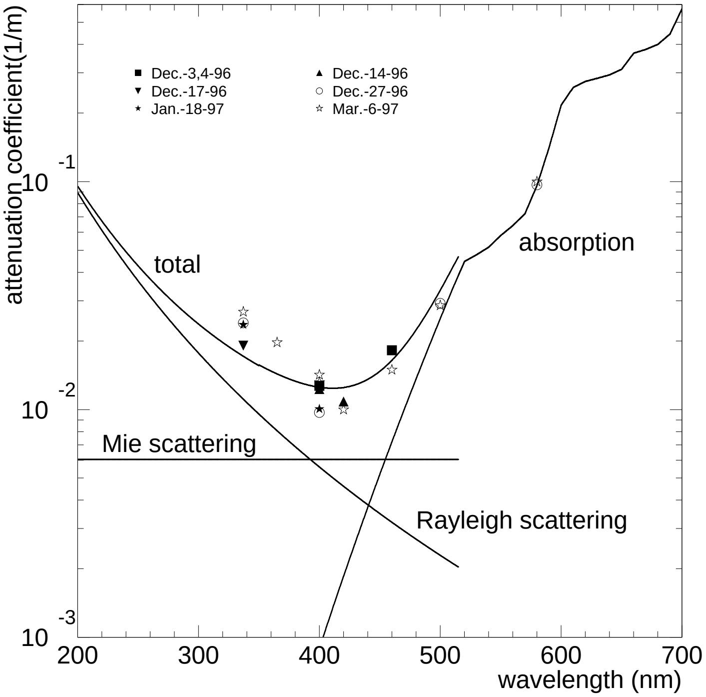

Figure 4.14: Attenuation coefficient as a function of wavelength. Solid lines show the attenuation length used in the detector simulation.

source because their dominant interaction with water is the ionization loss. The energy deposit by a cosmic ray muon in the detector is almost independent of its energy (~ 2.5 MeV/cm). This method cannot measure the wavelength dependence but measures the transparency averaged over the wavelength without disturbing the normal data taking. The attenuation length is estimated to be more than 90 m by selecting vertical-going muons entering from the top of the tank and exiting to the bottom.

4.6.5 Absolute Energy Scale

It is important to understand the absolute energy scale of the detector to reconstruct the energy of an event precisely. There are four calibration sources for the absolute energy determination; An electron linear accelerator (LINAC), decay electrons from stopping comic ray muons, π^0 invariant mass and stopping comic ray muons.

LINAC is used to understand the performance of the detector for low energy events [30]. The energy of electrons is adjustable from 5 to 16 MeV, and can be injected into various position of Super-Kamiokande through a beam pipe. Electrons of 16 MeV were injected at 6 m from the ID top wall and the momentum distribution was compared with a Monte Carlo simulation.

For the energy region of a few tens of MeV, decay electrons from muon decays are used. The mean value of the energy spectrum of the muon decay electron is compared with a Monte Carlo simulation.

The relation between the Čerenkov angle and the momentum for low energy stopping muons of $\lesssim$350 MeV/c are used to check the energy scale. The Čerenkov angle is determined by the momentum of the particle as described in Equation 4.1. The ratio of the reconstructed momentum to that estimated from the Čerenkov angle is compared between the data and a Monte Carlo.

The momentum of the high energy stopping muon can be estimated from the track length of the muon, because its energy deposit in the detector is almost independent of the muon energy (~ 2.5 MeV/cm). The stopping muons whose track length is greater than 7 m, which corresponds to the energy more than about 1.7 GeV, are used. The (momentum)/(track length) ratio is compared between the data and a Monte Carlo.

Figure 4.15 summarizes the absolute energy scale calibration. Events with the momentum from 16 MeV/c to about 10 GeV/c are examined. The uncertainty is estimated to be within $\pm 2.5\%$.

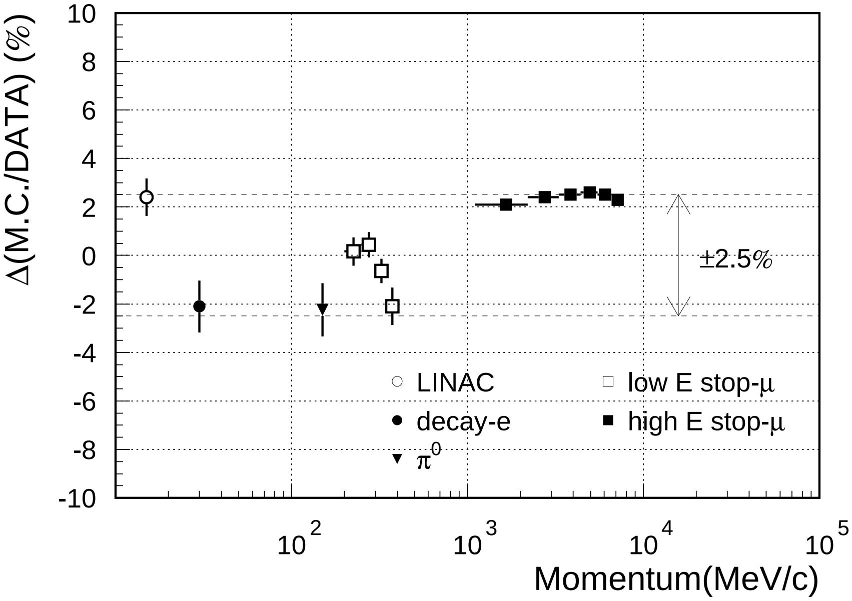

Figure 4.15: Absolute energy scale for the several calibration source.

Chapter 5

Timing Synchronization using GPS

Since it is extremely hard to connect KEK to Super-Kamiokande with cables, Universal Time Coordinate (UTC) timestamps provided by Global Positioning System (GPS) is used to identify beam neutrino event at Super-Kamiokande. The relative timing difference of GPS timestamps in Super-Kamiokande and KEK is confirmed by means of an atomic clock.

5.1 Global Positioning System

Figure 5.1 shows the schematic view of the GPS system used in the K2K experiment. The system consists of three components: the GPS receiver, VME receiver module and Local Time Clock (LTC). Each component of the GPS system and the method to obtain event trigger time are briefly described.

In the Super-Kamiokande site, the GPS receiver and antenna are located at the entrance of 1.7 km-long access tunnel to Super-Kamiokande, and the other components are located in the central hut. The GPS receiver and the VME receiver module are connected via an optical fiber through the tunnel. The GPS system in the KEK site is almost identical to that of Super-Kamiokande. The whole GPS system is located in the beam control room.

Overview of GPS

GPS is a Satellite Navigation System founded and controlled by the U.S. Department of Defense (DOD). There are 24 satellites in six orbital planes (Figure 5.2). Satellite orbits are controlled by the Master Control Station located at Schriever Air Force Base in Colorado. Each satellite has an atomic clock, which is referenced to the Master Clock at the U.S. Naval Observatory (USNO) and steered to UTC. These satellites send the time and orbital information by radio wave. A GPS receiver computes its position and time by receiving four GPS satellite signals.

GPS receiver

TrueTime Model XL-DC-602 GPS receivers are used for K2K experiment. The accuracy is better than 40 nsec in average and 150 nsec at the worst. Two outputs are provided by the receiver: a standard serial time code format, known as IRIG-B code, and 1 Hz square wave whose leading edges are synchronized to seconds roll-overs in UTC.

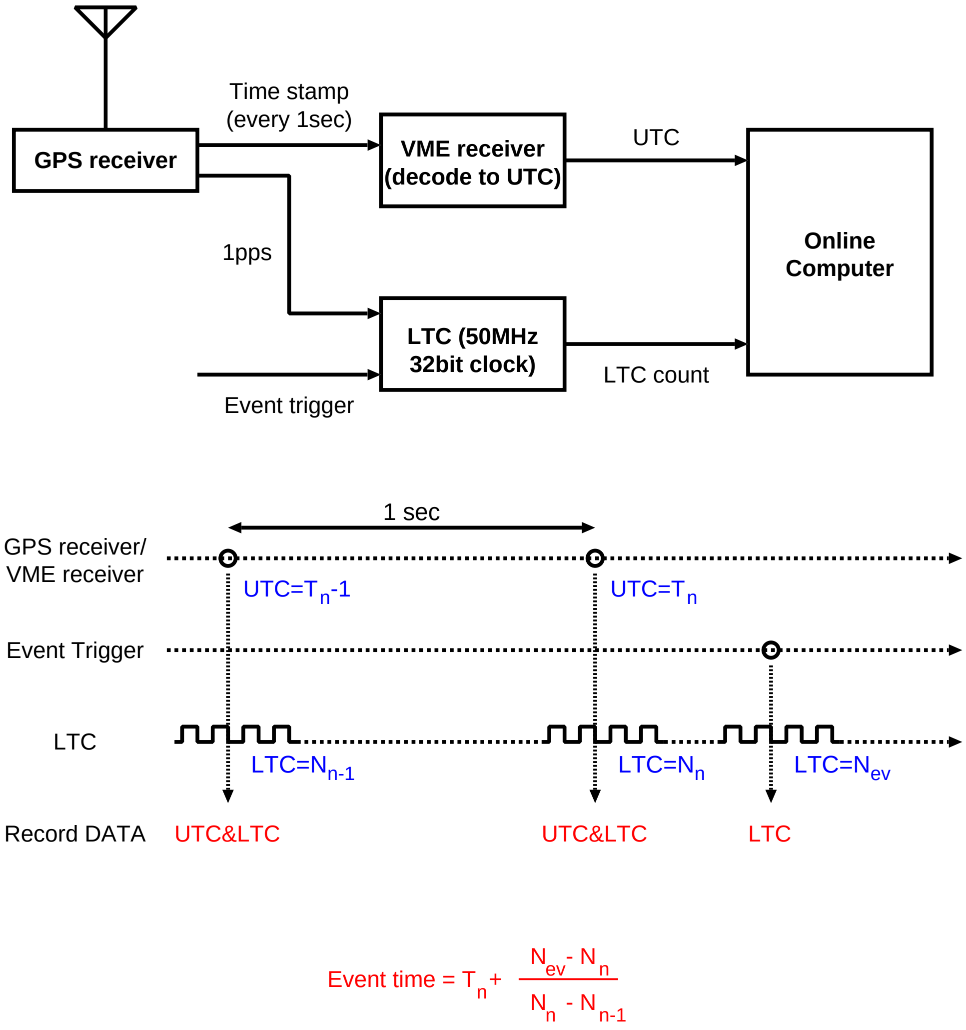

Figure 5.1: Schematic view of the GPS system

Figure 5.2: Schematic view of orbits of GPS satellites.

The IRIG-B code contains one "frame" per one second on 1 kHz carrier. Each frame can be divided into 100 elements, each of which has length of 10 msec. Three types of elements are defined: binary zero ("0"), binary one ("1") and position marker ("P") (Figure 5.3). Each frame starts with two "P". A frame is divided into 10 sets of 10 elements. Each set contains two BCD-coded binary numbers, separated by a "0" from each other, and terminated by a "P". The sets contain day of year, hour, minute, second data and status of the GPS receiver.

VME receiver

The VME receiver decodes the IRIG-B code to UTC timestamp, which is expressed by the number of seconds elapsed since 00:00:00 on January 1, 1970.

Local Time Clock

The Local Time Clock (LTC) is a free-running 50 MHz 32bit clock counter. It has two inputs: one for 1 pps signal from the GPS receiver and the another is for the event trigger (spill trigger in KEK, logical OR of the HE trigger and OD trigger in Super-Kamiokande). Counts of the LTC is recorded when it receives the 1 pps signal or an event trigger. The frequency of the 50 MHz clock is calibrated using 1 pps signal and corrected in software (Figure 5.4).

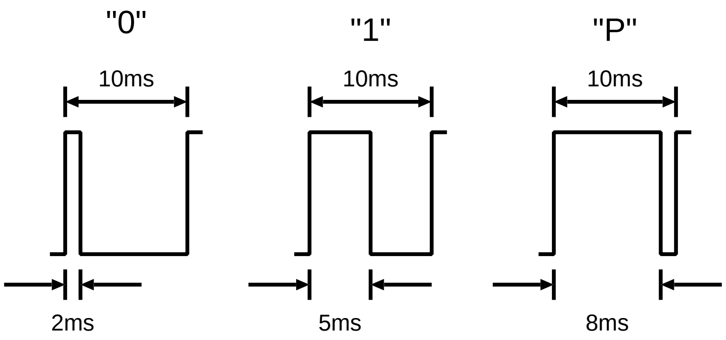

Figure 5.3: Elements of the IRIG-B code

Event Trigger Time

The time of the event trigger T_{ev} is obtained by linear interpolation as following:

$$T_{ev} = T_n + \frac{N_{ev} - N_n}{N_n - N_{n-1}} \tag{5.1}$$

where T_n is the timestamp of the latest 1 pps output from the GPS receiver, N_{ev} is count of LTC when it was triggered, N_n is LTC counts corresponding to T_n and N_{n-1} is LTC counts corresponding to the second latest 1 pps.

5.2 Timing Calibration using an Atomic Clock

Relative timing difference of GPS timestamps in Super-Kamiokande and KEK is confirmed by an atomic clock. The relative timing difference δT are given by:

$$\delta T = \delta T_{SK} - \delta T_{KEK} \tag{5.2}$$

$$\delta T_{SK(KEK)} = (T_{GPS} - T_{ATOM})_{SK(KEK)} \tag{5.3}$$

where T_{GPS} is the UTC provided by the GPS and T_{ATOM} is the time provided by the atomic clock, measured in Super-Kamiokande (KEK)

Atomic Clock

A cesium beam primary frequency standard, HP-5071A, one of the atomic clocks kept by Time Keeping Office, Earth Rotation Division and Mizusawa Astrogeodynamics Observatory, National Astronomical Observatory, is used. It was transported by a car from Mizusawa to KEK, Super-Kamiokande and returned back to Mizusawa after 7 days.

The accuracy is $\pm 2 \times 10^{-12}$ and the long term stability under laboratory conditions is $\leq 1.0 \times 10^{-13}$ for 5 days. The timestamp kept in the atomic clock (T_{ATOM}) is referenced to the International Atomic Time (TAI, Temps Atomique International) via one of the GPS satellites defined by BIPM (Bureau International des Poids et Mesures), but not adjusted to TAI. The difference between UTC and T_{ATOM} is about 3 μsec.

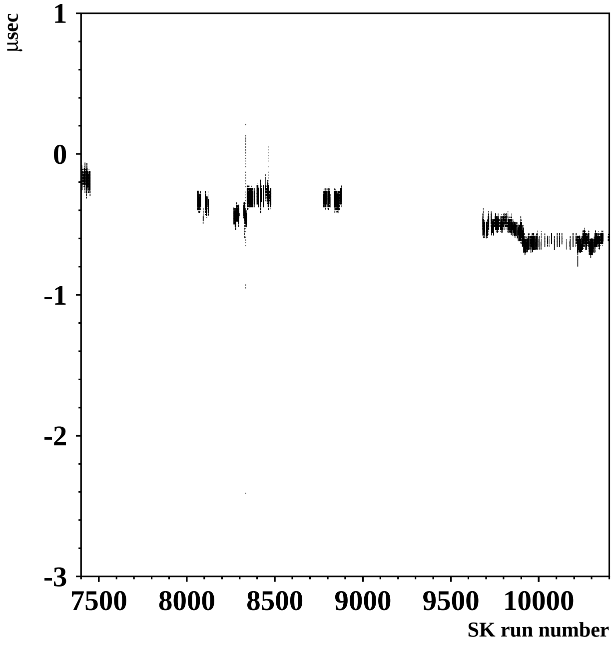

Figure 5.4: Stability of LTC in Super-Kamiokande. Vertical axis shows the drift of the LTC count from the nominal one (50 MHz), expressed by unit of μsec. Horizontal axis is the run number of Super-Kamiokande, corresponding to the whole running period.

TAI is a timestamp defined by the average of about 200 atomic clocks placed all over the world, which is independent of the Earth rotation. UTC timestamp is a compensated TAI to remain within 0.7 seconds of Astronomical Time. This compensation is known as the "leap second".

Two outputs are provided by the atomic clock: a timestamp via RS232C and 1 pps whose leading edges are synchronized to seconds roll-overs.

Setup

Figure 5.5 shows the schematic view of the setup of $\delta T_{SK(KEK)}$ measurement in Super-Kamiokande(KEK).

- **Setup in KEK**
  The 1 pps output from the atomic clock is fed to the beam-line DAQ system instead of the spill trigger. The GPS timestamp for corresponding 1 pps is acquired from the beam-line DAQ system and the atomic clock timestamp is read via RS232C port.
- **Setup in Super-Kamiokande**
  The laser system, which is used for timing calibration (Chapter 4.6.3), is triggered by the 1 pps output from the atomic clock and all the PMTs are lit. The GPS timestamp for corresponding 1 pps is acquired from the DAQ system and the atomic clock timestamp is read via RS232C port. The length of the optical fiber, time of flight of the laser light, delays in signal cables and electronics are considered.

Results

Following numbers are measured to be the time difference between T_{GPS} and T_{ATOM} in KEK and Super-Kamiokande (Figure 5.6):

$$\delta T_{KEK} = T_{GPS} - T_{ATOM} = 2366 \pm 36\text{nsec} \tag{5.4}$$

$$\delta T_{SK} = T_{GPS} - T_{ATOM} = 2481 \pm 50\text{nsec} \tag{5.5}$$

Thus the relative timing difference of GPS timestamps in Super-Kamiokande and KEK, δT is obtained as following:

$$\delta T = \delta T_{SK} - \delta T_{KEK} = 115 \pm 142(syst.)\text{nsec} \tag{5.6}$$

The systematic errors are described below.

Sources of Systematic Errors

Systematic errors on δT are summarized in Table 5.1.

- **Drift of the atomic clock.**
  The drift of the atomic clock was estimated by comparing UTC and T_{ATOM} twice in Mizusawa. The first time was before carrying the atomic clock from Mizusawa and the second was after returning to Mizusawa. The drift during the 7 days-long transportation

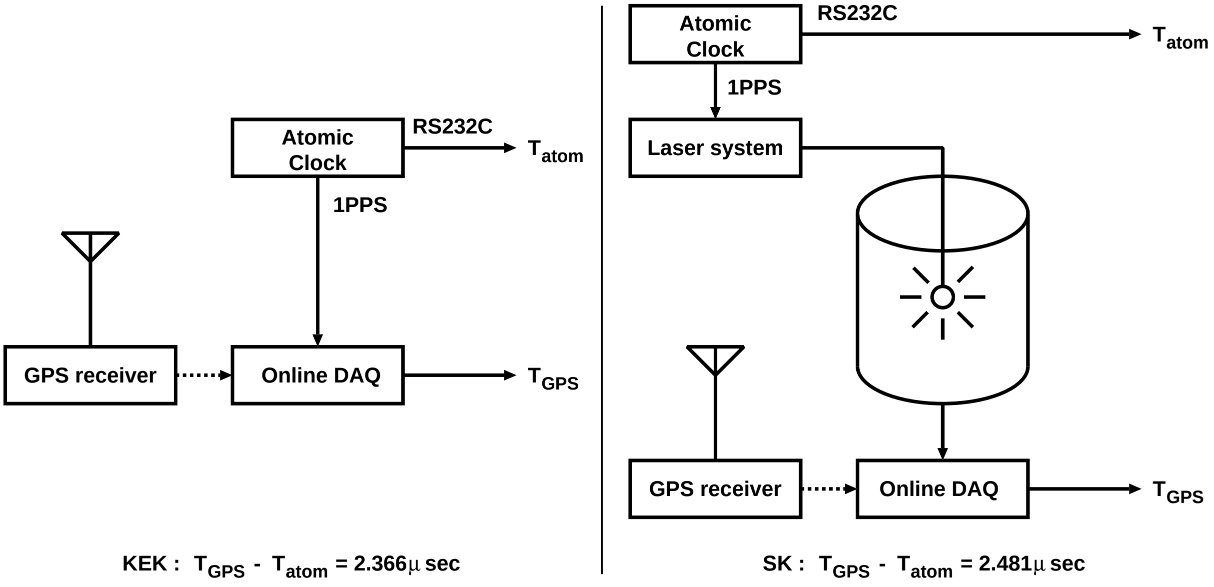

Figure 5.5: Schematic view of timing difference measurement, in KEK (left) and Super-Kamiokande (right)

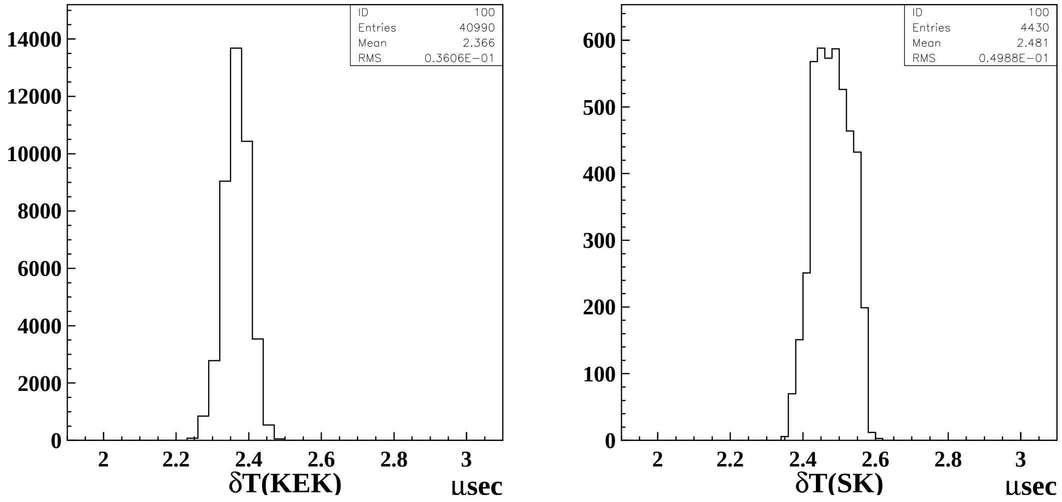

Figure 5.6: Timing difference between GPS and atomic clock, in KEK (left) and Super-Kamiokande (right)

Uncertainty in GPS (for SK)	87 nsec
Uncertainty in GPS (for KEK)	87 nsec
Drift of the atomic clock	36 nsec
RMS of δT_{KEK}	36 nsec
RMS of δT_{SK}	50 nsec
Total	142 nsec

Table 5.1: Systematic errors on the time synchronization.

of the atomic clock was 85 nsec. Assuming a linear drift of the atomic clock, an error of 36 nsec is assigned since there were 3 days of interval between measurements in KEK and Super-Kamiokande.

- **Uncertainty of GPS timestamps.**
  An error of 87 nsec is assigned for each of the Super-Kamiokande and KEK timestamps, which is the RMS error for a flat distribution with ± 150 nsec width which is maximum uncertainty of the GPS receiver.

- **The RMS of δT_{KEK} and δT_{SK}**
  The RMS errors of δT_{KEK} and δT_{SK} are estimated for the measurement error of 36 nsec and 50 nsec, respectively.

In total, an error of ± 142 nsec is assigned for the error of δT.

Chapter 6

Data reduction and results

6.1 Overview of the Analysis

In following Chapters, study of the ν_μ disappearance is described. When the number of observed events has a deficit caused by the neutrino oscillation, the reduction probability depends on the neutrino energy as shown by Equation 1.5. The oscillation parameters can be determined by fitting the distortion pattern in the measured ν_μ energy spectrum.

The number of expected neutrino events in Super-Kamiokande is calculated from the following formula:

$$N_{exp}^{SK} = N_{int}^{1kt} \cdot R^{SK/1kt} \cdot \frac{POT_{SK}}{POT_{1kt}} \cdot \epsilon^{SK} \tag{6.1}$$

where,

N_{exp}^{SK} : Number of expected neutrino events in Super-Kamiokande,
N_{int}^{1kt} : Number of neutrino interaction in the 1kt detector corrected with its event selection efficiency, ϵ^{1kt},
$R_{\nu_\mu}^{SK/1kt}$: The ratio of the number of muon neutrino interaction at Super-Kamiokande and the 1kt detector,
$POT_{SK(1kt)}$: Accumulated number of protons on the target for Super-Kamiokande (1kt),
ϵ^{SK} : Event selection efficiency at Super-Kamiokande.

The number of neutrino interactions in the 1kt detector (N_{int}^{1kt}) is described in Section 6.4. The accumulated numbers of protons on the target (P.O.T.) for SK and the 1kt detector (POT_{SK}, POT_{1kt}), and the definition of "good beam spill" to be used for analysis are described in Section 6.2.1. The event selection and its efficiency are described in Section 6.3.1, 6.4.1. The comparison between the observed and expected number of neutrino events in Super-Kamiokande is discussed in Chapter 7. The oscillation parameters ($\sin^2 2\theta, \Delta m^2$) are determined by fitting the distortion pattern in the measured ν_μ energy spectrum.

	1kt alive	1kt dead
SK alive	used (4.79×10^{19}P.O.T.)	used, need correction (0.50×10^{19}P.O.T.)
SK dead	not used	not used

Table 6.1: Chart of the definition of spills used. Values are accumulation from June 1999 to July 2001.

6.2 Operation of the Experiment

6.2.1 Good Beam Selection

A "good beam spill" to be used for the analysis is defined with the following criteria.

- The data from June 1999 to July 2001 are used.
- Exclude the period for the machine study, beam tuning, or PIMON measurement.
- Exclude the period of beam line component trouble.
- Proton intensity is greater than 1.0×10^{12} protons per pulse.
- Horn current is greater than 240(190) kA where nominal current is 250(200) kA from November 1999 to July 2001 (in June 1999).
- Super-Kamiokande is alive.

The accumulated P.O.T. for each month is summarized in Table 6.2. A total of $4.79 \times 10^{19}(4.29 \times 10^{19})$P.O.T. was used for SK (1kt) analysis. In order to make use of as many the proton beam as possible, the period when the 1kt detector was dead is also used for the analysis (Table 6.1). This effect was statistically corrected using accumulated P.O.T. in each month. The error for the correction is calculated by following formula;

$$\frac{\text{P.O.T.}_{SK} - \text{P.O.T.}_{1kt}}{\text{P.O.T.}_{SK}} \times S_{1kt}, \tag{6.2}$$

where S_{1kt} is the stability of the 1kt event rate, which is estimated to be 6 %.

6.2.2 Beam Profile and Stability Measurement

The stabilities of the neutrino beam intensity and density distribution were monitored spill by spill using MUMON. Additionally, they were confirmed during the whole running period with the ν-Fe events in MRD.

The proton beam was controlled to get the best targeting efficiency and precise aiming to Super-Kamiokande during the experiment. Figure 6.1 shows the fitted muon distribution center given by the MUMON. It was kept to the designed direction to Super-Kamiokande within ±1 mrad throughout the data taking. The intensity measured by MUMON was monitored as a indicator of muon yield efficiency (Figure 6.2).

period	Jun.99	Nov.99	Jan.00	Feb.00	Mar.00	May.00	Jun.00
Target diameter	$20mm\phi$	$30mm\phi$					
Horn current	200kA	250kA					
From	4 Jun.	29 Oct.	14 Jan.	2 Feb.	1 Mar.	11 May.	31 May.
To	26 Jun.	24 Nov.	29 Jan.	26 Feb.	23 Mar.	28 May.	21 Jun.
P.O.T.$_{SK}$($\times10^{18}$)	3.10	3.57	2.22	4.04	3.70	2.56	3.76
P.O.T.$_{1kt}$($\times10^{18}$)	2.60	2.62	1.81	3.74	3.35	2.42	3.17

period	Jan.01	Feb.01	Mar.01	Apr.01	May.01	Jun.01	Jul.01
Target diameter	$30mm\phi$						
Horn current	250kA						
From	14 Jan.	5 Feb.	8 Mar.	11 Apr.	17 May.	27 May.	1 Jul.
To	5 Feb.	8 Mar.	3 Apr.	26 Apr.	27 May.	1 Jul.	11 Jul.
P.O.T.$_{SK}$($\times10^{18}$)	3.20	5.04	4.60	2.76	1.75	6.12	1.54
P.O.T.$_{1kt}$($\times10^{18}$)	2.92	4.75	4.27	2.47	1.60	5.79	1.43

$$\begin{aligned} Total: \quad \text{P.O.T.}_{SK} &= 4.79\times10^{19} \\ \text{P.O.T.}_{1kt} &= 4.29\times10^{19} \end{aligned}$$

Table 6.2: Summary of the used P.O.T. for Super-Kamiokande and 1kt.

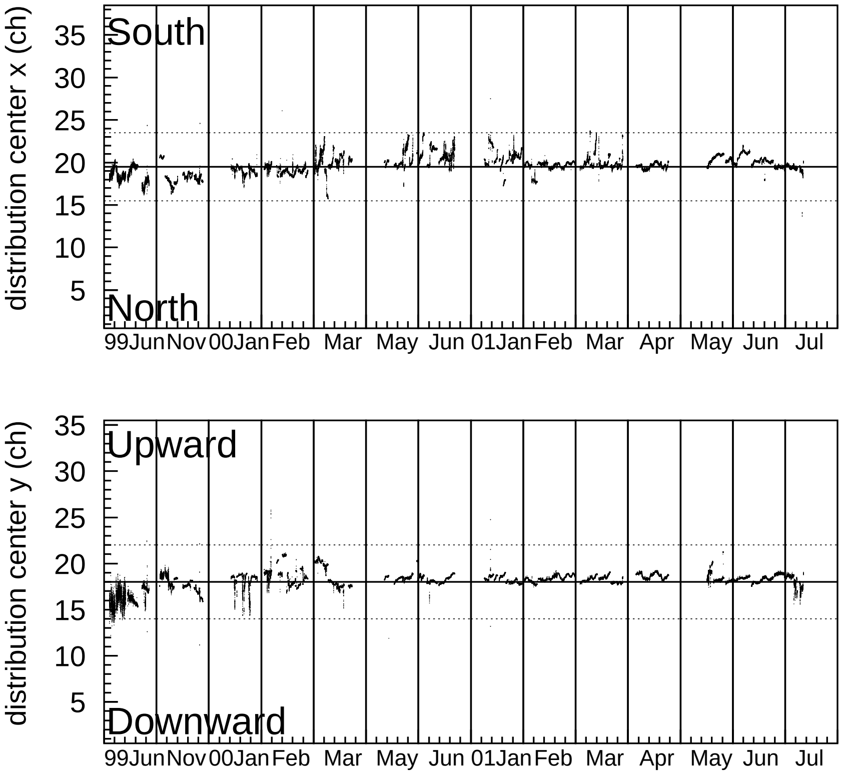

Figure 6.1: Fitted muon distribution center in the muon monitor after the beam dump, along the horizontal axis (upper) and the vertical axis (lower), averaged over 100 spills. The designed beam direction is shown in solid line in the figure. Dashed line in the figure shows the ±1 mrad boundary.

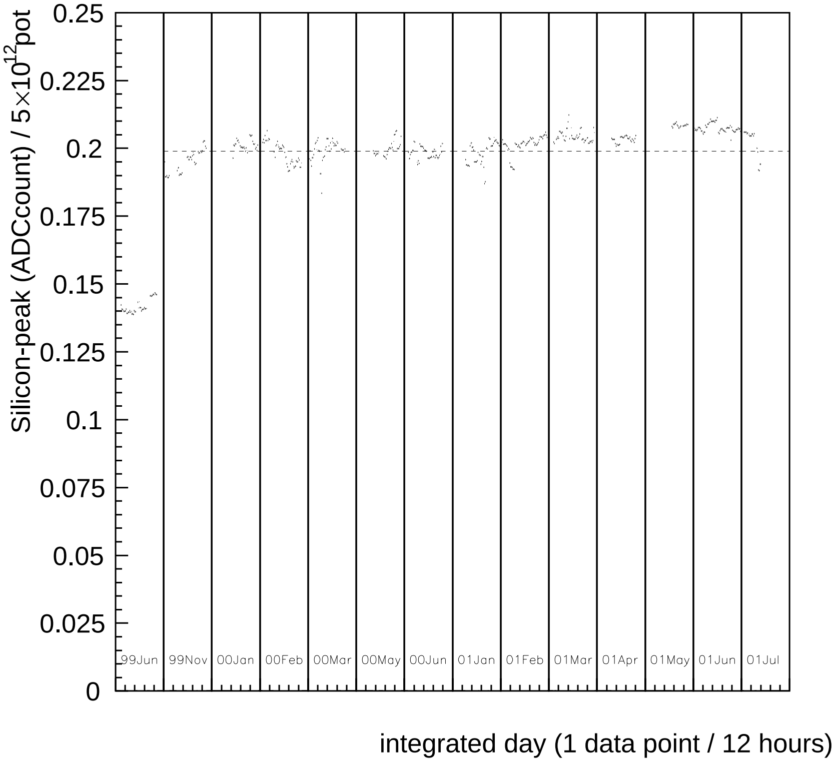

Figure 6.2: Beam intensity stability measured by MUMON, normalized to 5×10^{12} P.O.T.

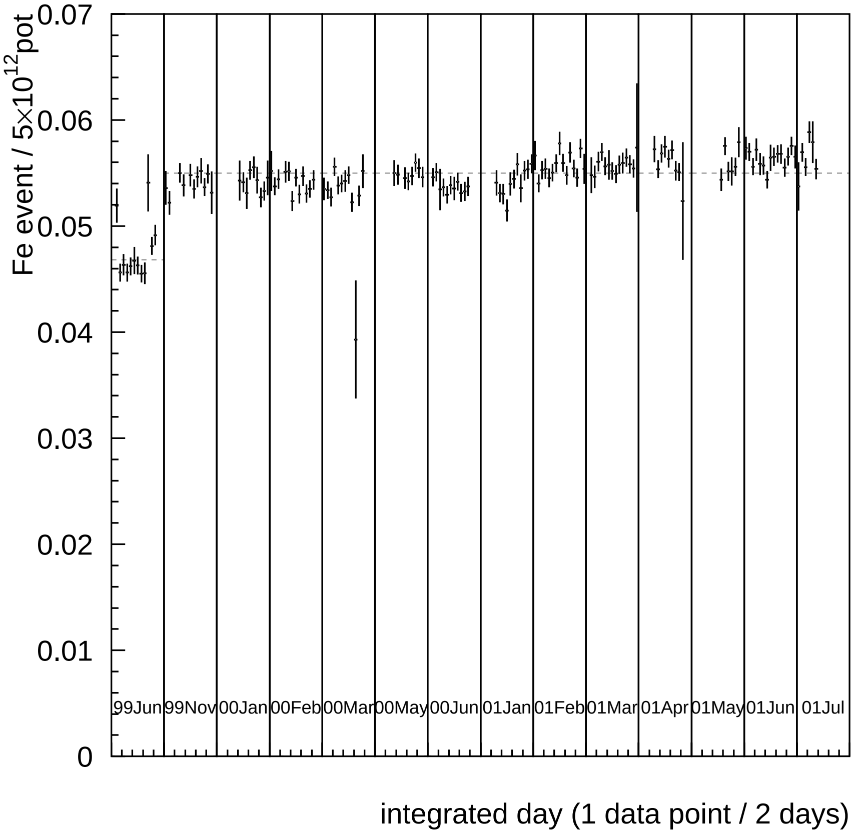

Figure 6.3: Stability of the event rate in MRD, normalized to 5×10^{12} P.O.T.The error bar shows the statistics.

Stability of the event rate in MRD, event vertex distribution, muon spectrum and angle distribution confirms the neutrino beam stability. Figure 6.3 shows stability of the event rate in MRD. There is no fluctuation except for statistical ones. Figure 6.4 shows typical vertex distribution in MRD. The neutrino beam is aimed at Super-Kamiokande within 1 mrad accuracy as shown in Figure 6.5. Figure 6.6 clearly proves the monthly stability of muon spectrum and angle distribution.

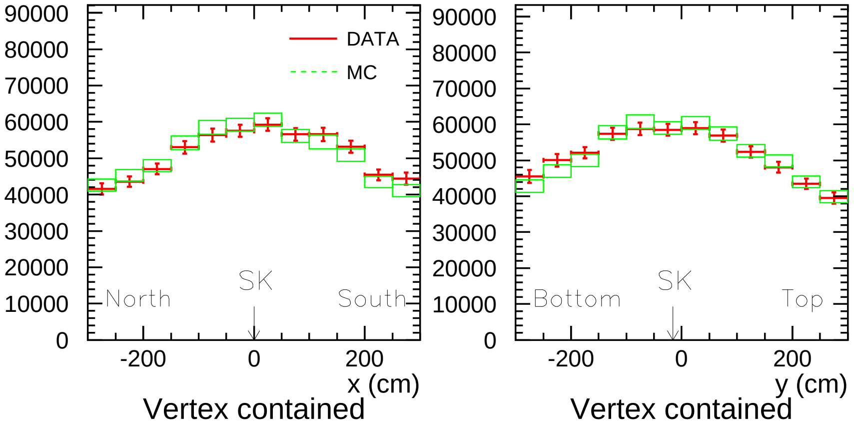

Figure 6.4: Horizontal vertex distribution in MRD (left) and vertical distribution (right) for June 1999 to July 2001; cross for the data, box for the Monte Carlo. The error bar shows the statistical error. A shift of 30 cm corresponds to 1 mrad off from the designed direction.

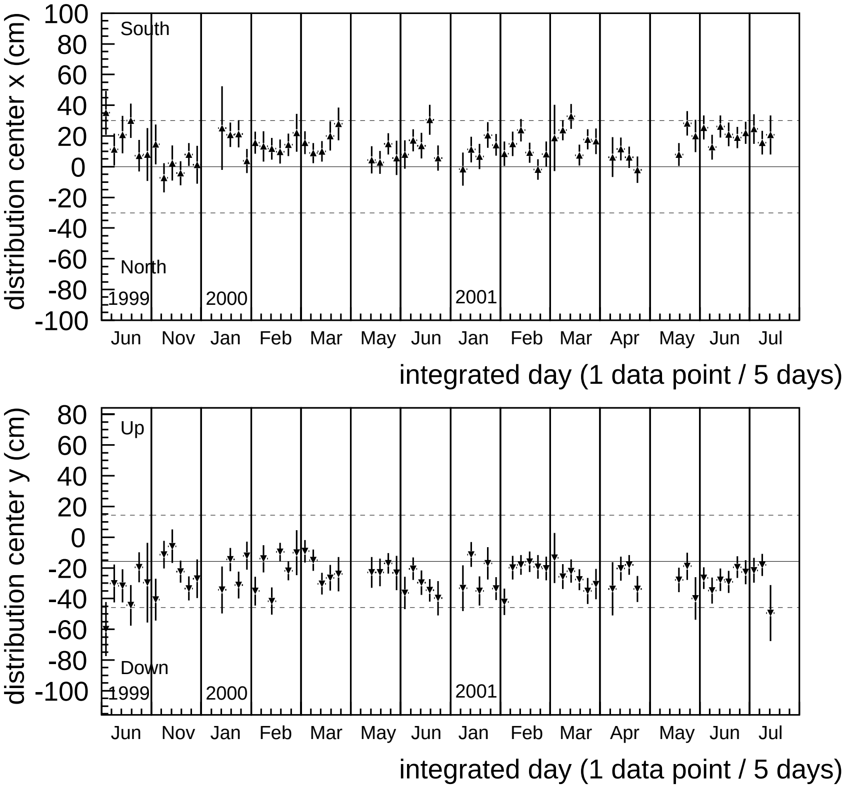

Figure 6.5: Stability of the MRD distribution center from November 1999 to July 2001 for horizontal direction (top) and vertical direction (bottom). The error bar is the Gaussian fitted error. The designed beam direction is $x = 0$ cm and $y = -15.8$ cm, shown in solid line in the figure. Dashed line in the figure means the ±1 mrad boundary.

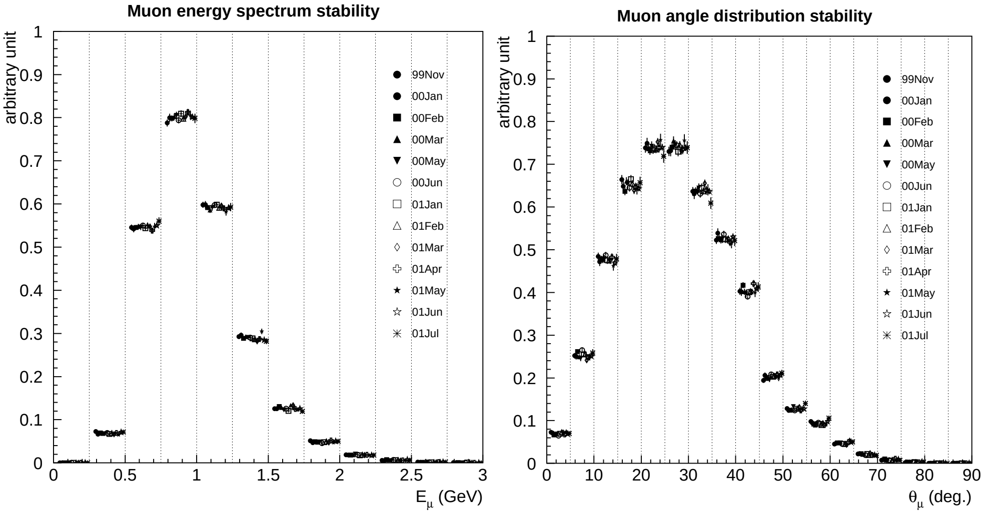

Figure 6.6: Stability of the reconstructed muon spectrum and angle in MRD, monthly variation.

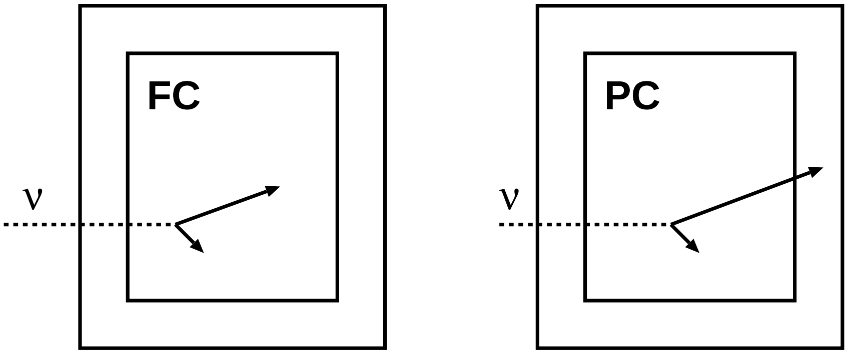

Figure 6.7: Definitions of FC and PC events. A FC event requires that all tracks of the visible particles are contained in the inner detector, whereas a PC event have at least one particle reaching the outer detector.

6.3 Reduction and Event Selection at Super-Kamiokande

6.3.1 Event Selection at Super-Kamiokande

K2K beam oriented neutrino candidate events at Super-Kamiokande are selected from a large number of cosmic ray background, radioactive background and natural neutrino events.

For this purpose two Universal Time Coordinate (UTC) timestamps from the GPS system, T_{KEK} for the start time of the beam spill at KEK-PS and T_{SK} for the observed time in Super-Kamiokande, are compared. The time difference ΔT is defined as follows;

$$\Delta T \equiv T_{SK} - T_{KEK} - TOF \tag{6.3}$$

where TOF ($= 833\ \mu$sec) is the time-of-flight of neutrino from KEK to SK. ΔT should distributed around the time window from 0.0 μsec to 1.1 μsec matching with the width of the beam spill.

Neutrino events can be classified into two event categories according to their event topology. One is the fully-contained (FC) event for which the whole visible energy is contained within the inner detector. Momenta of the emitted particles can be measured since all of the particle energies deposited inside the inner detector and the particle type can be identified by the Čerenkov ring pattern. Another is the partially-contained (PC) event for which some energy is carried out by an exiting charged particle in the outer detector. Figure 6.7 illustrates the definition of the FC and PC events.

In this thesis, FC samples are selected with following data reduction which is similar to that of the atmospheric neutrino analysis in Super-Kamiokande. Figure 6.8 shows a typical FC event. There is no energy deposit in the outer detector. An FC event which is identified to be muon (electron) by the particle identification program is called "muon-like"("electron-like") (subsection C.4).

The selection criteria are described below for each step, and the number of selected events is summarized in Table 6.3.

1 **Good beam spill selection**
The "good beam spills" are used, as described in Subsection 6.2.1.

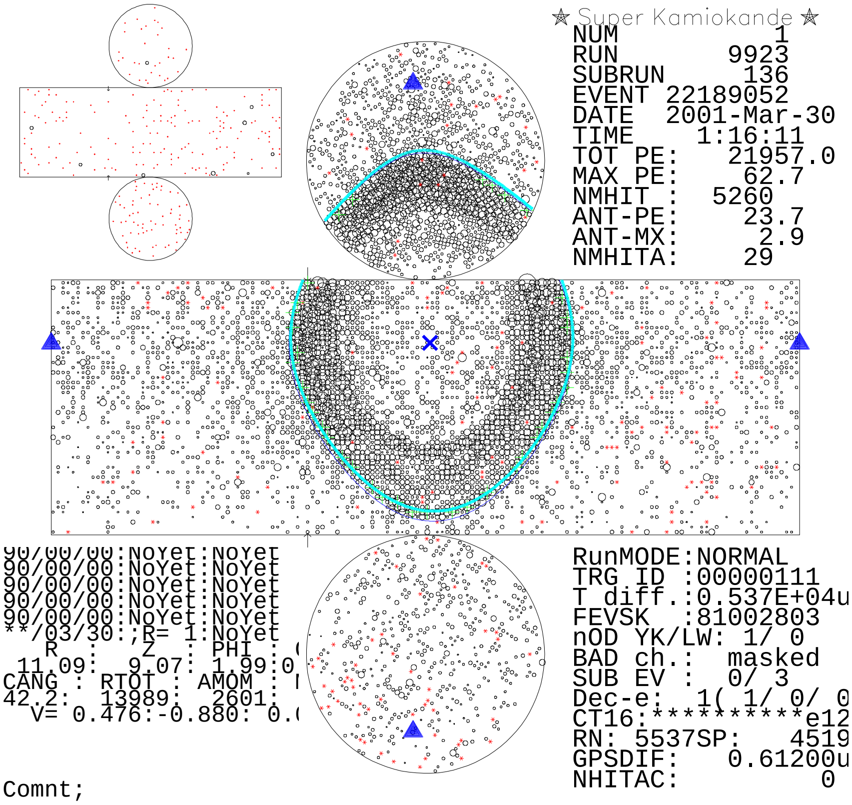

Figure 6.8: Visual display of a typical FC μ-like event, shown in the exploded view of the cylindrical tank. The left upper part of the display shows the outer detector.

	Selection	DATA	MC
1	Analyzed number of spill	9177578	
	(MC) generated in the tank		191346
	(MC) generated in the fiducial volume		88516
2	Rough timing cut	161763	
3	Decay-electron cut	107892	
4	Total photo-electron cut	18902	119571
5	Flashing PMT cut	18617	116168
6	Outer detector cut	108	101265
7	Fitting goodness cut	107	101189
8	Visible energy cut	100	98291
9	Scanning	94	
10	Fine timing cut	91	
11	Fiducial volume cut	56	69387

Table 6.3: Summary of the number of selected events in each step.

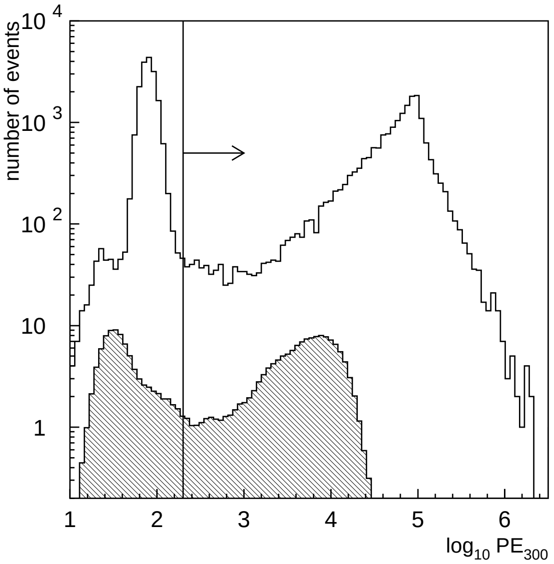

Figure 6.9: Distribution of total p.e.s in 300 nsec time window (PE_{300}); open histogram for the raw data, the hatched one for neutrino beam Monte Carlo events, normalized by its expected number of event by equivalent P.O.T.

2 Rough timing cut
From all of the triggered events in Super-Kamiokande, events inside $|\Delta T| \leq 500$ μsec time window matching to each of the good beam spill are selected at this stage.

3 Decay-electron cut
If a muon stops inside the tank, an electron produced by the muon decay makes a Čerenkov ring, which may be miss-identified as a neutrino event. Events which have detector activity within 30 μsec before them are removed. The dead time factor caused by this selection is less than 1/1000 because the total trigger rate (expect SLE trigger) is typically $\sim$ 10Hz.

4 Total photo-electron cut
The event whose maximum number of p.e.s within 300 nsec timewindow (PE_{300}) is less than 200 is rejected. Low energy background events caused by radon and gamma ray coming from the surrounding rock are eliminated by this criteria. This threshold corresponds to $\sim$ 20 MeV/c for electrons and $\sim$ 190 MeV/c for muons.

5 Flashing PMT cut
There are some “flashing PMTs” in Super-Kamiokande, which are caused by sparks inside PMTs. They sometime make hit pattern like Čerenkov light. To reject such fake events, following three cuts are applied:

(a) Max photo-electron cut

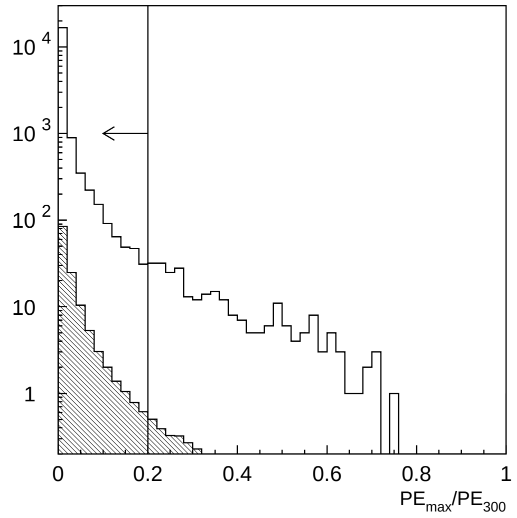

Figure 6.10: Distribution of the PE_{max}/PE_{300} ratio; open histogram for the raw data, the hatched one for neutrino beam Monte Carlo events. Monte Carlo events are normalized by its expected number of event by equivalent P.O.T.

(b) Timing distribution cut

(c) Goodness of the fit

If a spark occurs in a PMT, this PMT can produce large charge signal. To eliminate such events, $PE_{max}/PE_{300} \leq 0.2$ are required, where PE_{max} is the maximum number of p.e.s among the PMTs. Figure 6.10 shows the PE_{max}/PE_{300} distribution.

Since most of the "flashing PMT" events have broad timing distribution compared to neutrino events, "flashing PMT" events are rejected using the width of the timing distribution. If N_{min}, the minimum number of hits within 100 nsec sliding timewindow in the range of 300 nsec to 800 nsec after the event trigger, is greater than 10(15) and the number of ID hits is less(greater) than 800, the event is rejected.

For an event whose number of ID hit PMT is less than 500, a vertex fitter is used to select "flashing PMT" events. This fitter searches for the vertex point with an assumption that all photons were produced at a point. The event is rejected if the goodness of the vertex fitting (G_{low}) is less than 0.4. Figure 6.11 indicates that $G_{low} < 0.4$ cut is safe enough for the neutrino event.

6 Outer detector cut
The outer detector (OD) cut is applied to reject background of cosmic ray thru-going muons and stopping muons. An event which have more than 9 hits in the largest hit cluster in the OD is eliminated as shown in Figure 6.12. Also an event which has more than 50 hits within 800 nsec time window in the outer detector is removed.

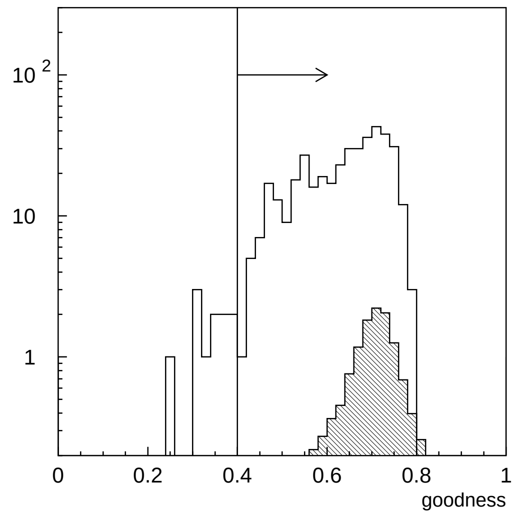

Figure 6.11: Distribution of the goodness of the vertex fitter for events such as less than 500 ID hits; open histogram for the raw data, the hatched one for neutrino beam Monte Carlo events, normalized by its expected number of event by equivalent P.O.T.

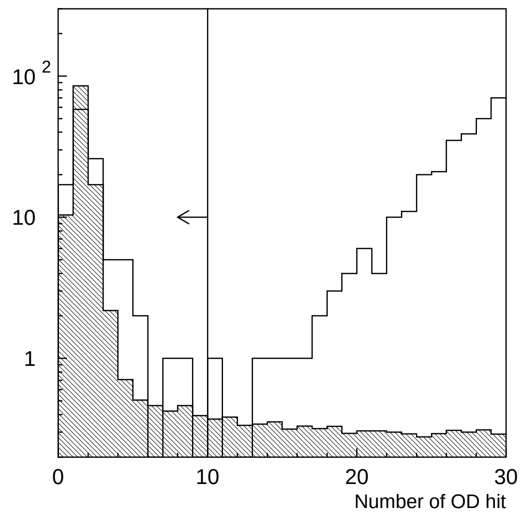

Figure 6.12: Distribution of the number of OD hit in the largest hit cluster; open histogram for the raw data, the hatched one for neutrino beam Monte Carlo events. Monte Carlo events are normalized by its expected number of event by equivalent P.O.T.

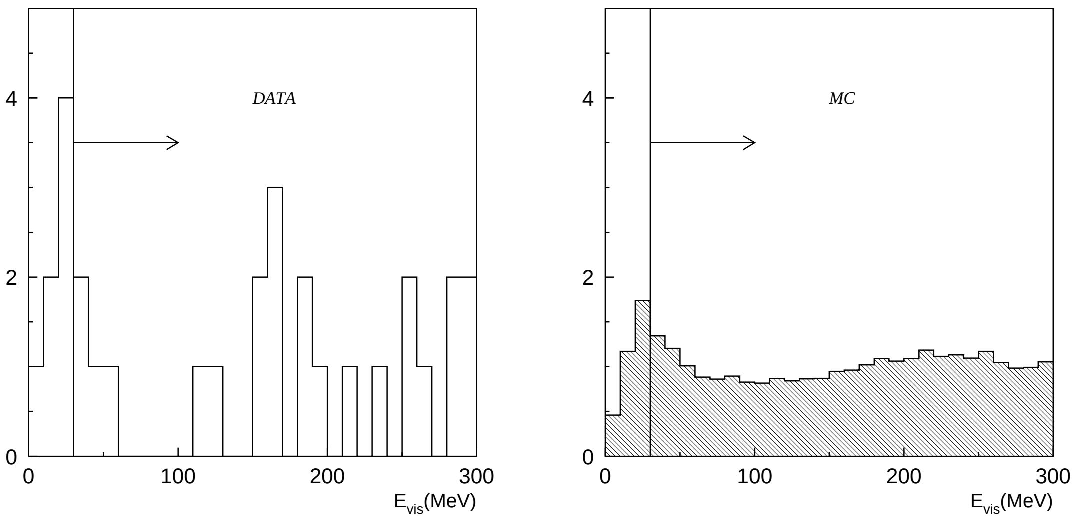

Figure 6.13: Distribution of the visible energy (E_{vis}) after OD cut for data (left) and Monte Carlo (right).

7 Fitting goodness cut
Vertex fitter is applied to define the vertex point of the interaction. Small fraction of badly fitted events are removed when the goodness of the fit was less than zero.

8 Visible energy cut
In order to avoid threshold uncertainty of the total p.e.s cut, more well-defined energy cut is applied. Visible energy (E_{vis}) greater than 30 MeV is required. The visible energy is defined as energy sum of each ring assuming the charge of each ring is produced by an electron. This threshold correspond to 197 MeV/c of muon momentum.

9 Scanning
Just to make sure all selected events were scanned visually. They were found to be consistent as neutrino induced events.

10 Fine timing cut
Tighter timing cut is applied using UTC timestamps from the GPS system. Events inside the time window of -0.2μsec $\leq \Delta T \leq 1.3\mu$sec are selected, since the measured uncertainty of two UTC timestamps are $\leq 0.2\mu$sec (Chapter 5). Figure 6.14 shows the time difference distribution. Events are clearly identified in the expected time window from 0.0μsec to 1.1μsec matching with the width of the beam spill. Systematic error from the timing information is negligible.

11 Fiducial volume cut
The event is required to have its reconstructed vertex point in the fiducial volume. The fiducial volume is defined as $D_{wall} \geq 200cm$, where D_{wall} is the distance between the

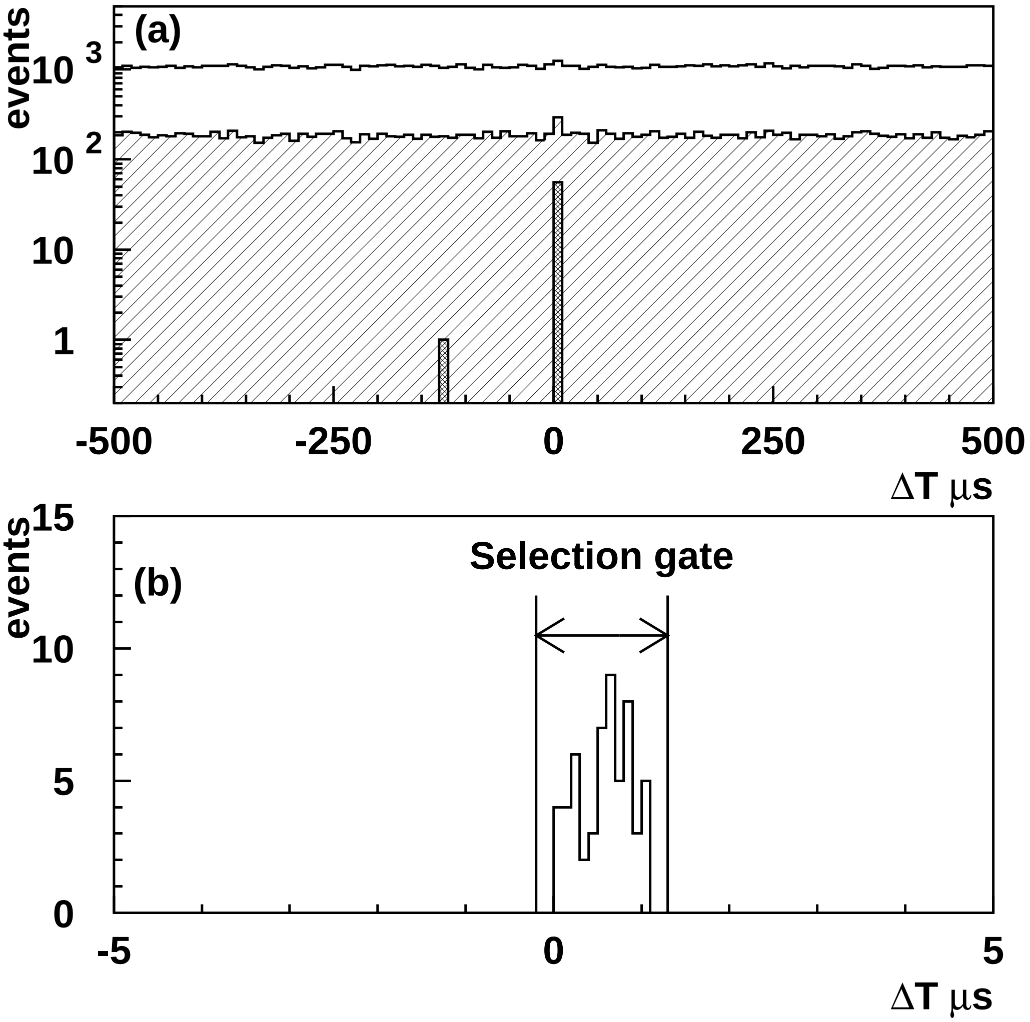

Figure 6.14: Distribution of the time difference of the two UTC timestamps; top figure for ±500μsec time window after decay electron cut(solid line), after flashing PMT cut(hatched) and selected events in the fiducial volume(dark hatched), bottom for selected events in the fiducial volume. A clear cluster of events can bee seen just within 1.1μsec of beam spill width.

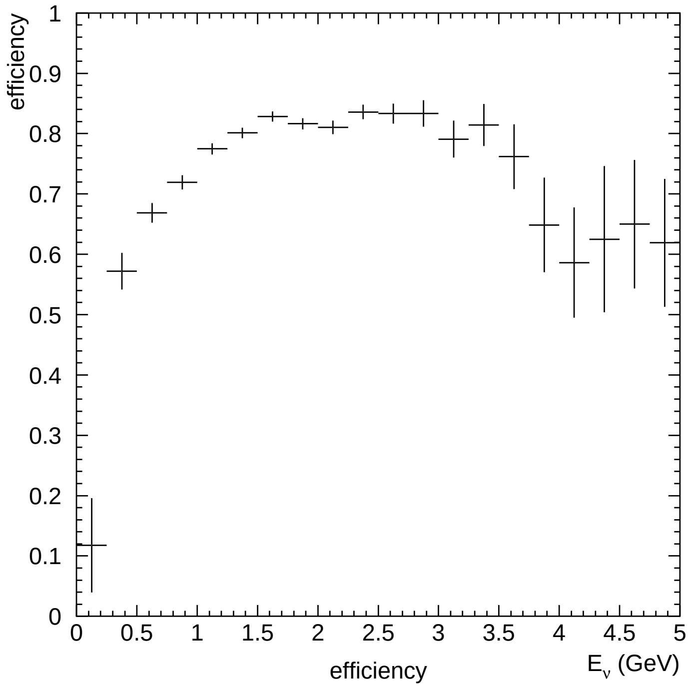

Figure 6.15: Selection efficiency at Super-Kamiokande, as a function of neutrino energy, estimated by Monte Carlo simulation.

vertex point and the nearest inner detector wall. This fiducial volume corresponds to 22.5 kt of water.

The selection efficiency for ν_μ is estimated by neutrino beam Monte Carlo simulation. Figure 6.15 shows the selection efficiency as a function of neutrino energy. The efficiency for all the interactions is 77.9% for June 1999 beam configuration and 78.4% for the beam configuration since November 1999. The efficiency for CC interactions is more than 90%.

6.3.2 Number of Observed Events

A total of 56 FC events were observed during the whole running period from June 1999 to July 2001 according to the above criteria. Those events are clearly isolated in the expected timing of the beam spill, from 0.0μsec to 1.1μsec as shown in Figure 6.14. The event classification of FC observed events is summarized in Table 6.4. All 56 FC events are listed in Table 6.5-6.7.

It is possible to reconstruct the neutrino energy for the out-going muons from the charged current quasi-elastic interaction ($\nu_\mu n \rightarrow \mu p$) with an assumption that the target neutron is at rest. The neutrino energy E_ν^{rec} is obtained as following:

$$E_\nu^{rec} = \frac{m_N E_\mu - m_\mu/2}{m_N - E_\mu + p_\mu \cos\theta_\mu}, \tag{6.4}$$

where m_N, m_μ are nucleon and muon mass, E_μ, p_μ, θ_μ are the measured muon energy, momentum and angle with respect to the neutrino beam direction. Because the momentum of

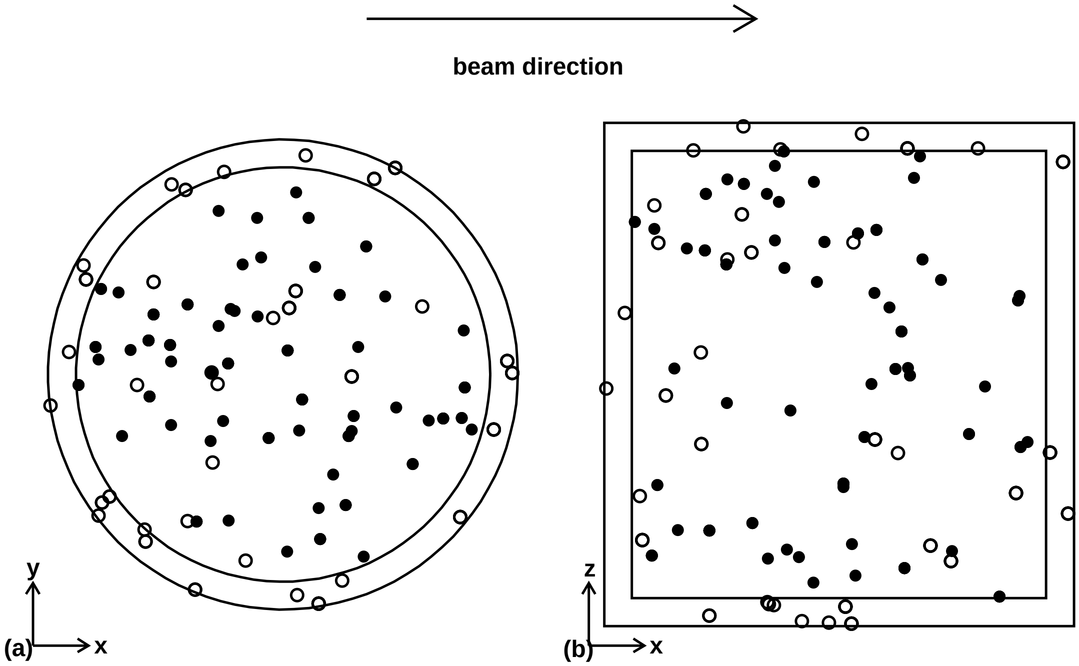

Figure 6.16: Reconstructed vertex distribution in Super-Kamiokande; left figure shows the top view and the right shows the side view with respect to the beam direction. Outer circle and box represent the inner detector, and the inner circle and box represent the boundary of the fiducial volume. Each circle point shows the reconstructed vertex; closed circle corresponds to the events whose vertices are in the fiducial volume, open circle corresponds to the events whose vertices are out of the fiducial volume.

the recoiled proton is typically below the Čerenkov threshold, only the muon is visible in these reactions. Single-ring μ-like events are selected to enhance the fraction of the charged current quasi-elastic interactions. Figure 6.17 shows the reconstructed muon momentum distribution and angle distribution with respect to the beam direction for single-ring μ-like events. Their expectations without neutrino oscillation are overlaid. Figure 6.18 shows the reconstructed neutrino energy assuming the charged current quasi-elastic scattering for those events.

An expected background source is atmospheric neutrino interactions. Its typical FC event rate in Super-Kamiokande is about 8 events per day. Considering the 1.5 μsec timewindow, estimation of the accidental contamination of the atmospheric neutrino interaction is order of 10^{-3} events through the entire running period.

6.3.3 Systematic Error

Systematic errors on the selection efficiency at Super-Kamiokande are summarized in Table 6.8. Each item is explained below.

Event category	Number of events
1-ring μ-like	30
1-ring e-like	2
multi-ring	24
total	56

Table 6.4: Event summary of observed events in Super-Kamiokande

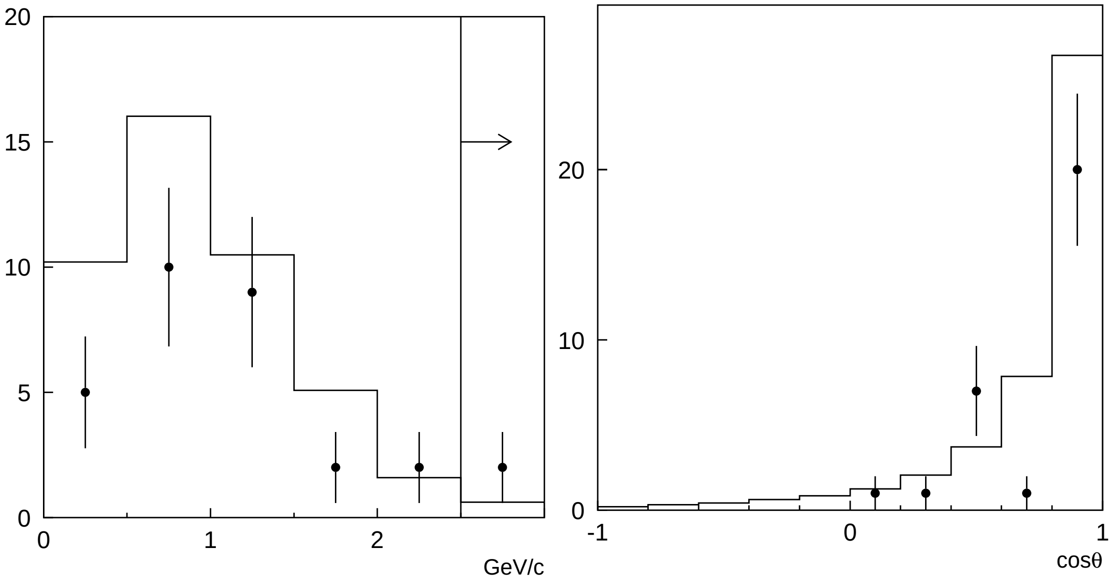

Figure 6.17: Reconstructed momentum distribution (left) and angle distribution with respect to the beam direction (right) for single-ring μ-like events in Super-Kamiokande. The momentum distribution is integrated above 2.5 GeV/c. In each figure, histogram shows the expected distribution without oscillation.

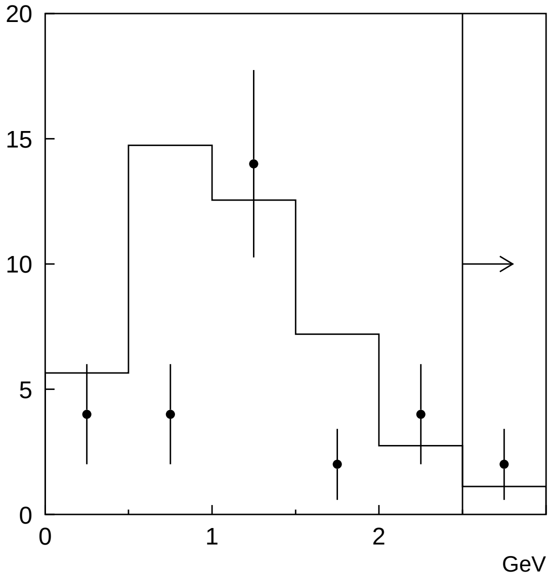

Figure 6.18: Reconstructed neutrino energy distribution for 1-ring μ-like events in Super-Kamiokande. The distribution is integrated above 2.5 GeV. The charged current quasi-elastic scattering is assumed in the reconstruction. Histogram shows the expected distribution without oscillation.

	date	$\Delta T(\mu\text{sec})$	$D_{wall}(cm)$	E_{vis} (MeV)	N_{ring}	PID	P (MeV/c)	$\cos\theta_{beam}$
1	1999-Jun-19	0.541	239.5	42.6	1	μ	216.5	0.401
2	1999-Nov-05	0.910	397.0	282.2	1	μ	466.9	0.185
3	1999-Nov-06	0.507	569.8	596.6	1	e	596.6	0.960
4	2000-Jan-24	0.806	425.1	982.1	1	μ	1086.2	0.906
5	2000-Jan-25	0.568	695.6	1015.8	1	μ	1084.7	0.927
6	2000-Feb-05	0.802	366.6	854.3	2	μ	731.8	0.887
						e	249.3	-0.534
7	2000-Feb-10	1.057	796.7	311.0	3	e	154.7	-0.143
						e	75.0	0.000
						μ	202.2	-0.417
8	2000-Feb-10	0.291	589.6	295.0	2	e	202.7	0.495
						e	84.6	0.910
9	2000-Feb-19	0.267	511.5	1213.2	1	μ	1297.0	0.911
10	2000-Feb-20	0.697	308.9	588.4	1	μ	742.2	0.539
11	2000-Feb-24	0.469	405.7	332.4	1	μ	512.8	0.869
12	2000-Mar-03	0.665	244.4	655.2	2	μ	571.1	0.033
						e	233.8	0.885
13	2000-Mar-06	0.647	474.6	777.6	3	μ	532.5	0.957
						μ	335.3	0.413
						μ	459.8	0.452
14	2000-Mar-07	0.536	987.3	2983.0	3	e	1226.7	0.914
						e	951.4	0.912
						e	410.5	0.730
15	2000-Mar-10	1.026	496.3	438.2	1	μ	603.4	0.303
16	2000-Mar-12	0.516	550.3	683.5	1	μ	791.2	0.490
17	2000-Mar-15	0.766	206.2	1196.0	3	μ	841.9	0.696
						e	283.8	0.951
						e	199.0	0.659
18	2000-Mar-17	0.821	548.8	1643.7	2	μ	1357.5	0.995
						e	244.1	-0.925
19	2000-May-19	0.396	850.5	546.9	4	μ	317.7	-0.030
						e	204.9	0.481
						e	124.5	-0.343
						e	46.5	-0.442
20	2000-May-20	0.005	883.9	3051.3	1	μ	2647.8	0.973
21	2000-May-24	0.290	833.0	1986.5	1	μ	1896.8	0.966
22	2000-May-25	0.533	414.1	121.3	1	μ	310.1	0.726
23	2000-May-31	0.403	1024.0	910.2	3	e	542.6	0.988
						μ	217.8	-0.352
						e	249.3	0.950

Table 6.5: List of the observed events in Super-Kamiokande(1).

	date	$\Delta T(\mu\text{sec})$	$D_{wall}(cm)$	E_{vis} MeV	N_{ring}	PID	P (MeV/c)	$\cos\theta_{beam}$
24	2000-Jun-09	0.891	218.5	253.7	2	μ	345.3	-0.902
						e	85.9	-0.130
25	2000-Jun-11	0.650	589.6	755.6	1	μ	871.0	0.862
26	2000-Jun-16	0.624	856.1	2312.1	3	μ	1089.9	0.930
						e	879.1	0.792
						e	429.6	0.969
27	2000-Jun-20	0.124	448.6	1625.0	1	μ	1648.6	0.943
28	2000-Jun-21	0.694	694.0	1168.5	4	e	276.7	0.965
						e	258.9	0.045
						μ	541.3	0.690
						e	232.1	-0.272
29	2001-Jan-23	0.437	1049.8	3564.1	1	μ	3111.9	0.923
30	2001-Jan-25	1.013	365.0	1028.8	1	μ	1144.6	0.844
31	2001-Jan-26	0.897	568.2	215.5	1	μ	403.4	0.965
32	2001-Feb-02	0.700	425.8	998.1	1	μ	1099.4	0.859
33	2001-Feb-03	0.017	439.5	958.9	3	μ	748.6	0.893
						e	177.1	-0.303
						e	158.5	0.488
34	2001-Feb-18	0.936	556.1	283.5	2	e	177.9	0.578
						e	99.9	0.252
35	2001-Feb-25	1.019	541.4	1367.4	1	μ	1358.4	0.919
36	2001-Mar-04	0.237	276.4	781.6	1	e	781.6	0.550
37	2001-Mar-29	0.669	367.5	432.4	1	μ	596.8	0.407
38	2001-Mar-30	0.706	580.8	2602.0	1	μ	2457.4	0.996
39	2001-Mar-30	0.628	648.7	846.9	3	e	432.9	0.715
						μ	465.1	0.877
						μ	245.5	0.224
40	2001-Apr-12	0.250	353.9	857.0	1	μ	944.0	0.418
41	2001-Apr-15	0.510	417.5	588.2	5	e	172.0	0.122
						μ	244.4	0.271
						e	126.6	-0.963
						e	34.7	-0.423
						e	104.1	0.760
42	2001-Apr-18	0.053	1114.2	1032.9	1	μ	1118.0	0.807
43	2001-Apr-20	0.005	357.7	1009.4	1	μ	1106.2	0.960
44	2001-Apr-21	0.894	327.2	375.1	3	e	154.8	0.955
						e	156.1	-0.989
						e	44.2	0.521

Table 6.6: List of the observed events in Super-Kamiokande(2).

	date	$\Delta T(\mu\text{sec})$	$D_{wall}(cm)$	E_{vis} (MeV)	N_{ring}	PID	P (MeV/c)	$\cos\theta_{beam}$
45	2001-May-18	0.880	764.8	355.2	1	μ	531.7	0.585
46	2001-May-27	0.883	881.5	119.2	1	μ	307.3	0.995
47	2001-May-30	0.159	805.6	970.4	1	μ	1067.2	0.850
48	2001-May-31	0.758	461.1	929.1	3	e	496.2	0.874
						μ	413.4	-0.186
						e	150.0	0.443
49	2001-May-31	1.024	210.5	348.2	3	μ	422.6	0.775
						μ	243.8	-0.686
						μ	133.4	0.286
50	2001-Jun-06	0.630	380.3	648.2	3	μ	411.7	0.580
						e	246.0	0.053
						e	162.8	-0.080
51	2001-Jun-10	0.118	313.7	878.0	1	μ	995.6	0.970
52	2001-Jun-13	0.982	1101.2	1928.2	2	μ	1592.4	0.849
						μ	465.8	0.715
53	2001-Jun-18	0.222	512.5	1387.4	3	e	731.4	0.817
						e	371.1	0.411
						e	260.2	0.590
54	2001-Jun-26	0.127	662.9	427.0	4	μ	130.5	0.969
						μ	276.3	-0.840
						e	102.3	-0.483
						e	175.3	0.300
55	2001-Jun-30	0.721	486.7	597.5	1	μ	711.0	0.501
56	2001-Jul-03	0.376	377.8	2145.9	1	μ	2044.6	0.968

Table 6.7: List of the observed events in Super-Kamiokande(3).

Event selection	±0.9%
Fiducial volume	±1.8%
MC statistic	±0.9%
Total	±2.3%

Table 6.8: Systematic errors on the Super-Kamiokande analysis.

- **Event selection**
  The systematic error for the event selection, except for the fiducial volume cut, is estimated by changing following three thresholds. A ±10% change on the PE_{300} cut causes $^{+0.8}_{-0.7}\%$ change on the MC sample. A ±3 hits change on the OD cut causes $^{-0.15}_{+0.04}\%$ change on the MC sample. A ±10 MeV change on the E_{vis} cut causes ±0.3% change on the MC sample. Thus, an error of ±0.9% is assigned.

- **Fiducial volume**
  The performance of the vertex fitter was checked by comparing results of two different vertex fitters, "TDC-fit" (Section C.2) and "MS-fit" (Section C.5). The latter is used for the fiducial volume cut. The two fitters were applied to atmospheric 1-ring μ-like data sample and atmospheric neutrino Monte Carlo simulation, resulting 1.8% difference in DATA/MC ratio.

- **MC statistics**
  The statistical error of neutrino beam Monte Carlo event sample is assigned as an error of ±0.9%.

In total, a systematic error of ±2.3% is assigned to the selection efficiency.

The systematic errors coming from the uncertainty of the cross section and neutrino beam spectrum have correlation with the 1kt detector. Treatment of these errors are discussed in Section 6.5.3.

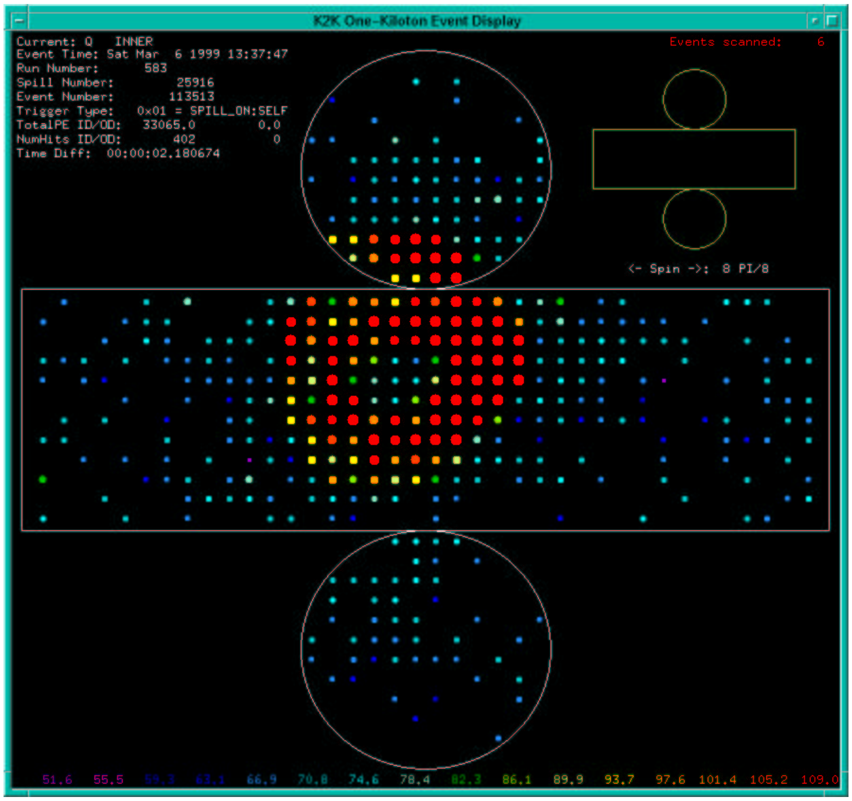

```
Current: Q   INNER
Event Time: Sat Mar  6 1999 13:37:47
Run Number:       583
Spill Number:         25916
Event Number:        113513
Trigger Type:   0x01 = SPILL_ON:SELF
TotalPE ID/OD:   33065.0         0.0
NumHits ID/OD:       402           0
Time Diff:  00:00:02.180674
```

Figure 6.19: A typical neutrino event in the 1kt detector.

6.4 Measurement of the Neutrino Interaction at the 1kt Detector

The number of observed events in the 1kt detector is extrapolated into the expected number of events in Super-Kamiokande using Formula 6.1. The event selection and result of the 1kt detector are described in this section.

6.4.1 Event Selection at the 1kt Detector

Figure 6.19 shows a typical neutrino event in the 1kt detector. The selection criteria at 1kt are described bellow for each step, and the typical number of selected events in each step in January 2000 is summarized in Table 6.9.

1 **Good beam spill selection**
The "good beam spills" are used, as described in Subsection 6.2.1.

2 **Pre-activity cut**
An event which has activity within 1.2 μsec before the beam timing is rejected. The source of pre-activities is mainly cosmic ray muons, which could cause fake on-spill event by reflection signal of cables. The fraction of the spills with the pre-activity event is about

	Selection	DATA	MC
1	Analyzed number of spill	611587	
	(MC) generated in Fiducial-C		98482
2	Pre-activity cut	598844	
3	Total photo-electron cut	136372	
4	Single event selection (N^1_{peak})	110867	
5	Vertex in Fiducial-C	5746	73820

Table 6.9: Summary of the number of selected events in each step, in January 2001 run. Definitions of the fiducial volumes are shown in Figure 6.23

1.9% (3% in 1999 run, before the buffer-amplifiers were installed). Those spills are not counted in the accumulated number of spills and P.O.T.

3 Total photo-electron cut

A event is required to have more than about 1000 p.e.s of PMTSUM (analog sum of all inner PMTs) in Flash-ADC (FADC). This threshold is equivalent to visible energy deposit of about 100 MeV. Figure 6.20 shows the efficiency curve of the FADC. The threshold is high enough compared to the signals from muon-decay electrons. In November 1999 run, one fourth of the cables which bring PMTSUM to FADC was disconnected by mistake. The selection efficiency was decreased by 1%, and the efficiency curve was distorted. This effect is taken into account in the detector simulation for this period.

4 Single event selection

Since the event rate of neutrino-induced activity in the 1kt detector is about 0.39 events per spill, more than two neutrino events may occur in the same spill. Events with single neutrino interaction are used for the analysis because the readout electronics(ATM) cannot correctly distinguish multiple events in one beam spill due to its 300 nsec ADC gate width and subsequent 300 nsec dead time.

The number of events in a spill is measured by counting the number of peaks in PMTSUM pulse hight distribution recorded by FADC as a function of time, within 1.1 μsec of the on-spill time window. When successive interactions occur in a spill, corresponding peaks can be seen in the FADC, while ATM cannot record those events properly (Figure 6.21). Figure 6.22 shows the number of peaks recorded by FADC in a beam spill and the FADC peak time distribution after the single event selection. The latter has a clear 9-bunch structure in a spill and thus guarantee that the peaks in FADC is originated from the proton beam which has the 9-bunch micro structure.

The effect of multiple-events is taken into account for the number of expected events in Super-Kamiokande. The correction factor of multiple-events C_{multi} is defined as following:

$$C_{multi} \equiv \left(\frac{N^{total}_{peak}}{N^{1}_{peak}} \right)_{DATA} \cdot \left(\frac{N^{total}_{int}}{N^{total}_{peak}} \right)_{MC} \tag{6.5}$$

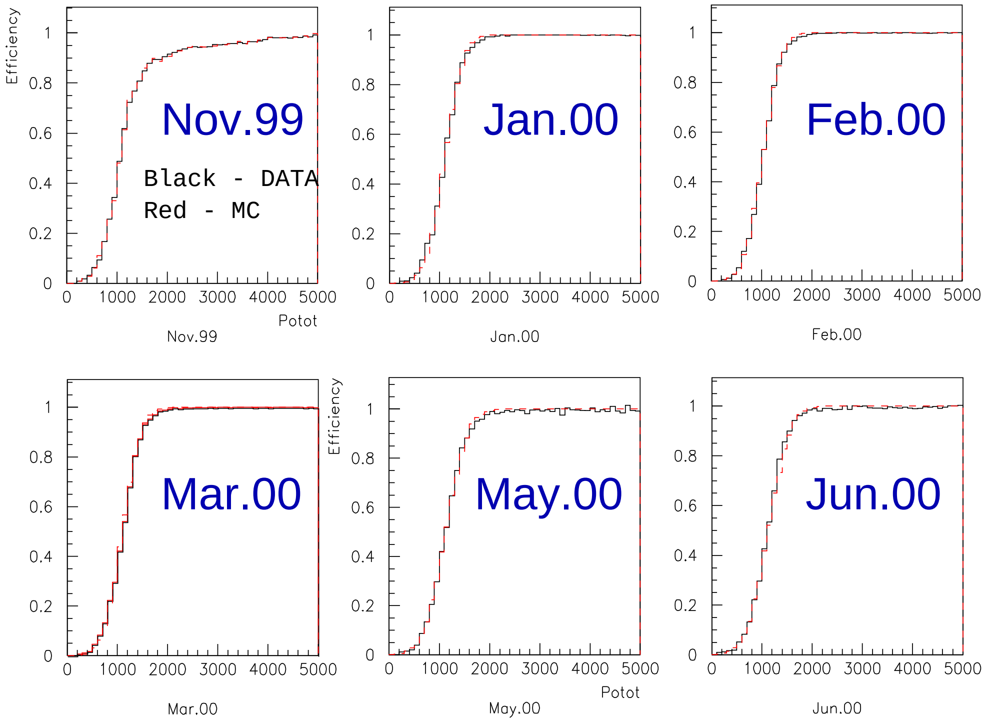

Figure 6.20: FADC efficiency curve around the threshold of total p.e. cut. The efficiency estimated from data (black line) and from MC (red line) are overlaid. The distortion of the efficiency curve in November 1999 is caused by the disconnection of 1/4 of PMTSUM cables.

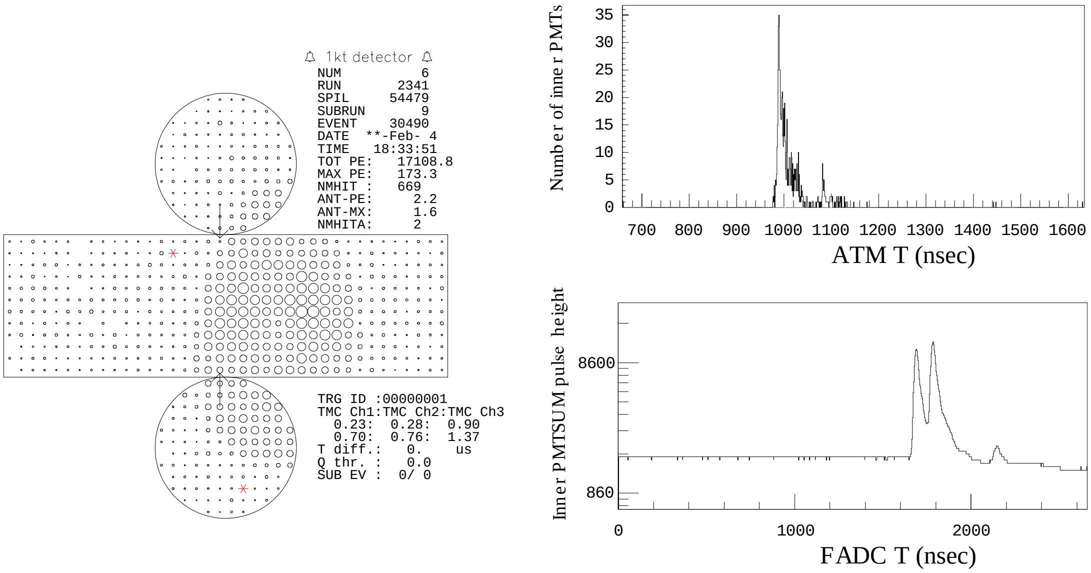

```
NUM          6
RUN       2341
SPIL     54479
SUBRUN       9
EVENT    30490
DATE  **-Feb- 4
TIME   18:33:51
TOT PE:   17108.8
MAX PE:   173.3
NMHIT :   669
ANT-PE:     2.2
ANT-MX:     1.6
NMHITA:     2
```

```
TRG ID :00000001
TMC Ch1:TMC Ch2:TMC Ch3
  0.23:  0.28:  0.90
  0.70:  0.76:  1.37
T diff.:   0.    us
Q thr. :   0.0
SUB EV :  0/ 0
```

(a) (b)

Figure 6.21: Event display for the multiple event in a beam spill (left), the TDC distribution of inner-detector PMT recorded by ATM (top-right), the PMTSUM distribution recorded by FADC (lower-right). Only FADC can clearly identify the event to contain multiple events in a beam spill.

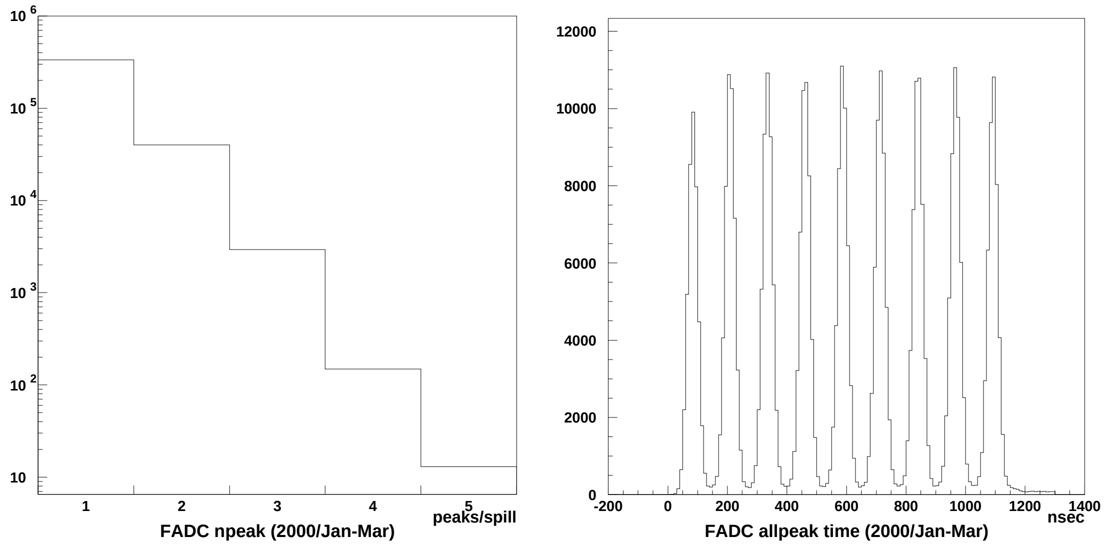

(a) (b)

Figure 6.22: Number of peak recorded by FADC (left) and the time distribution of the peak time after the single event selection (right).

where N_{peak}^{total} is the number of total peaks in FADC in each spill, N_{peak}^{1} is the number of events that have only one peak, N_{int}^{total} is the number of total neutrino interaction in each spill. The ratio $\left(N_{int}^{total}/N_{peak}^{total}\right)_{MC}$ is estimated to be 1.008 by Monte Carlo simulation.

5 **Fiducial volume cut**

In order to distinguish neutrino interaction from incoming background events, following three fiducial volumes are defined inside of the 1kt detector as shown in Figure 6.23.

(a) Fiducial-A, for neutrino profile measurement. Perpendicular cylinder with 3 m radius, and 6 m height. Total volume is 170 t.

(b) Fiducial-B, for the event rate stability. Horizontal cylinder along the neutrino beam with 2 m radius, and 4 m length. Total volume is 50 t.

(c) Fiducial-C, for the measurement of the number of neutrino event N_{obs}^{1kt}. Horizontal cylinder with 2 m radius, and 2 m length, upstream half of the Fiducial-B. Total volume is 25 t.

The selection efficiency for ν_μ is estimated by the Monte Carlo simulation. Figure 6.24 shows the selection efficiency for Fiducial-C as a function of vertex position and neutrino energy. The efficiency for all the interaction is about 71% for 1999 run and 75% for 2000 and 2001 run.

A total of 80024 events was observed during the whole running period from June 1999 to July 2001. Table 6.10 summarizes the numbers of events for different categories of all the period.

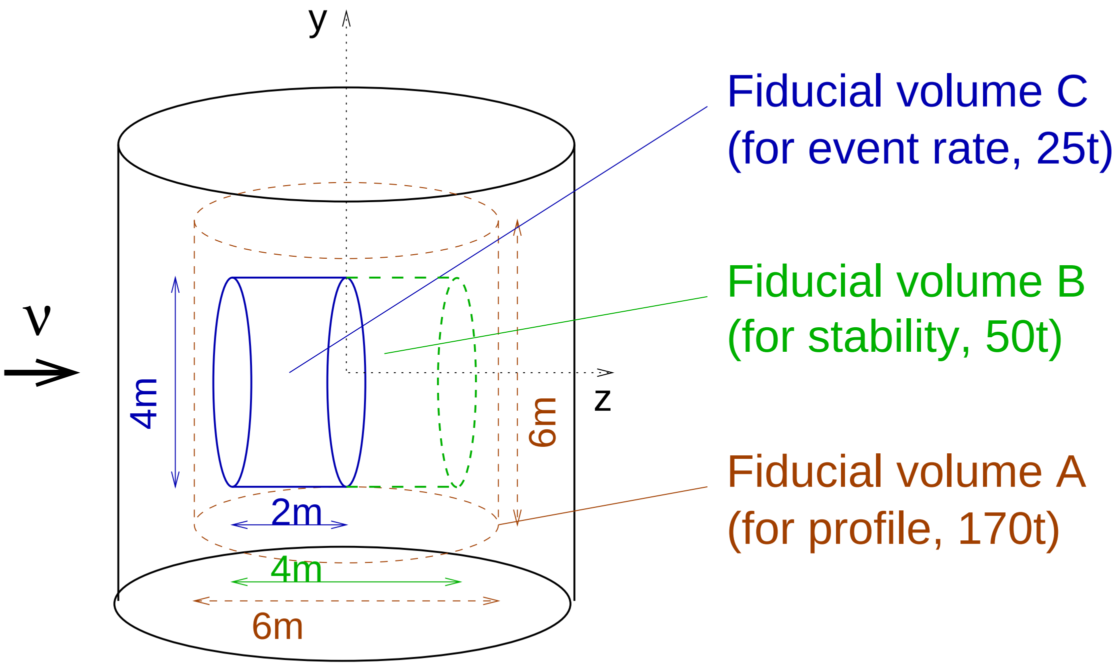

Figure 6.23: Definition of the fiducial volume in the 1kt detector.

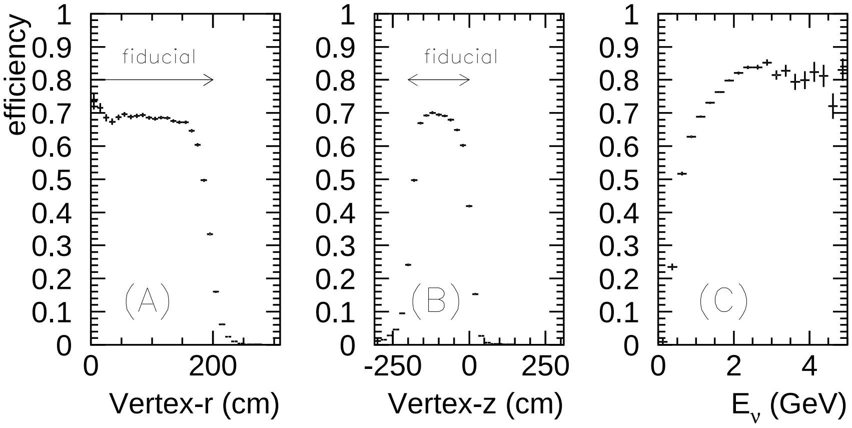

Figure 6.24: Selection efficiency for events in Fiducial-C, as a function of its vertex position (A:radius from the Z-axis, B:Z-position) and neutrino energy (C).

period	Jun.99	Nov.99	Jan.00	Feb.00	Mar.00	May.00	Jun.00
Target diameter	$20mm\phi$	$30mm\phi$					
Horn current	200kA	250kA					
P.O.T.$_{1kt}$($\times 10^{18}$)	2.60	2.62	1.81	3.74	3.35	2.42	3.17
total peaks in FADC (N_{peak}^{total})	109119	118321	85155	174224	155643	88445	114688
single event (N_{peak}^{1})	89782	96304	67678	139241	122700	74227	95888
efficiency ($\epsilon_{\nu_\mu}^{1kt}$)	0.706	0.708	0.743	0.748	0.743	0.742	0.742
Background ($R_{b.g.}$)	0.031	0.031	0.015	0.015	0.015	0.015	0.015
7-bunch correction ($C_{7b\rightarrow 9b}$)	-	-	-	-	-	1.282	1.283
observed events (N_{obs}^{1kt})	4282	4923	3576	7139	6234	3705	4933
number of interaction (N_{int}^{1kt})	7206	8351	6013	11857	10567	7573	10130
event rate(/10^{15}P.O.T.)	2.77	3.19	3.32	3.17	3.16	3.13	3.20

period	Jan.01	Feb.01	Mar.01	Apr.01	May.01	Jun.01	Jul.01
Target diameter	$30mm\phi$						
Horn current	250kA						
P.O.T.$_{1kt}$($\times 10^{18}$)	2.92	4.75	4.27	2.47	1.60	5.79	1.43
total peaks in FADC (N_{peak}^{total})	136372	229826	207066	120324	75864	27597	67719
single event (N_{peak}^{1})	110867	182166	163502	95032	60113	220087	53606
efficiency ($\epsilon_{\nu_\mu}^{1kt}$)	0.745	0.745	0.745	0.745	0.745	0.745	0.745
Background ($R_{b.g.}$)	0.015	0.015	0.015	0.015	0.015	0.015	0.015
7-bunch correction ($C_{7b\rightarrow 9b}$)	-	-	-	-	-	-	-
observed events (N_{obs}^{1kt})	5746	9213	8228	4743	3113	11430	2759
number of interaction (N_{int}^{1kt})	9420	15491	13888	8004	5236	19102	4645
event rate(/10^{15}P.O.T.)	3.23	3.26	3.26	3.24	3.27	3.30	3.26

$$
\begin{aligned}
Total: \quad N_{obs}^{1kt} &= 80024 \\
N_{int}^{1kt} &= 137483 \pm 486(stat.)
\end{aligned}
$$

Table 6.10: Summary of the 1kt detector for all the period.

6.4.2 Number of Neutrino Interactions in the 1kt Detector

In order to obtain the number of neutrino interactions in the 1kt detector, following correction are applied to the number of observed events in 1kt:

$$N_{int}^{1kt} = \frac{N_{obs}^{1kt}}{\epsilon_{\nu_\mu}^{1kt}} \cdot \frac{C_{7b\to 9b} \cdot C_{multi}}{1 + R_{b.g.}} \tag{6.6}$$

where,

N_{obs}^{1kt} : Number of observed events in the 1kt detector,

$\epsilon_{\nu_\mu}^{1kt}$: Event selection efficiency at the 1kt detector,

$R_{b.g.}$: Background contamination rate at the 1kt detector,

$C_{7b\to 9b}$: Correction factor for 7-bunch analysis, only in May 2000 and June 2000 run,

C_{multi} : Correction factor for multiple-events described in Section 6.4.1.

The expected backgrounds are cosmic ray muons and neutrino induced incoming muons. The background contaminations are estimated as follows.

1 **Cosmic ray muons.**
The rate of cosmic ray muon contamination is estimated by random-triggered data. The data was analyzed with the same selection. The contamination was estimated to be 1.0% of neutrino candidates in Fiducial-C for 2000 and 2001 run. Before the installation of the buffer amplifier in June 1999 and November 1999 run, the reflection pulse in the signal cable caused fake events. In this period, the contamination was estimated to be 2.6%.

2 **Neutrino induced muons.**
The on-spill triggered data contains neutrino beam induced incoming muons, which are generated by neutrino interaction in surrounding materials. Most of the neutrino induced muons are injected from the upstream of the tank and penetrate the front side of the outer detector. Some of the selected neutrino candidates in Fiducial-C, with outer detector hit, were visually inspected by physicists. The contamination was estimated to be 0.5% of neutrino candidates in Fiducial-C.

Total background contamination rate $R_{b.g.}$ are estimated to be 1.5%(3.1%) of neutrino candidates for 2000-2001 run (1999 run). The number of neutrino interactions are corrected with $R_{b.g.}$.

The 7-bunch analysis correction ($C_{7b\to 9b}$) was required in May 2000 and June 2000 run because the 8th and 9th bunch were sometimes lost due to the drift of the stop-timing signal to the FADC (Figure 6.25). Neutrino events in the first to 7th bunches in a spill were used for the analysis to avoid this gate uncertainty. This effect was corrected by the ratio of the number of events in the 1-7th bunch to that in the 1-9th bunch, using the data in which the stop signal was not drifted in this period. The correction factor $C_{7b\to 9b}$ was stable during the running period as shown in Figure 6.26.

Using Equation 6.6, the number of neutrino interaction is estimated to be $N_{int}^{1kt} = 137483 \pm 486(stat.)$. Figure 6.27 shows the long-term stability of the event rate and it is very stable as expected.

Figure 6.28 shows the reconstructed muon momentum distribution and angle distribution with respect to the beam direction for fully-contained single-ring μ-like events observed in Fiducial-C.

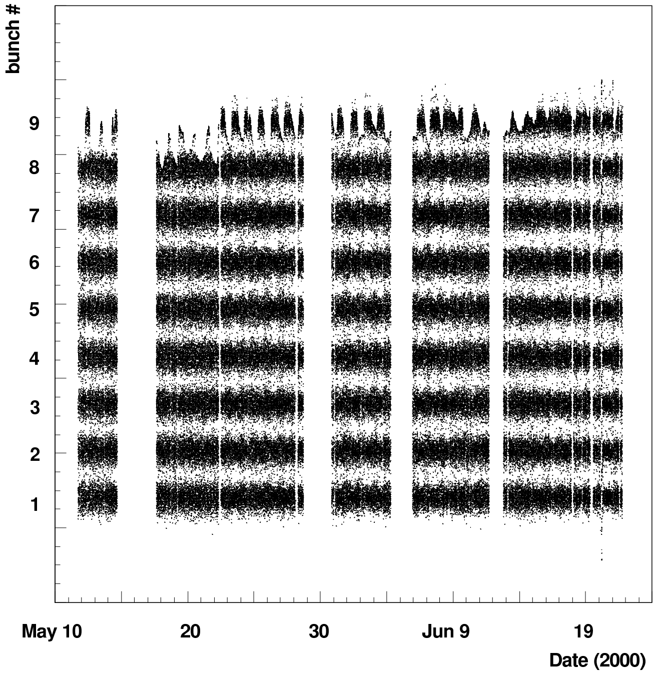

Figure 6.25: Timing distribution of the event in each spill from May 2000 to June 2000 run. The 8th and 9th bunch were sometimes lost due to the drift of the stop-timing signal to the FADC.

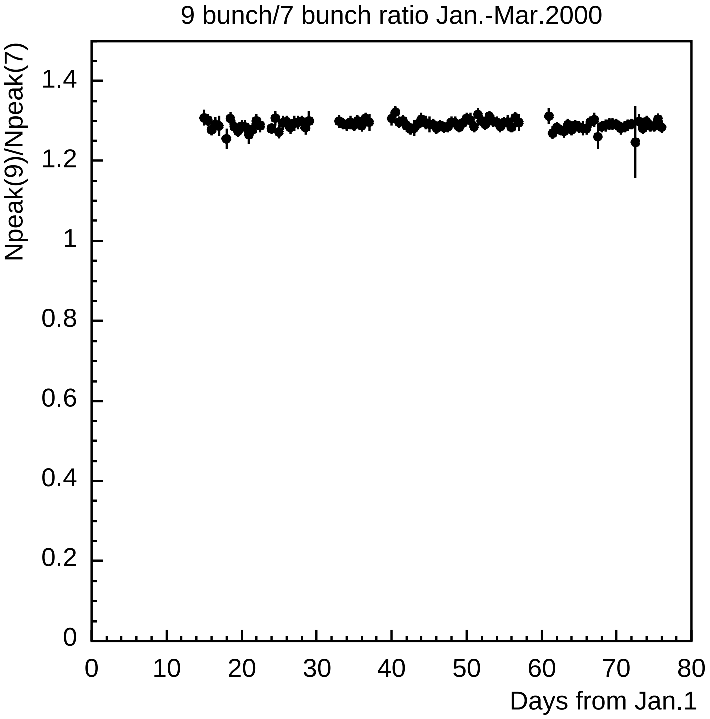

Figure 6.26: Stability of the correction factor for 7-bunch analysis.

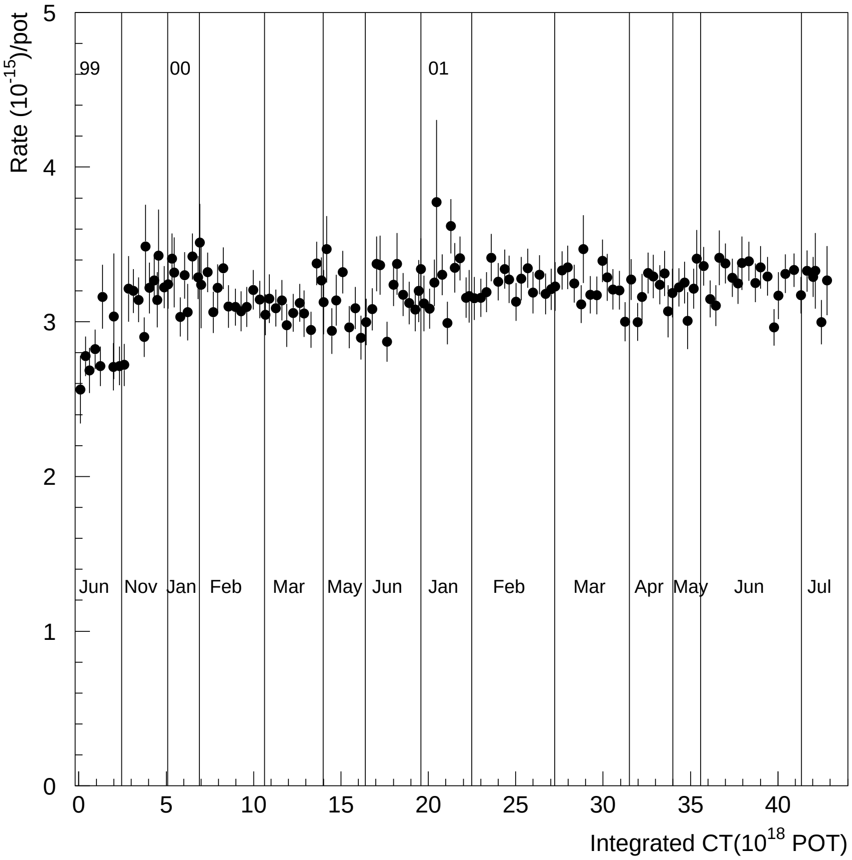

Figure 6.27: Long term stability of the neutrino event rate at 1kt. In June 1999, neutrino beam intensity was lower than the other period due to the lower current in the horn magnet. In November 1999, the event rate looks slightly lower due to the disconnection of 1/4 of PMTSUM cables.

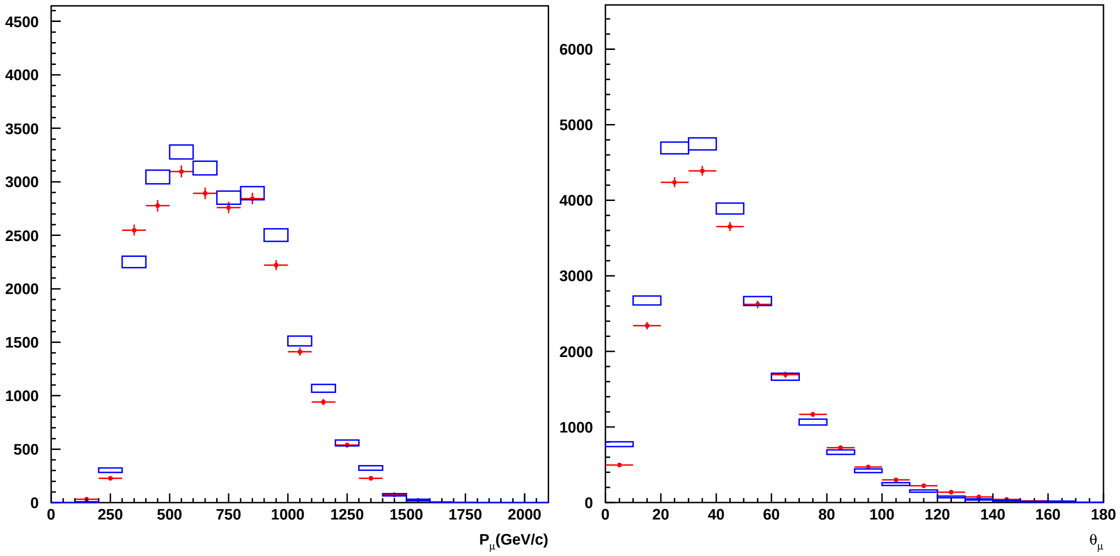

Figure 6.28: Reconstructed momentum distribution (left) and angle distribution with respect to the beam direction (right) for single-ring μ-like events in the 1kt detector. Boxes are the expected distribution. The size of the box shows statistical error of Monte Carlo events in each bin. In each figure, Monte Carlo events are normalized by the number of total events in Fiducial-C.

<table>
<tr><th>period</th><th>Jun.99</th><th>Nov.99</th><th>Jan.00</th><th>Feb.00</th><th>Mar.00</th><th>May.00</th><th>Jun.00</th></tr>
<tr><td>Fiducial volume</td><td colspan="7">4.0%</td></tr>
<tr><td>FADC threshold</td><td colspan="7">1.0%</td></tr>
<tr><td>1/4 disconnection to FADC</td><td>0.0%</td><td>1.0%</td><td colspan="5">0.0%</td></tr>
<tr><td>Energy scale</td><td colspan="7">1.0%</td></tr>
<tr><td>Background rate</td><td colspan="2">1.0%</td><td colspan="5">0.5%</td></tr>
<tr><td>Multiple-events treatment</td><td colspan="7">0.7%</td></tr>
<tr><td>7-bunch/9-bunch</td><td colspan="5">0.0%</td><td colspan="2">1.2%</td></tr>
<tr><td>Total</td><td>4.4%</td><td>4.5%</td><td>4.3%</td><td>4.3%</td><td>4.3%</td><td>4.5%</td><td>4.5%</td></tr>
</table>

<table>
<tr><th>period</th><th>Jan.01</th><th>Feb.01</th><th>Mar.01</th><th>Apr.01</th><th>May.01</th><th>Jun.01</th><th>Jul.01</th></tr>
<tr><td>Fiducial volume</td><td colspan="7">4.0%</td></tr>
<tr><td>FADC threshold</td><td colspan="7">1.0%</td></tr>
<tr><td>1/4 disconnection to FADC</td><td colspan="7">0.0%</td></tr>
<tr><td>Energy scale</td><td colspan="7">1.0%</td></tr>
<tr><td>Background rate</td><td colspan="7">0.5%</td></tr>
<tr><td>Multiple-events treatment</td><td colspan="7">0.7%</td></tr>
<tr><td>7-bunch/9-bunch</td><td colspan="7">0.0%</td></tr>
<tr><td>Total</td><td>4.3%</td><td>4.3%</td><td>4.3%</td><td>4.3%</td><td>4.3%</td><td>4.3%</td><td>4.3%</td></tr>
</table>

Table 6.11: Systematic errors on the N_{int}^{1kt}.

6.4.3 Systematic Errors on the number of neutrino interactions in the 1kt detector

Systematic errors on N_{int}^{1kt} are summarized in Table 6.11. Each item is explained below.

- **Fiducial volume**

  The performance of the vertex fitter for the 1kt detector was experimentally studied using cosmic ray [32, 31]. The result proves that the resolution of the vertex reconstruction is better for transverse direction to the particle track than that for longitudinal direction. Since the particle track of a neutrino event is dominantly directed to Z-axis, Z-vertex distribution was used to estimate the error of the fiducial volume.

  The vertex profile was analyzed with the selected events in the Fiducial-A. Target mass correction was applied to the profile due to the cylindrical shape of the fiducial volume. Figure 6.29 shows the reconstructed vertex distribution of horizontal (X), vertical (Y) and longitudinal (Z) direction, overlaid with Monte Carlo predictions.

  There are systematic difference in the Z-vertex distribution outside the Fiducial-C, which comes from mis-fitting of outgoing muons.

  The systematic error from the vertex position resolution is estimated by comparing the observed event rate in several fiducial volume definitions with MC (Table 6.12).

  The ±4% spread including statistical error from the Fiducial-C is assigned as the system-

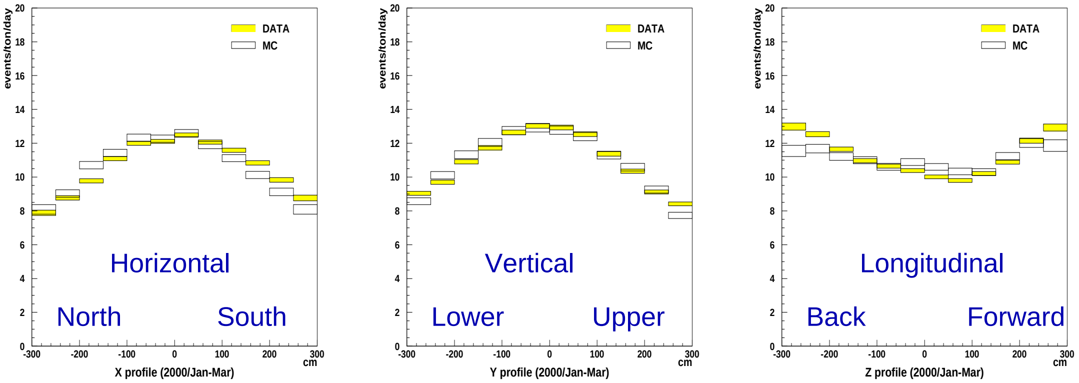

Figure 6.29: Vertex profile of horizontal, vertical, and longitudinal direction in the 1kt detector, after target mass correction.

Z-vertex	DATA	MC	relative DATA/MC
$-2 < z < 0$ m (Fiducial-C)	16571	13223	1.
$-3 < z < 0$ m	24990	19418	$1.03 \pm 0.01(stat.)$
$-2 < z < +2$ m (Fiducial-B)	31290	25720	$0.97 \pm 0.01(stat.)$
$-2 < z < +3$ m	39330	32139	$0.98 \pm 0.01(stat.)$
$-2 < z < +4.5$ m	49449	38425	$1.03 \pm 0.01(stat.)$

Table 6.12: Event rate comparison (DATA/MC) with various fiducial volume definition of Z-vertex. The Z-coordinate with its origin set at the 1kt detector center is defined along the beam axis. DATA means the observation from January 2000 to March 2000.

atic error of the fiducial volume.

- **FADC threshold error**
  The threshold of FADC is set at about 1000 p.e.s as shown in Figure 6.20. Its fluctuation is estimated to be 10% for the whole period. The 10% change on the threshold in the MC sample causes 1% change on the event rate. Thus ±1% is assigned for the systematic error in the FADC threshold.

  Due to the disconnection of one fourth of PMTSUM cables to FADC, the selection efficiency decreased by 1% in November 1999 run. An additional 1% error is assigned for this period.

- **Energy scale error**
  The absolute energy scale of the 1kt detector is calibrated within 5% accuracy, as described in Chapter 3.4.1. If the energy scale of the MC sample shifted by 5%, the event rate changes by less than 1%. The energy scale error is assigned to be 1%.

- **Background rate uncertainty**
  The estimation of the background rate is described in Section 6.4.2. The statistical error

of the background rate is assigned as a systematic error of ±1.0% in 1999 run and ±0.5% to the other period.

- **Error in multiple-events correction**
  The correction factor was estimated by Monte Carlo simulation as described in Section 6.4.1. Its statistical error is assigned as a systematic error of 0.7%.

- **Correction for 7-bunch analysis**
  7-bunch analysis is applied in May 2000 and June 2000 run, as described in Section 6.4.2. The statistical error in the calculation of the correction factor $C_{7b \to 9b}$ is 1%. For estimation of the validity of the 7-bunch analysis method, the other data from January 2000 to March 2000 is analyzed by this method. The difference between the 7-bunch analysis and the standard one is found to be at most 0.4%.

  Also, the vertex position mis-fitting caused by signals belonging to the masked bunches is considered. When FADC signals in the 8th and 9th bunches are masked, a multiple-event may mis-identified as a single event because the ADC gate width of ATM is about 300 nsec which corresponds to 3 bunches in a beam spill. In such a case, the vertex position fitter failed by approximately 0.6% of events selected by the 7-bunch analysis.

  In total, a systematic error of ±1.2% is assigned to the error caused by the 7-bunch analysis.

6.5 Number of Expected Events in Super-Kamiokande

6.5.1 Extrapolation Formula

The number of expected neutrino events in Super-Kamiokande is extrapolated from the number of observed events in the 1kt detector by following formula:

$$N_{exp}^{SK} = N_{int}^{1kt} \cdot \epsilon_{\nu_\mu}^{SK} \cdot R_{\nu_\mu}^{SK/1kt} \cdot \frac{POT_{SK}}{POT_{1kt}} \cdot \frac{C_{7b \to 9b} \cdot C_{multi} \cdot C_{\nu_e}}{1 + R_{b.g.}} \tag{6.7}$$

The ratio of the number of neutrino interaction

The ratio of the number of neutrino interaction at Super-Kamiokande and the 1kt detector ($R_{\nu_\mu}^{SK/1kt}$) is defined as follows;

$$R_{\nu_\mu}^{SK/1kt} = \frac{\int \Phi_{\nu_\mu}^{SK} \cdot \sigma_{H_2O} \cdot M_{SK} dE}{\int \Phi_{\nu_\mu}^{1kt} \cdot \sigma_{H_2O} \cdot M_{1kt} dE} \tag{6.8}$$

where $\Phi_{\nu_\mu}^{SK(1kt)}$ are the muon neutrino flux per unit P.O.T. per unit area, σ_{H_2O} is the cross section, and $M_{SK(1kt)}$ is the fiducial mass. The energy integrated ratio $R_{\nu_\mu}^{SK/1kt}$ is provided by beam Monte Carlo since it reproduces well the PIMON measurement [15].

Correction for ν_e component

Since effect of the electron neutrino component in the beam is not taken into account in the calculation of selection efficiencies ($\epsilon_{\nu_\mu}^{SK(1kt)}$) and the ratio of the neutrino interaction

($R^{SK/1kt_{\nu_\mu}}$), a correction is required for the number of expected neutrino events in Super-Kamiokande. The correction factor C_{ν_e} is defined as following;

$$\begin{aligned}
C_{\nu_e} &= \frac{N^{SK}_{\nu_\mu} + N^{SK}_{\nu_e}}{N^{SK}_{\nu_\mu}}, \\
N^{SK}_{\nu_\mu(\nu_e)} &= N^{1kt}_{\nu_\mu(\nu_e)} \cdot R^{SK/1kt}_{\nu_\mu(\nu_e)} \cdot \frac{POT_{SK}}{POT_{1kt}} \cdot \epsilon^{SK}_{\nu_\mu(\nu_e)}, \\
N^{1kt}_{\nu_\mu(\nu_e)} &= \frac{\eta^{1kt}_{\nu_\mu(\nu_e)}}{\eta^{1kt}_{\nu_\mu} + \eta^{1kt}_{\nu_e}} \cdot N^{1kt}_{int}, \\
\eta^{SK(1kt)}_{\nu_\mu} &= \int \Phi^{SK(1kt)}_{\nu_\mu} \cdot \sigma_{H_2O} \cdot M_{SK(1kt)} dE
\end{aligned}$$

where $N^{SK}_{\nu_\mu(\nu_e)}$ is the number of expected $\nu_\mu(\nu_e)$ events in Super-Kamiokande, $N^{1kt}_{\nu_\mu(\nu_e)}$ is the number of $\nu_\mu(\nu_e)$ neutrino interaction in the 1kt detector. N^{1kt}_{int} is the number of neutrino interaction in the 1kt detector defined in Equation 6.6. Then, C_{ν_e} can be transformed as

$$C_{\nu_e} = 1 - \frac{\eta^{1kt}_{\nu_e}}{\eta^{1kt}_{\nu_\mu} + \eta^{1kt}_{\nu_e}} \cdot \left(1 - \frac{\eta^{SK}_{\nu_e}/\eta^{1kt}_{\nu_e}}{\eta^{SK}_{\nu_\mu}/\eta^{1kt}_{\nu_\mu}} \cdot \frac{\epsilon^{SK}_{\nu_e}/\epsilon^{1kt}_{\nu_e}}{\epsilon^{SK}_{\nu_\mu}/\epsilon^{1kt}_{\nu_\mu}}\right)$$

and its value is estimated to be 0.966.

6.5.2 Number of Expected Events in Super-Kamiokande

The number of expected events in Super-Kamiokande is summarized in Table 6.13. In total,

$$\begin{aligned}
N^{SK}_{exp} &= 80.6 \pm 0.3(stat.)^{+4.8}_{-4.9}(syst.) && (6.9) \\
&= 80.6^{+4.8}_{-4.9}(stat. + syst.) && (6.10)
\end{aligned}$$

events are expected for 4.79 × 10^{19}P.O.T., in the case of no neutrino oscillation. The statistical error comes from the number of observed events in the 1kt detector. The sources of the systematic error are described in Section 6.5.3.

6.5.3 Systematic Error on number of expected events in Super-Kamiokande

Systematic errors on N^{SK}_{exp} are summarized in Table 6.14. Each item is explained below.

- **P.O.T. correction**
  The error for the P.O.T. correction is given by Formula 6.2.
- **ν spectrum**
  The selection efficiency at Super-Kamiokande (1kt), $\epsilon^{SK(1kt)}_{\nu_\mu}$, has an energy dependence as shown in Figure 6.15(6.24). The ratio of the number of neutrino interaction ($R^{SK/1kt}_{\nu_\mu}$) also has the energy dependence. The uncertainty in the neutrino energy spectrum affects

period	Jun.99	Nov.99	Jan.00	Feb.00	Mar.00	May.00	Jun.00
Target diameter	$20mm\phi$	$30mm\phi$					
Horn current	200kA	250kA					
P.O.T.$_{SK}$($\times 10^{18}$)	3.10	3.57	2.22	4.04	3.70	2.56	3.76
P.O.T.$_{1kt}$($\times 10^{18}$)	2.60	2.62	1.81	3.74	3.35	2.42	3.17
N_{obs}^{1kt}	4282	4923	3576	7139	6234	3705	4933
N_{int}^{1kt}	7206	8351	6013	11857	10567	7573	10130
C_{ν_e}	0.996						
$R_{\nu_\mu}^{SK/1kt}$($\times 10^{-4}$)	6.81	6.71					
$\epsilon_{\nu_\mu}^{SK}$	0.781	0.785					
N_{exp}^{SK}	4.55	5.97	3.87	6.73	6.14	4.19	6.31

period	Jan.01	Feb.01	Mar.01	Apr.01	May.01	Jun.01	Jul.01
Target diameter	$30mm\phi$						
Horn current	250kA						
P.O.T.$_{SK}$($\times 10^{18}$)	3.20	5.04	4.60	2.76	1.75	6.12	1.54
P.O.T.$_{1kt}$($\times 10^{18}$)	2.92	4.75	4.27	2.47	1.60	5.79	1.43
N_{obs}^{1kt}	5746	9213	8228	4743	3113	11430	2759
N_{int}^{1kt}	9420	15491	13888	8004	5236	19102	4645
C_{ν_e}	0.996						
$R_{\nu_\mu}^{SK/1kt}$($\times 10^{-4}$)	6.71						
$\epsilon_{\nu_\mu}^{SK}$	0.785						
N_{exp}^{SK}	5.42	8.63	7.87	4.70	3.00	10.59	2.63

$$Total: \quad N_{exp}^{SK} \quad = \quad 80.6 \pm 0.3(stat.)$$

Table 6.13: Number of expected events in Super-Kamiokande.

period	Jun.99	Nov.99	Jan.00	Feb.00	Mar.00	May.00	Jun.00
N^{SK}_{exp}	4.55	5.97	3.87	6.73	6.14	4.19	6.31
from N^{1kt}_{int}	4.4%	4.5%	4.3%	4.3%	4.3%	4.5%	4.5%
P.O.T. correction	1.0%	1.6%	1.1%	0.5%	0.6%	0.3%	1.0%
from SK	2.3%						
NC/CC ratio	$^{+0.6}_{-0.7}\%$						
inelastic/elastic	$^{+0.8}_{-1.2}\%$						
ν spectrum	±3.2%						
$200kA$	1.5%						
Total	$^{+6.3}_{-6.3}\%$	$^{+6.3}_{-6.3}\%$	$^{+6.0}_{-6.1}\%$	$^{+5.9}_{-6.0}\%$	$^{+6.0}_{-6.0}\%$	$^{+6.1}_{-6.1}\%$	$^{+6.1}_{-6.2}\%$
1kt statistics	0.4%						

period	Jan.01	Feb.01	Mar.01	Apr.01	May.01	Jun.01	Jul.01
N^{SK}_{exp}	5.42	8.63	7.87	4.70	3.00	10.59	2.63
from N^{1kt}_{int}	4.3%	4.3%	4.3%	4.3%	4.3%	4.3%	4.3%
P.O.T. correction	0.5%	0.3%	0.4%	0.6%	0.5%	0.4%	0.3%
from SK	2.3%						
NC/CC ratio	$^{+0.6}_{-0.7}\%$						
inelastic/elastic	$^{+0.8}_{-1.2}\%$						
ν spectrum	±3.2%						
$200kA$							
Total	$^{+5.9}_{-6.0}\%$	$^{+5.9}_{-6.0}\%$	$^{+5.9}_{-6.0}\%$	$^{+6.0}_{-6.0}\%$	$^{+5.9}_{-6.0}\%$	$^{+5.9}_{-6.0}\%$	$^{+5.9}_{-6.0}\%$
1kt statistics	0.4%						

$$Total : N^{SK}_{exp} = 80.6 \pm 0.3(stat.)^{+4.8}_{-4.9}(syst.)$$

Table 6.14: Systematic errors on N^{SK}_{exp}.

these values and results in N^{SK}_{exp}. The efficiencies and the interaction ratio are obtained by Monte Carlo simulation;

$$\epsilon^{SK}_{\nu_\mu} = \left(\frac{N^{SK}_{obs}}{N^{SK}_{gen}}\right)_{MC}, \qquad \epsilon^{1kt}_{\nu_\mu} = \left(\frac{N^{1kt}_{obs}}{N^{1kt}_{gen}}\right)_{MC}, \qquad R^{SK/1kt}_{\nu_\mu} = \left(\frac{N^{SK}_{gen}}{N^{1kt}_{gen}}\right)_{MC} \tag{6.11}$$

where $N_{gen}(N_{obs})$ is the number of generated (observed) events in Monte Carlo simulation. Thus, equation 6.7 can be simplified as following:

$$N^{SK}_{exp} = N^{1kt}_{obs\,DATA} \times \left(\frac{N^{SK}_{obs}}{N^{1kt}_{obs}}\right)_{MC} \tag{6.12}$$

The uncertainty in N^{SK}_{exp} is estimated by changing the i-th bin of the neutrino spectrum and re-weighting the Monte Carlo events. Since the uncertainty in each bin of the spectrum has common source, they are correlated. The correlation and the estimation of the error is described in Section 6.5.4.

- **Uncertainty of the cross section**

  The uncertainty caused by the absolute scale of the cross section is canceled by taking the ratio of the near to the far as shown in Equation 6.12, but the ratio of each interaction mode is not canceled. Two uncertainties, the ratio of NC cross section to CC ($\sigma_{\mathrm{NC}}/\sigma_{\mathrm{CC}}$), and the ratio of inelastic cross section to that of CC quasi-elastic and NC elastic ($\sigma_{\mathrm{inelastic}}/\sigma_{\mathrm{elastic}}$), are taken into account. The central values of those ratios are $\sigma_{\mathrm{NC}}/\sigma_{\mathrm{CC}} = 0.16$ and $\sigma_{\mathrm{inelastic}}/\sigma_{\mathrm{elastic}} = 2.0$ for fully-contained events in Super-Kamiokande.

  Each of the ratios was changed by ±30%, which is suitable to cover the experimental data (Figure B.2,B.3), and re-weighted Monte Carlo events. Their errors are estimated to be $^{+0.6}_{-0.7}\%$ and $^{+0.8}_{-1.2}\%$ for NC/CC and inelastic/elastic, respectively.

- **Neutrino beam configuration for June 1999**

  The neutrino spectrum for June 1999 and since November 1999 are different, as shown in Figure A.6. This affects to N^{SK}_{exp} by 1.5%.

6.5.4 Correlation Between the Spectrum

To consider the correlation between each bin of the neutrino beam spectrum and to parameterize sources of uncertainties in the spectrum, an associated error matrix M is constructed, which is defined as the covariance;

$$M_{ij} = \overline{\epsilon_i \cdot \epsilon_j} \tag{6.13}$$

Here, ϵ_i is the fractional deviation of the i-th spectrum bin ϕ_i. It is calculated by changing parameters in the neutrino beam Monte Carlo;

$$\epsilon_i = \frac{\Delta\phi_i}{\phi_i} \tag{6.14}$$

where $\Delta\phi_i$ is the difference of the spectrum from the nominal case. The correlation coefficient of the error matrix, ρ_{ij}, is given as following:

$$\rho_{ij} \equiv M_{ij}/\sigma_i\sigma_j \tag{6.15}$$

where σ_i is the squared roots of the diagonal elements of the matrix. The diagonal error σ_i corresponds to the regular symmetric error if there were no correlation between ϵ_is.

The neutrino fluxes at 1kt and Super-Kamiokande, ϕ_i^{1kt} and ϕ_i^{SK}, respectively, are mapped into 6 bins. The first 5 bins are for the energies from 0 to 2.5 GeV and the last bin is for those greater than 2.5 GeV. The correlation between the near neutrino flux and the far one is considered as well, by concatenating the spectra ϕ_i^{SK} and ϕ_i^{1kt} into a 12 binned one as following:

$$\phi_i = \begin{cases} \phi_i^{1kt} & (\text{for } i = 1, 6) \\ \phi_i^{SK} & (\text{for } i = 7, 12) \end{cases} \tag{6.16}$$

The uncertainty in the proton beam targeting and pion production model are considered to obtain the error matrix.

- Proton beam targeting
  The stability of center of the proton beam is within ± 1.5 mm as shown in Figure 3.13. The injection position dependence and the injection angle dependence of the neutrino spectrum is estimated with a Monte Carlo simulation.

  The effect of the proton beam targeting is estimated by shifting the proton beam in Monte Carlo simulation. The shifts are ± 1.5 mm in horizontal direction and ± 1.5 mm in vertical direction from the nominal case. Table 6.15 shows the estimated correlation coefficient ρ_{ij} and the diagonal error σ_i.

  The injection angle of the proton beam is changed by ± 1 mrad and ± 1 mrad for x and y, respectively, with respect to the nominal beam axis. The deviation of the injection angle is estimated from the fluctuation of the beam center (± 1.5 mm) and the distance between the last magnet and TARGET-SPIC (2 m). Table 6.16 shows the estimated correlation coefficient ρ_{ij} and the diagonal errors σ_i.

- Pion production model
  The pion production model employed in the neutrino beam Monte Carlo is Cho model (Section A.2). This model is strongly favored by the momentum and angle distribution of the pion obtained by PIMON measurement [15].

  The uncertainty in neutrino spectrum is estimated by varying the parameters in Equation A.1. Of the 8 parameters in the pion production model, 7 parameters were varied within their 90% C.L. limits and $2^7 = 128$ spectra are obtained. The normalization term, C_1, is not varied because it is canceled by taking the ratio of the near to the far in Equation 6.12. Table 6.17 shows the correlation coefficient coefficient ρ_{ij} and the diagonal errors σ_i of the covariance of 128 spectra.

Finally, the total error matrix M is obtained by summing up the matrices described above:

$$M = M^{\text{pos}} + M^{\text{ang}} + M^{\text{pion}} \tag{6.17}$$

j\i		ϕ^{1kt}						ϕ^{SK}					
		1	2	3	4	5	6	7	8	9	10	11	12
ϕ^{1kt}	1	1.00	-0.03	-0.12	-0.36	-0.48	-0.48	-0.31	0.15	0.05	-0.42	0.02	-0.54
	2	-0.03	1.00	0.01	0.36	0.37	0.56	-0.14	0.00	-0.56	0.47	0.48	0.72
	3	-0.12	0.01	1.00	0.20	-0.07	-0.46	0.56	0.25	0.80	-0.70	-0.42	-0.32
	4	-0.36	0.36	0.20	1.00	-0.40	-0.08	0.80	0.80	0.03	0.04	-0.56	0.19
	5	-0.48	0.37	-0.07	-0.40	1.00	0.84	-0.59	-0.86	-0.43	0.61	0.82	0.74
	6	-0.48	0.56	-0.46	-0.08	0.84	1.00	-0.55	-0.62	-0.82	0.94	0.81	0.96
ϕ^{SK}	7	-0.31	-0.14	0.56	0.80	-0.59	-0.55	1.00	0.83	0.60	-0.49	-0.90	-0.32
	8	0.15	0.00	0.25	0.80	-0.86	-0.62	0.83	1.00	0.35	-0.44	-0.84	-0.40
	9	0.05	-0.56	0.80	0.03	-0.43	-0.82	0.60	0.35	1.00	-0.92	-0.72	-0.77
	10	-0.42	0.47	-0.70	0.04	0.61	0.94	-0.49	-0.44	-0.92	1.00	0.68	0.89
	11	0.02	0.48	-0.42	-0.56	0.82	0.81	-0.90	-0.84	-0.72	0.68	1.00	0.67
	12	-0.54	0.72	-0.32	0.19	0.74	0.96	-0.32	-0.40	-0.77	0.89	0.67	1.00
σ_i		0.2	0.5	0.9	1.3	3.9	4.6	3.1	2.0	1.7	2.2	6.4	13.0

Table 6.15: Correlation coefficient for center of the proton beam. The bottom row shows the diagonal errors in percent.

j\i		ϕ^{1kt}						ϕ^{SK}					
		1	2	3	4	5	6	7	8	9	10	11	12
ϕ^{1kt}	1	1.00	-0.76	0.24	-0.55	0.23	0.30	-0.39	0.81	0.29	0.11	0.05	0.37
	2	-0.76	1.00	0.10	0.04	0.11	0.12	-0.18	-0.76	-0.82	0.03	0.24	0.17
	3	0.24	0.10	1.00	-0.07	0.97	0.70	-0.85	0.04	-0.23	0.45	0.80	0.61
	4	-0.55	0.04	-0.07	1.00	0.03	0.00	0.57	-0.61	0.30	0.42	0.25	-0.24
	5	0.23	0.11	0.97	0.03	1.00	0.84	-0.79	-0.09	-0.30	0.65	0.92	0.73
	6	0.30	0.12	0.70	0.00	0.84	1.00	-0.61	-0.25	-0.51	0.88	0.93	0.96
ϕ^{SK}	7	-0.39	-0.18	-0.85	0.57	-0.79	-0.61	1.00	-0.23	0.47	-0.19	-0.57	-0.68
	8	0.81	-0.76	0.04	-0.61	-0.09	-0.25	-0.23	1.00	0.55	-0.46	-0.41	-0.17
	9	0.29	-0.82	-0.23	0.30	-0.30	-0.51	0.47	0.55	1.00	-0.29	-0.44	-0.63
	10	0.11	0.03	0.45	0.42	0.65	0.88	-0.19	-0.46	-0.29	1.00	0.87	0.76
	11	0.05	0.24	0.80	0.25	0.92	0.93	-0.57	-0.41	-0.44	0.87	1.00	0.82
	12	0.37	0.17	0.61	-0.24	0.73	0.96	-0.68	-0.17	-0.63	0.76	0.82	1.00
σ_i		0.4	0.4	1.0	0.6	5.8	8.0	2.6	1.1	2.8	3.8	11.6	13.7

Table 6.16: Correlation coefficient for the injection angle dependence. The bottom row shows the diagonal errors in percent.

j\i		ϕ^{1kt}						ϕ^{SK}					
		1	2	3	4	5	6	7	8	9	10	11	12
ϕ^{1kt}	1	1.00	0.57	0.27	0.17	0.11	0.01	0.91	0.55	0.29	0.18	0.13	0.02
	2	0.57	1.00	0.88	0.69	0.44	0.16	0.64	0.95	0.90	0.73	0.47	0.18
	3	0.27	0.88	1.00	0.92	0.74	0.47	0.35	0.79	0.99	0.94	0.76	0.48
	4	0.17	0.69	0.92	1.00	0.92	0.72	0.26	0.61	0.88	0.99	0.92	0.73
	5	0.11	0.44	0.74	0.92	1.00	0.92	0.12	0.31	0.68	0.88	0.98	0.92
	6	0.01	0.16	0.47	0.72	0.92	1.00	-0.03	0.04	0.40	0.65	0.88	0.99
ϕ^{SK}	7	0.91	0.64	0.35	0.26	0.12	-0.03	1.00	0.70	0.37	0.28	0.12	-0.03
	8	0.55	0.95	0.79	0.61	0.31	0.04	0.70	1.00	0.81	0.65	0.34	0.05
	9	0.29	0.90	0.99	0.88	0.68	0.40	0.37	0.81	1.00	0.90	0.70	0.43
	10	0.18	0.73	0.94	0.99	0.88	0.65	0.28	0.65	0.90	1.00	0.88	0.67
	11	0.13	0.47	0.76	0.92	0.98	0.88	0.12	0.34	0.70	0.88	1.00	0.88
	12	0.02	0.18	0.48	0.73	0.92	0.99	-0.03	0.05	0.43	0.67	0.88	1.00
σ_i		9.7	8.0	10.9	15.6	23.9	39.4	10.5	8.8	10.4	14.5	22.8	39.8

Table 6.17: Correlation coefficient for the pion production model. The bottom row shows the diagonal errors in percent.

where M^{pos} is the error matrix for the proton beam injection position dependence, M^{ang} is for the injection angle dependence and M^{pion} is for the pion production model dependence. Table 6.18 shows its correlation coefficient ρ_{ij} and the diagonal errors σ_i. The diagonal errors are consistent with the systematic errors on PIMON measurement [15], which is shown Table 6.19.

The square of the error caused by the uncertainty of the spectrum, $(\delta N^{SK}_{exp})^2$ is obtained as following:

$$\left(\delta N^{SK}_{exp}\right)^2 \quad = \quad \vec{D}^T M \vec{D} \tag{6.18}$$

and found to be $\delta N^{SK}_{exp} = 3.2\%$. Here, $\vec{D}$ is the deviation vector

$$\vec{D} = \begin{pmatrix} \dfrac{\partial N^{SK}_{exp}}{\partial \epsilon_1} \\ \vdots \\ \dfrac{\partial N^{SK}_{exp}}{\partial \epsilon_{12}} \end{pmatrix} \tag{6.19}$$

which is estimated by re-weighting the i-th bin of the neutrino spectrum by factor $(1+\sigma_i)$ in Monte Carlo events.

6.6 Event Summary

Neutrino events in 22.5 kt fiducial volume of Super-Kamiokande is analyzed for the whole running period from June 1999 to July 2001 as described in Chapter 6.3. As a result, total number of observed fully-contained events 56 when $80.6 \pm 0.3(stat.)^{+4.8}_{-4.9}(syst.)$ events are expected.

j\i		ϕ^{1kt}						ϕ^{SK}					
		1	2	3	4	5	6	7	8	9	10	11	12
ϕ^{1kt}	1	1.00	0.56	0.27	0.17	0.11	0.01	0.84	0.54	0.28	0.18	0.11	0.02
	2	0.56	1.00	0.88	0.69	0.42	0.16	0.59	0.91	0.84	0.70	0.42	0.17
	3	0.27	0.88	1.00	0.91	0.72	0.46	0.32	0.77	0.94	0.89	0.67	0.44
	4	0.17	0.69	0.91	1.00	0.87	0.69	0.27	0.60	0.84	0.95	0.78	0.66
	5	0.11	0.42	0.72	0.87	1.00	0.91	0.04	0.26	0.59	0.86	0.94	0.89
	6	0.01	0.16	0.46	0.69	0.91	1.00	-0.08	0.01	0.33	0.67	0.84	0.96
ϕ^{SK}	7	0.84	0.59	0.32	0.27	0.04	-0.08	1.00	0.68	0.38	0.22	-0.02	-0.10
	8	0.54	0.91	0.77	0.60	0.26	0.01	0.68	1.00	0.78	0.58	0.22	0.01
	9	0.28	0.84	0.94	0.84	0.59	0.33	0.38	0.78	1.00	0.78	0.50	0.28
	10	0.18	0.70	0.89	0.95	0.86	0.67	0.22	0.58	0.78	1.00	0.85	0.67
	11	0.11	0.42	0.67	0.78	0.94	0.84	-0.02	0.22	0.50	0.85	1.00	0.85
	12	0.02	0.17	0.44	0.66	0.89	0.96	-0.10	0.01	0.28	0.67	0.85	1.00
σ_i		9.7	8.0	11.0	15.7	24.9	40.5	11.2	9.1	10.9	15.1	26.3	44.1

Table 6.18: Total correlation coefficient of neutrino spectrum. The bottom row shows the diagonal errors in percent.

i	ϕ^{1kt}						ϕ^{SK}					
	1	2	3	4	5	6	7	8	9	10	11	12
σ_i			$^{+9.2}_{-9.6}$	$^{+10.7}_{-9.9}$	$^{+12.1}_{-17.7}$	$^{+47.7}_{-34.0}$			± 13.8	$^{+8.1}_{-11.9}$	$^{+10.6}_{-15.8}$	$^{+42.1}_{-39.5}$

Table 6.19: Systematic errors in percent on neutrino spectrum obtained by PIMON measurement. There is no PIMON measurement for neutrinos below 1 GeV (i = $1, 2, 7$ and 8) due to the Čerenkov threshold of pions.

Chapter 7

Results

7.1 Comparison between the observation and the expectation

A total of 56 fully-contained events are observed when $80.6 \pm 0.3(stat.)^{+4.8}_{-4.9}(syst.)$ events are expected. The number of the observation is clearly small than expected.

A hypothesis test is performed with a statistical Monte Carlo. A large number of Poisson distributions are generated with average around 80.6 smeared by a Gaussian distribution with width of 4.9. Here, the difference between 4.8 and 4.9 us neglected. The probability of this observation is calculated as an integration of Poisson probabilities of less than or equal to 56 events, given as following:

$$P(x \leq n; \mu_0 \pm \Delta\mu) = \frac{1}{\sqrt{2\pi}\Delta\mu} \int_0^\infty \sum_{x=0}^{n} \frac{e^{-\mu}\mu^x}{x!} \exp\left(-\frac{1}{2}\left(\frac{\mu - \mu_0}{\Delta\mu}\right)^2\right) d\mu \tag{7.1}$$

where $n = 56$ is the number of observed events, $\mu_0 = 80.6$ is the center value of number of expected events and $\Delta\mu$ is its error.

The test is performed 10^7 times. The obtained probability is 0.7% (Figure 7.1). The probability of null oscillation hypothesis is excluded with more than 99% C.L. by one side test.

7.2 Neutrino Oscillation Analysis

In this section, the result of $\nu_\mu \leftrightarrow \nu_\tau$ two flavor neutrino oscillation analysis is described. The surviving probability for a muon neutrino of energy E_ν in $\nu_\mu \rightarrow \nu_\tau$ oscillation is given following equation:

$$P(\nu_\mu \rightarrow \nu_\mu) \quad = \quad 1 - \sin^2 2\theta \sin^2\left(1.27\frac{\Delta m^2[\mathrm{eV}^2]L[km]}{E_\nu[\mathrm{GeV}]}\right) \tag{7.2}$$

Using the mean neutrino energy $\langle E_\nu \rangle = 1.3$ GeV and its flight length $L = 250$ km, the most sensitive Δm^2 is expected to be

$$\frac{2.48\langle E_\nu \rangle}{2L} = 7 \times 10^{-3}\mathrm{eV}^2 \tag{7.3}$$

at the maximum mixing angle.

A χ^2 test is performed to evaluate the goodness of the fit between the data and the expectation.

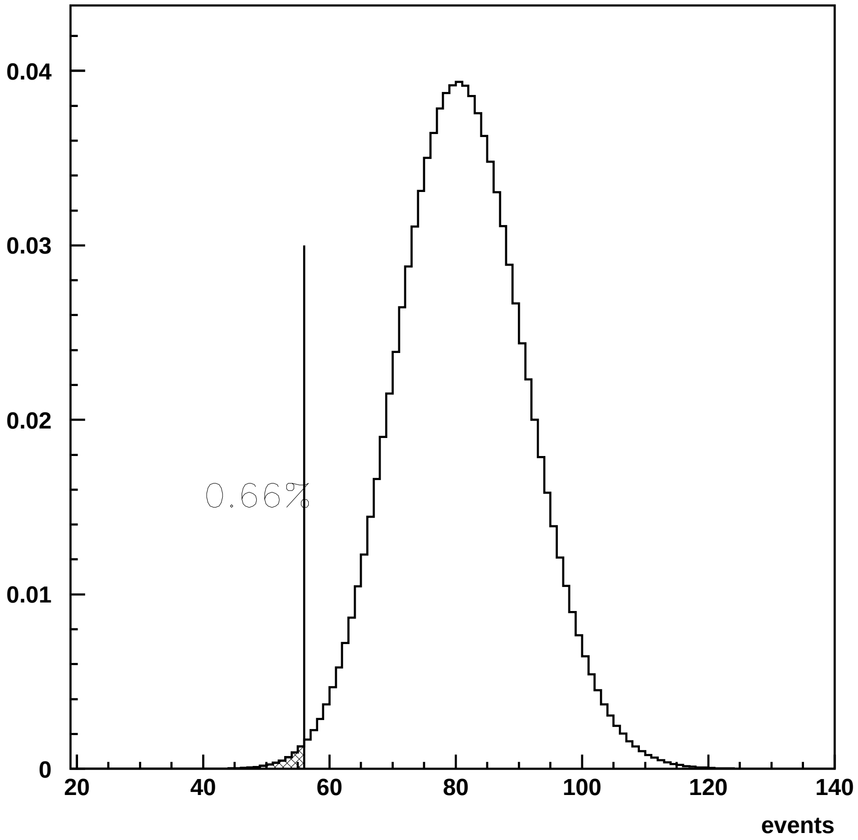

Figure 7.1: Result of statistical test. The area less than or equal to 56 event occupies 0.7% of the histogram. The distribution is generated with 10^7 trials of random number generation obeying Poisson distribution with its mean smeared by a Gaussian distribution. Its area is normalized to unity.

7.2.1 Definition of χ^2

The fully-contained single-ring μ-like sample are used for the χ^2 test because it is possible to reconstruct the neutrino energy as shown in Equation 6.4. A total of 30 fully-contained single-ring μ-like events are selected to reconstruct the neutrino energy. The number of expected single-ring μ-like events is 44.0 (Table 7.1).

The reconstructed neutrino energies are mapped into 6 bins. The first 5 bins are from 0 to 2.5 GeV and the last bin is for those greater than 2.5 GeV. Since the number of events in each bin is relatively small, χ^2 for Poisson-distributed data was applied to the fit:

$$\chi^2 = \sum_{i=1}^{6} \left[2\left(E^i_{exp} - E^i_{obs}\right) + 2E^i_{obs} \log_e \frac{E^i_{obs}}{E^i_{exp}} \right] + \frac{\alpha^2}{\sigma^2_\alpha} + \frac{\beta^2}{\sigma^2_\beta} + \frac{\gamma^2}{\sigma^2_\gamma} + \frac{\delta^2}{\sigma^2_\delta} + \vec{\epsilon}^T M^{-1} \vec{\epsilon} \tag{7.4}$$

where E^i_{obs} is the observed number of events in the i-th bin. $E^i_{exp} = E^i_{exp}(\Delta m^2, \theta; \alpha, \beta, \gamma, \delta, \vec{\epsilon})$ is the expected number of events in the i-th bin, with parameters $(\alpha, \beta, \ldots, \vec{\epsilon})$ constrained by systematic uncertainties. M is the error matrix for the neutrino spectrum estimated in Section 6.5.4. The source of systematic errors are assumed to obey a Gaussian distribution in this calculation.

7.2.2 Systematic errors

There are several systematic uncertainties in the neutrino energy distributions for both observation and expectation. The systematic uncertainties are considered by re-weighting the expected number of events defined in Equation 6.12:

$$\begin{aligned}
N^{SK}_{exp} &= (1+\alpha) N^{1kt}_{obs\,DATA} \left(\frac{N^{SK}_{obs}}{N^{1kt}_{obs}} \right)_{MC} \\
&= (1+\alpha) N^{1kt}_{obs\,DATA} \frac{\sum_j W_\sigma \left(1+\epsilon_j\right) n^{SK}_j P(\Delta m^2, \theta)}{\sum_j W_\sigma \left(1+\epsilon_j\right) n^{1kt}_j} \qquad (7.5) \\
W_\sigma &= \begin{cases} 1 & \text{for CC quasi-elastic interactions} \\ 1+\beta & \text{for NC elastic interactions} \\ 1+\gamma & \text{for CC inelastic interactions} \\ (1+\beta)(1+\gamma) & \text{for NC inelastic interactions} \end{cases}
\end{aligned}$$

Here, $n^{SK(1kt)}_j$ is the number of Monte Carlo events for Super-Kamiokande (1kt) whose true neutrino energy belongs to the j-th bin of the neutrino spectrum ϕ_j which is defined in Section 6.5.4. $P(\Delta m^2, \theta)$ is the surviving probability for a muon neutrino of momentum p in $\nu_\mu \leftrightarrow \nu_\tau$ oscillation. The meaning and the estimated systematic uncertainties of the parameters, $(\alpha, \beta, \ldots, \vec{\epsilon})$, are described below.

- α **: Absolute normalization**
  Systematic errors which are supposed to be uncorrelated are taken in account for the uncertainty in the absolute normalization. Considered are errors in N^{1kt}_{int}, P.O.T. correction, errors from Super-Kamiokande, the statistics of N^{1kt}_{obs}, single-ring/multi-ring separation and particle identification. The former 4 errors are described in Section 6.5.3. The latter 2 errors are introduced for selecting single-ring μ-like events.

period	Jun.99	Nov.99	Jan.00	Feb.00	Mar.00	May.00	Jun.00
N_{exp}^{SK}(1-ring μ-like)	2.48	3.26	2.11	3.67	3.35	2.29	3.44
from N_{int}^{1kt}	4.4%	4.5%	4.3%	4.3%	4.3%	4.5%	4.5%
P.O.T. correction	1.0%	1.6%	1.1%	0.5%	0.6%	0.3%	1.0%
from SK	2.3%						
1-ring/multi-ring separation	6%						
particle identification	3%						
1kt statistics	0.4%						
Total	8.4%	8.6%	8.4%	8.3%	8.3%	8.4%	8.5%

period	Jan.01	Feb.01	Mar.01	Apr.01	May.01	Jun.01	Jul.01
N_{exp}^{SK}(1-ring μ-like)	2.95	4.71	4.29	2.56	1.64	5.78	1.43
from N_{int}^{1kt}	4.3%	4.3%	4.3%	4.3%	4.3%	4.3%	4.3%
P.O.T. correction	0.5%	0.3%	0.4%	0.6%	0.5%	0.4%	0.3%
from SK	2.3%						
1-ring/multi-ring separation	6%						
particle identification	3%						
1kt statistics	0.4%						
Total	8.3%	8.3%	8.3%	8.3%	8.3%	8.3%	8.3%

$$Total : N_{exp}^{SK}(\text{1-ring } \mu\text{-like}) = 44.0 \pm 3.7$$

Table 7.1: Systematic errors for the normalization.

The number of rings in an event is obtained by a ring-counting program. The uncertainty in ring-counting is estimated by comparing the result of ring-counting program and that of visual scanning, which is found to be 6%.

The uncertainty in particle identification is estimated by twice the mis-identification probability in a particle identification program. The mis-identification probability is obtained as the fraction of e-like events in the ν_μ charged current quasi-elastic sample in a Monte Carlo simulation and found to be 1.5%.

The absolute normalization is estimated to be $\sigma_\alpha = 8.4\%$ as shown Table 7.1.

- β **: Ratio of NC/CC cross section**
  The uncertainty of the ratio of NC cross section to that of CC is estimated to be $\sigma_\beta = 30\%$ as described in Section 6.5.3.

- γ **: Ratio of inelastic/elastic cross section**
  The uncertainty of the ratio of inelastic cross section to CC quasi-elastic and NC elastic cross section is estimated to be $\sigma_\gamma = 30\%$ as described in Section 6.5.3.

- δ **: Absolute energy scale of Super-Kamiokande**

The absolute energy scale of Super-Kamiokande is estimated to be $\sigma_\delta = 2.5\%$ (Section 4.6.5). Instead of mapping the expectation of reconstructed neutrino energy to the bin after scaling by factor $(1+\delta)$, the effect of the absolute energy scale is taken into account with linear approximation as following:

$$E^{i}_{exp}{}' = E^{i}_{exp} + \frac{i}{2} \cdot \delta \left(E^{i}_{exp} + E^{i+1}_{exp} \right) - \frac{i-1}{2} \cdot \delta \left(E^{i-1}_{exp} + E^{i}_{exp} \right) \tag{7.6}$$

- $\vec{\epsilon} = (\epsilon_1, \epsilon_2, \ldots, \epsilon_{12})$ **: Spectrum of the neutrino beam**
  The uncertainty and the correlation in the spectrum of the neutrino beam are estimated in Section 6.5.4.

7.2.3 $\nu_\mu \leftrightarrow \nu_\tau$ oscillation

The χ^2 is minimized by scanning the parameter space $(\sin^2 2\theta, \Delta m^2)$ and optimizing the systematic error parameters $(\alpha, \beta, \ldots, \vec{\epsilon})$ at each point. The unphysical parameter region $(\sin^2 2\theta > 1)$ is also scanned in order to demonstrate the validity of the analysis.

The minimum χ^2 is 9.27/4 d.o.f. obtained at $(\sin^2 2\theta, \Delta m^2) = (1.00, 2.7 \times 10^{-3}\mathrm{eV}^2)$. Its C.L. is about 6%. Including the unphysical region, the minimum χ^2 is 9.26/4 d.o.f. at $(\sin^2 2\theta, \Delta m^2) = (1.02, 2.7 \times 10^{-3}\mathrm{eV}^2)$. The χ^2 without neutrino oscillation is 15.86, and the null oscillation hypothesis is excluded with more than 97% C.L. Table 7.2 shows the summary of the best fit systematic parameters. The reconstructed neutrino energy spectrum for single-ring μ-like events with the best fit result of $\nu_\mu \leftrightarrow \nu_\tau$ oscillation are shown in Figure 7.2.

Figure 7.3 shows the result from the oscillation analysis. The contours show the 68%, 90% and 95% C.L. allowed region which are defined to be $\chi^2 = \chi^2_{min} + 2.3$, $\chi^2 = \chi^2_{min} + 4.6$ and $\chi^2 = \chi^2_{min} + 6.2$, respectively. The best fit position, $(\sin^2 2\theta, \Delta m^2) = (1.00, 2.7 \times 10^{-3}\mathrm{eV}^2)$, is shown with the symbol "★" in the figure. The result is consistent with the atmospheric neutrino observation in the Super-Kamiokande experiment [12], which is shown in Figure 1.2.

α	Absolute normalization	1.6%	(8.4%)
β	Ratio of NC/CC cross section	1.5%	(30%)
γ	Ratio of inelastic/elastic cross section	-4.6%	(30%)
δ	Absolute energy scale	-0.4%	(2.5%)
ϵ_1	Neutrino spectrum	-0.2%	(9.7%)
ϵ_2		-0.5%	(8.0%)
ϵ_3		0.0%	(11.0%)
ϵ_4		0.8%	(15.7%)
ϵ_5		3.5%	(24.9%)
ϵ_6		7.9%	(40.2%)
ϵ_7		-0.8%	(11.1%)
ϵ_8		-0.9%	(9.0%)
ϵ_9		-0.3%	(10.7%)
ϵ_{10}		0.8%	(14.8%)
ϵ_{11}		3.6%	(25.8%)
ϵ_{12}		9.2%	(42.9%)

Table 7.2: Summary of the best fit systematic uncertainty parameters of the $\nu_\mu \leftrightarrow \nu_\tau$ oscillation analysis. The best fit parameters are shown is the second column, and the estimated systematic errors are shown in the third column. The estimated systematic errors for the neutrino spectrum are the diagonal errors of the error matrix.

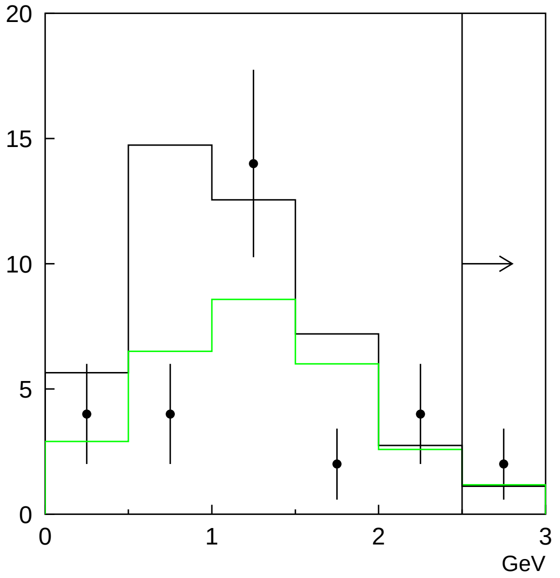

Figure 7.2: Reconstructed neutrino energy spectrum for single-ring μ-like events in Super-Kamiokande. The distribution is integrated above 2.5 GeV. The black line shows the expected distribution without oscillation. The green line shows the best fit result from $\nu_\mu \leftrightarrow \nu_\tau$ oscillation analysis.

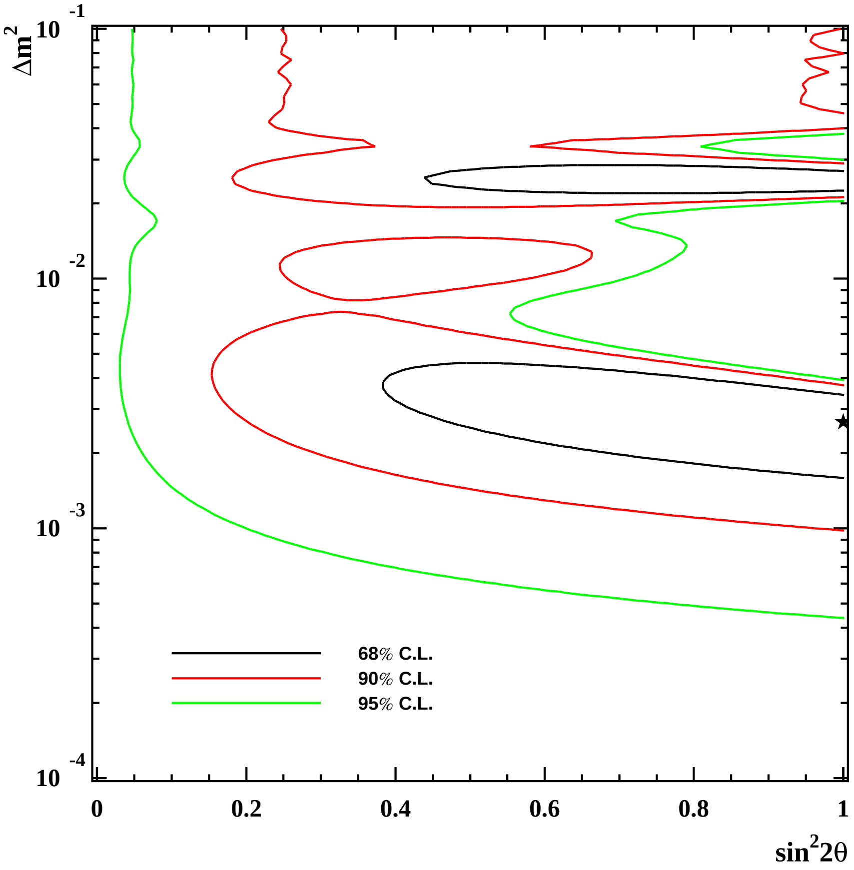

Figure 7.3: Contour plots of allowed regions of parameters $(\sin^2 2\theta, \Delta m^2)$ in $\nu_\mu \leftrightarrow \nu_\tau$ oscillation. Black, red and green lines show the 68%, 90% and 90% C.L. allowed regions, respectively. The symbol "★" in the figure shows the best fit position.

Chapter 8

Conclusion

The KEK to Kamioka long baseline neutrino oscillation experiment (K2K) took data successfully both at KEK and Super-Kamiokande to investigate neutrino oscillation for the period from Jun 1999 to July 2001. Accumulated are 4.79×10^{19} protons on target at the 12 GeV-PS.

Stability of the spectrum and the direction of the muon neutrino beam was confirmed by the Muon Range Detector at the near site through the entire running period. The beam was monitored spill by spill and kept stable by means of proton monitors and secondary muon monitors in the beam line. The expected neutrino spectra at the far and the near site and the far to the near flux ratio were confirmed by measuring the momentum and angular distribution of pions before decaying to neutrinos.

The expected number of events in Super-Kamiokande at 250 km from the target is estimated by extrapolating the number of observed events in the 1kt detector at 300 m from the target. It is estimated to be $80.6 \pm 0.3(stat.)^{+4.8}_{-4.9}(syst.)$ for fully-contained events during the whole run.

In Super-Kamiokande, the neutrino events are clearly isolated in the beam arrival time matching perfectly with the beam spill time of PS. The timing synchronization of Super-Kamiokande clock and the accelerator clock is carried out by using GPS and confirmed by an atomic clock for their relative accuracy. A total of 56 fully-contained events are observed during the whole run. They are background free.

Comparing the expectation and the observation at Super-Kamiokande, the probability of null-oscillation hypothesis was obtained to be 0.7%.

The $\nu_\mu \leftrightarrow \nu_\tau$ oscillation analysis is performed using 30 fully-contained 1-ring muon-like events. The best fit was obtained at $(\sin^2 2\theta, \Delta m^2) = (1.00, 2.7 \times 10^{-3}\text{eV}^2)$. This is consistent with the set of parameters suggested by atmospheric neutrinos.

Appendix A

Neutrino Beam Simulation

The neutrino beam simulation provides neutrino flux at near and far site. It simulates proton injection into the target, production of secondary pions and kaons in the target, trajectory of secondary particles through the magnetic filed of horns and their decay into neutrinos. Different configuration of horn magnets (Chapter 3.1.3) and beam injection between June 1999 and since November 1999 are taken into account in the simulation.

A.1 Proton Injection into the Target

Protons are injected to the target with the measured beam emittance. Two SPICs between the last magnet and the target, called “V39 out SPIC” and “TARGET SPIC” (Figure 3.2), are used for the emittance measurement. The former is located just after the last magnet and the latter is located just before the target.

The emittance of the proton beam is calculated by assuming that the protons do not cross over and the proton density distribution is 2-dimensional Gaussian. Figure A.1 shows the schematic view of the calculation and Figure A.2 show the results of the November 1999 configuration, where x (y) is the horizontal (vertical) beam position and dx (dy) is the beam divergence.

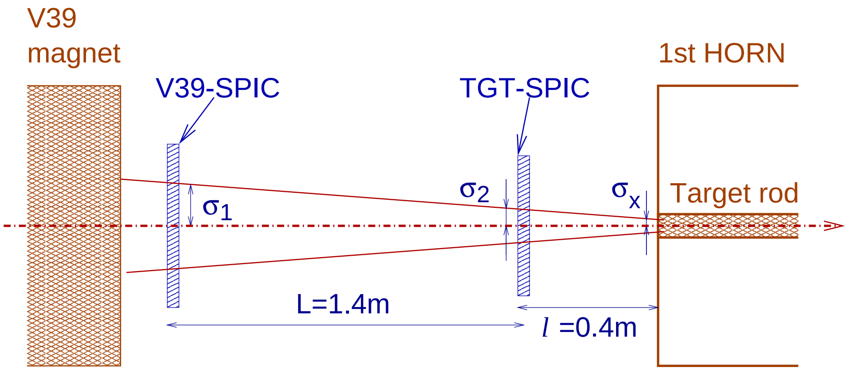

Figure A.1: Schematic view of the proton beam emittance calculation.

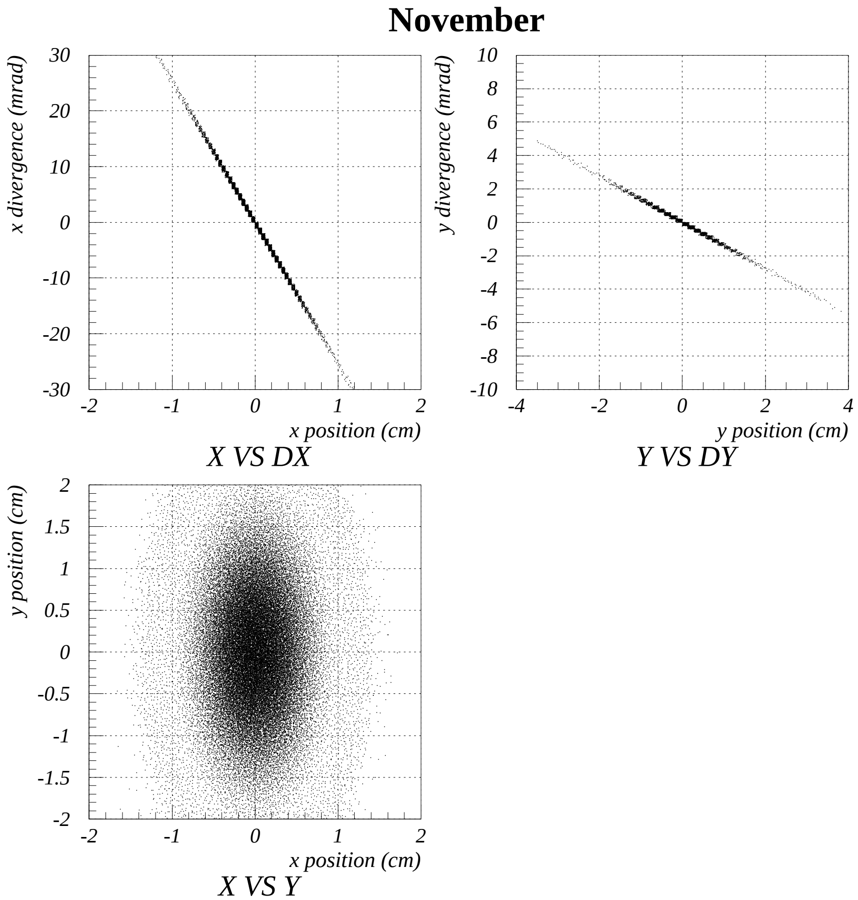

Figure A.2: Proton beam emittance for the November 1999 configuration. Top-Left: x vs dx, Top-Right: y vs dy, Bottom-Left: x vs y (proton beam distribution at the target)

A.2 Production of Secondary Pions and Kaons in the Target

There have been various pion production experiments in the energy region of K2K beam, whose results are inconsistent with one another [37, 38, 39, 41, 42, 43, 44, 45]. Some pion production models can be chosen in simulating secondary particle production in the target, which is a large ambiguity of the simulation. In the following three kinds of pion production models are compared:

1 **GCALOR/FLUKA Model** [33, 34].
GCALOR/FLUKA is one of the hadron simulation package prepared for GEANT simulation [35], which has a larger p-Al cross section than other models. It tends to produce higher energy secondary pions.

2 **Fit to Measurements (I), Sanford-Wang** [36].
This model is an experimental parameterization using compilation of three measurements: Lundy *et al.*(13.4 GeV/c) [37], Dekkers *et al.*(11.8, 18.8 and 23.1 GeV/c) [38] and Baker *et al.*(10.9, 20.9 and 30.9 GeV/c) [39]. This result is confirmed by measurement performed by Yamamoto [40].

3 **Fit to Measurements (II), Cho** [41].
This model is also an experimental parameterization, based on the result of measurement performed by Cho's group. The measurement was performed on the same proton beam at Argonne as Lundy *et al.*[37], to understand their neutrino beam better. Spectrometers are used to measure accurate differential cross sections ($d^2\sigma/d\theta dp$). The compilation of their result and other measurements are fitted using Sanford-Wang formula. Following results are used in the fit: Cho *et al.*(12.4 GeV/c) [41], Asbury *et al.*(12.5 GeV/c) [42], Marmer *et al.*(12.3 GeV/c) [43, 44] and Allaby *et al.*(19.2 GeV/c) [45].

The Sanford-Wang formula is an experimental parameterization, which gives the differential yield of the secondary particle per interacting proton ($d^2n/d\theta dp$) as following:

$$\frac{d^2n}{d\theta dp} \quad = \quad C_1 \cdot p^{C_2}\Big(1-\frac{p}{p_B}\Big)\cdot \exp\Big(-\frac{C_3\cdot p^{C_4}}{p_B^{C_5}} - C_6\cdot\theta\left(p - C_7\cdot p_B\cos^{C_8}\theta\right)\Big), \qquad \text{(A.1)}$$

where p_B and p are the momenta of the primary and secondary particle, respectively, θ is the angle between the secondary particle and the beam axis. C_i's are constants to be found by the fit. Cho *et al.*fitted the particle yield instead of the cross section. Fitted result about π^+ production in Reference [41] is summarized in Table A.1. Figure A.3 show the results of their measurements [41, 42, 43, 44] and fit results for π^+ and π^- in [41].

In GCALOR/FLUKA model, GEANT simulates everything using the GCALOR/FLUKA automatically. In the other models, only the interaction of energetic protons more than 10 GeV with the target aluminum is simulated according to the Equation A.1. The less energetic interactions are simulated according to GCALOR model. For secondary interaction of hadrons, GCALOR/FLUKA is always used. For Kaon production, [36] is referred.

The ν_μ flux dependence on the hadron production model is shown in Figure A.4. The Cho model is employed in the simulation because the momentum and angle distribution of the pion obtained by PIMON measurement strongly favored the simulation using Cho model [15].

	C_1	C_2	C_3	C_4	C_5	C_6	C_7	C_8
2. SW	227	0.65	4.05	1.63	1.66	5.03	0.172	82.7
3. Cho	196	1.08	2.15	2.31	1.98	5.73	0.137	24.1

Table A.1: The fitted parameters of the Sanford-Wang formula for π^+ production, by Sanford-Wang and Cho *et al.*[36, 41]

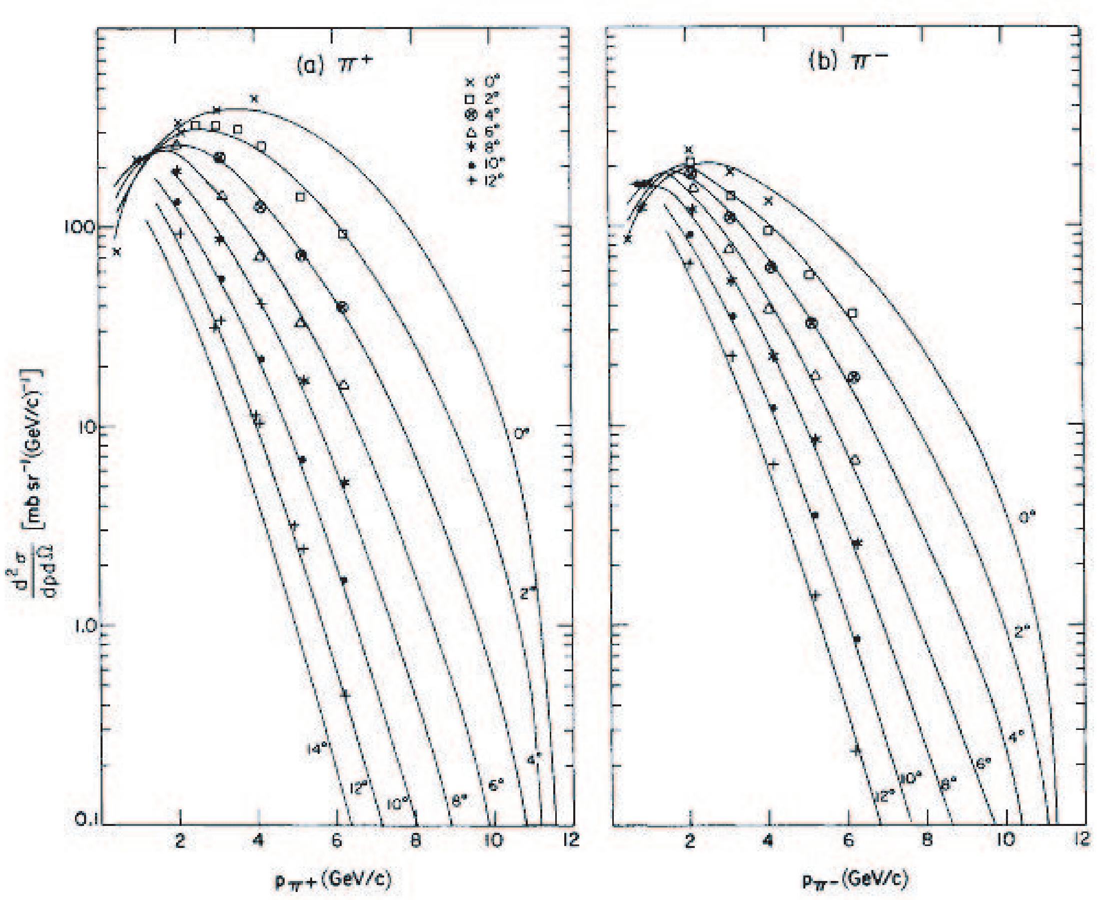

Figure A.3: Results of the pion production measurements [41, 42, 43, 44] and fitted results by Sanford-Wang formula, for π^+ (left) and π^- (right).

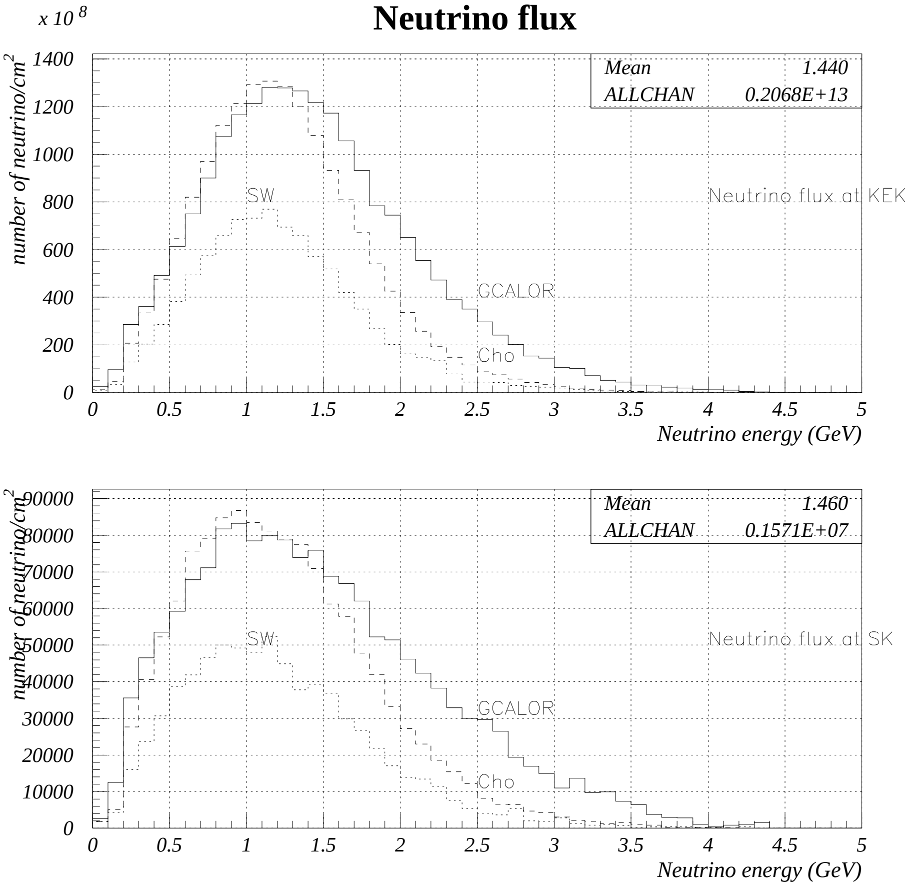

Figure A.4: Hadron production model dependence of ν_μ flux.

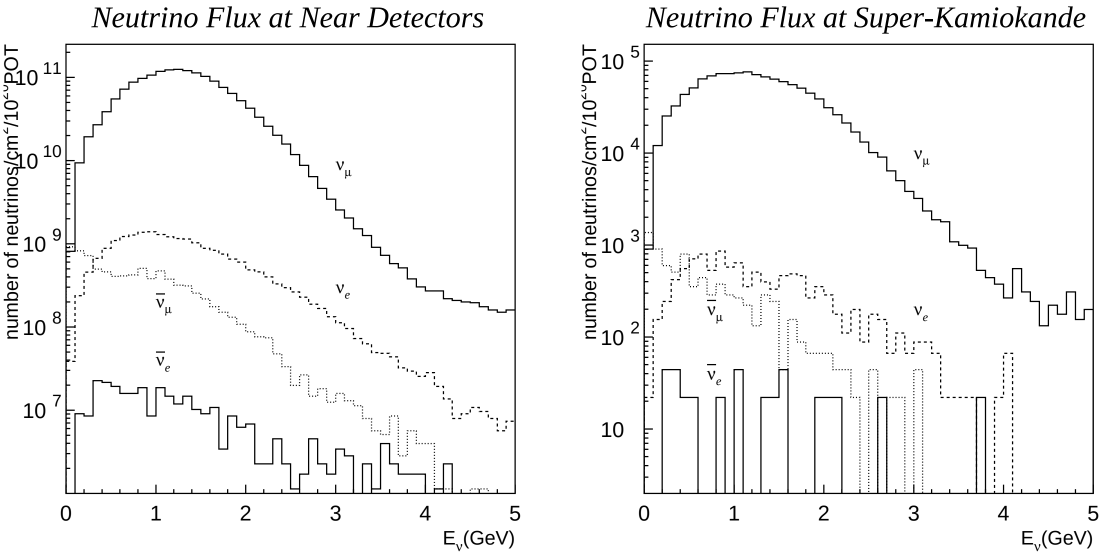

Figure A.5: Expected Neutrino spectra at KEK(left) and at Super-Kamiokande(right).

A.3 Trajectory of the Secondary Particle Through the Horn Magnet

The secondary particle is traced by Monte Carlo simulation GEANT with GCALOR hadron simulation [35, 33], through the magnetic field generated by the horn to the decay section. Magnetic fields in horns are given by calculation. As described in Chapter 3.1.3, the magnetic field inside of the first horn was measured using pickup coils to confirm the calculation. The magnetic field inside the target rod is calculated with static approximation as a function of radius.

A.4 Particles Decay into Neutrino

The dominant source of neutrino beam is pion, while a little fraction of neutrinos comes from muon decay and from kaon decay.

Figure A.5 show the expected neutrino spectra for the November 1999 configuration. The near flux is averaged over 25 cm in radius and 40 m for the far flux. The fraction of neutrinos flying toward Super-Kamiokande is 98.4%, 0.9%, 0.6%, 0.03% for ν_μ, ν_e, $\bar{\nu}_\mu$, $\bar{\nu}_e$, respectively.

Figure A.6 shows the difference of ν_μ spectra for June 1999 and since November 1999 configuration. The average neutrino energy is higher in the November configuration (1.29 GeV) than the June configuration (1.23 GeV) because the horn current was higher in the November configuration. The higher flux is expected for the higher horn current, but the absolute flux is 2.7% smaller in November configuration due to the higher pion absorption effect in the target.

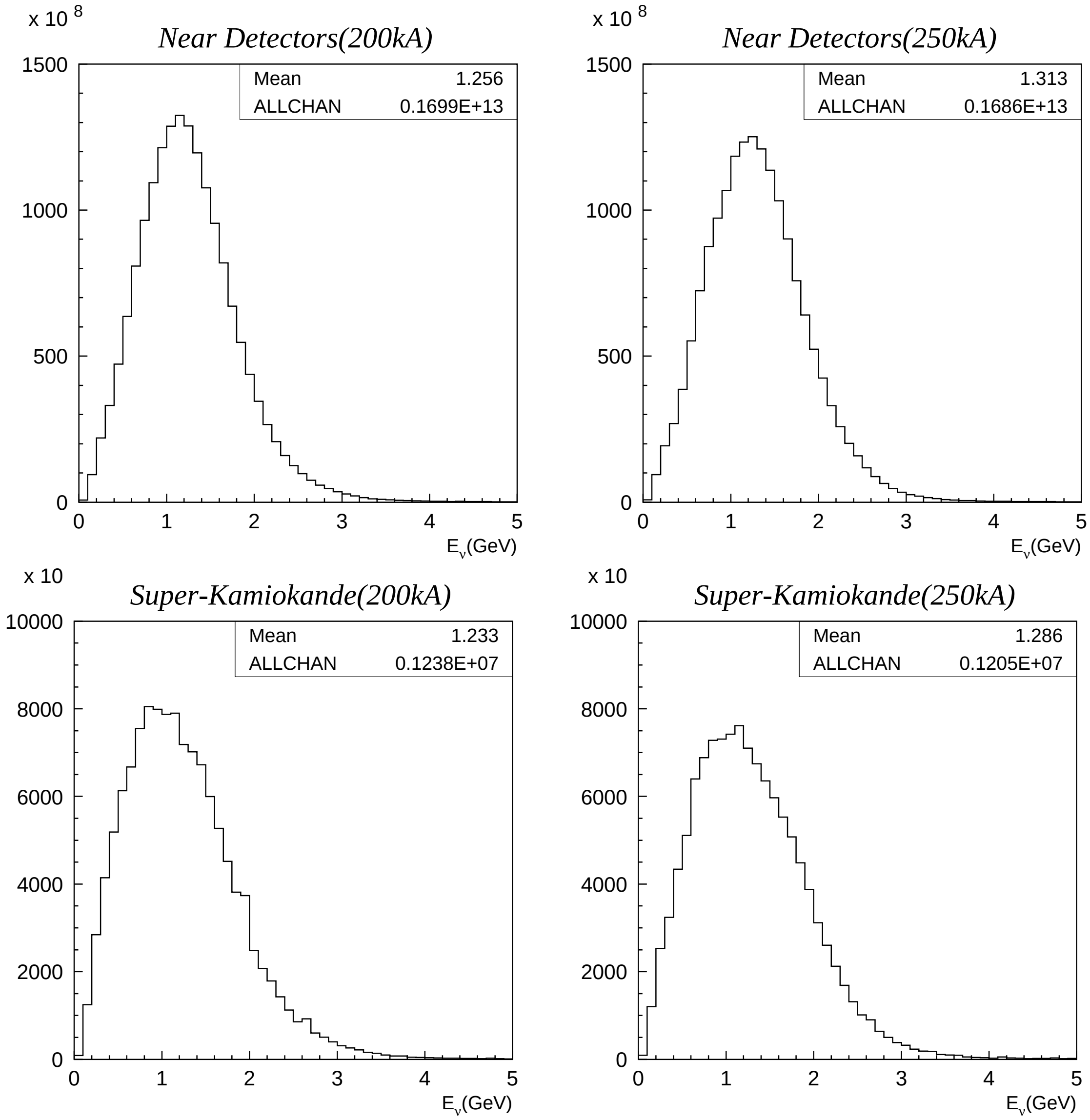

Figure A.6: Difference of ν_μ spectra. Left figures: spectra in June 1999 configuration, right figures: spectra since November 2000 configuration. Top figures: spectra at KEK, bottom figures: spectra in Super-Kamiokande. Unit of the Y-axis is number of neutrinos/cm^2/10^{20}P.O.T.

Appendix B

Simulation of Neutrino Interaction and Detector

Monte Carlo simulation of neutrino interaction and detector are briefly described in this chapter. These simulations are originally developed and used for atmospheric neutrino analysis in the Super-Kamiokande experiment [29].

B.1 Neutrino Interaction

Simulated neutrino flux is passed through a neutrino interaction simulator. Neutrino interacts with target material through charged current (CC) and neutral current (NC) weak interactions. Following interactions are simulated for ~ 1.3 GeV neutrino beam;

• CC quasi-elastic scattering	$\nu N \rightarrow l N'$	($\sim 27\%$)
• NC elastic scattering	$\nu N \rightarrow \nu N$	($\sim 12\%$)
• CC single-pion production	$\nu N \rightarrow l N' + \pi$	($\sim 28\%$)
• NC single-pion production	$\nu N \rightarrow \nu N' + \pi$	($\sim 10\%$)
• CC multi-pion production	$\nu N \rightarrow l N' + n\pi (n \geq 2)$	($\sim 14\%$)
• NC multi-pion production	$\nu N \rightarrow \nu N' + n\pi (n \geq 2)$	($\sim 4\%$)
• CC coherent-pion production	$\nu {}^{16}\mathrm{O} \rightarrow l {}^{16}\mathrm{O} + \pi^{\pm}$	($\sim 2\%$)
• NC coherent-pion production	$\nu {}^{16}\mathrm{O} \rightarrow \nu {}^{16}\mathrm{O} + \pi^{0}$	($\sim 1\%$)

where N is a nucleon and l is a charged lepton. The fraction of each interaction mode is shown at the end of each line. These values are for the expected flux at Super-Kamiokande interacting with water (H_2O).

The neutrino cross section with an orbital electron is neglected since it is roughly 1/1000 of above interactions.

B.1.1 Quasi-Elastic Scattering and Elastic Scattering Mode

The charged current quasi-elastic interaction is two-body scattering on a nucleon. Since the target nucleon has internal structure, vector and axial vector form factors are taken into account. The Q^2 (4-momentum transfer) dependence of the cross section can be expressed in terms of hadronic current [47]:

$$< N\prime | J_{had} | N >= \cos\theta_c \bar{u}(N\prime)\Big[\gamma_\lambda F_V^1(Q^2) + \frac{i\sigma_{\lambda\nu}q^\nu \xi F_V^2(Q^2)}{2M_N} + \gamma_\lambda\gamma_5 F_A(Q^2)\Big]u(N), \tag{B.1}$$

where θ_c is the Cabbibo angle, M_N is the nucleon mass. F_V^1,F_V^2,F_A are the vector and axial vector form factors represented as following:

$$F_V^1(Q^2) = \Big(1 + \frac{Q^2}{4M_N^2}\Big)^{-1}\Big[G_E^V(Q^2) + \frac{Q^2}{4M_N^2}G_M^V(Q^2)\Big], \tag{B.2}$$

$$\xi F_V^2(Q^2) = \Big(1 + \frac{Q^2}{4M_N^2}\Big)^{-1}\Big[G_M^V(Q^2) - G_E^V(Q^2)\Big], \tag{B.3}$$

$$G_E^V(Q^2) = \frac{1}{\Big(1 + \frac{Q^2}{M_V^2}\Big)^2}, \quad G_M^V(Q^2) = \frac{1+\xi}{\Big(1 + \frac{Q^2}{M_V^2}\Big)^2}, \quad \xi \equiv \mu_p - \mu_n = 3.71 \tag{B.4}$$

$$F_A(Q^2) = \frac{-1.23}{\Big(1 + \frac{Q^2}{M_A^2}\Big)^2}, \quad M_V = 0.84\mathrm{GeV/c}^2, \quad M_A = 1.01\mathrm{GeV/c}^2 \tag{B.5}$$

M_V and M_A represent the vector mass and the axial vector mass, respectively, which were determined by e-p and ν-p scattering experiments [48]. The uncertainty of M_A is 10%.

Finally the cross section is expressed as following:

$$\frac{d\sigma^\nu}{dQ^2} = \frac{M_N^2 G_F^2 \cos^2\theta_c}{8\pi E_\nu^2}\Big[A(Q^2) \mp B(Q^2)\frac{(s-u)}{M_N^2} + C(Q^2)\frac{(s-u)^2}{M_N^4}\Big] \tag{B.6}$$

where G_F is the Fermi coupling constant, $(s-u) = 4M_N E_\nu - Q^2 - M_l^2$, M_l is the lepton mass and;

$$\begin{aligned} A(Q^2) &= \frac{(M_l^2 + Q^2)}{4M_N^2}\Big[\Big(4 + \frac{Q^2}{M_N^2}\Big)|F_A|^2 - \Big(4 - \frac{Q^2}{M_N^2}\Big)|F_V^1|^2 + \frac{Q^2}{M_N^2}|\xi F_V^2|^2\Big(1 - \frac{Q^2}{4M_N^2}\Big) \\ &\quad + \frac{4Q^2 F_V^1 \xi F_V^2}{M_N^2} - \frac{M_l^2}{M_N^2}\Big(|F_V^1 + \xi F_V^2|^2 + |F_A|^2\Big)\Big], \end{aligned} \tag{B.7}$$

$$B(Q^2) = -\frac{Q^2}{M_N^2}F_A\Big(F_V^1 + \xi F_V^2\Big) \tag{B.8}$$

$$C(Q^2) = \frac{1}{4}\Big(|F_A|^2 + |F_V^1|^2 + \frac{Q^2}{M_N^2}|\frac{\xi F_V^2}{2}|^2\Big) \tag{B.9}$$

Figure B.1 shows the quasi-elastic cross section as a function of initial neutrino energy with $M_A = 1.01 \pm 0.10$ GeV/c^2. It gives a consistent result to various bubble chamber measurements around 1 GeV [49, 50, 51, 52].

Fermi motion and Pauli blocking effect are considered for target nucleons bounded in oxygen. Fermi gas model is adopted to simulate Pauli blocking by requiring the final nucleon momentum to be larger than Fermi surface momentum (217 MeV/c in ^{16}O). The Fermi momentum distribution is estimated from e-^{12}C scattering experiment [53].

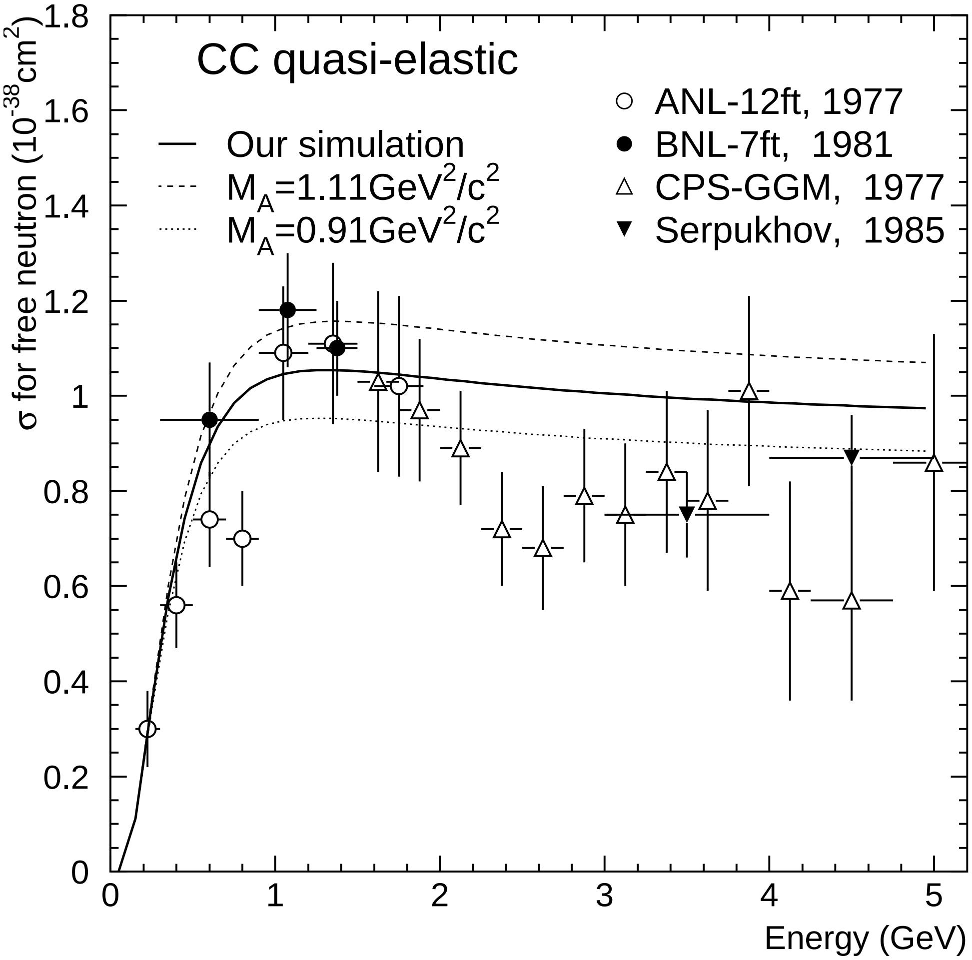

Figure B.1: Cross section of the CC quasi-elastic scattering. Solid line shows the standard simulation ($M_A = 1.01$ GeV/c^2) and dashed(dotted) line shows the simulation with $M_A = 1.11(0.91)$ GeV/c^2. Horizontal axis is the injected neutrino energy in Lab. frame. Various measurements (ANL:[49], BNL:[50], GGM:[51], and Serpukhov:[52]) are overlaid. Error bars are the errors quoted in papers.

The total cross section for the neutral current elastic scattering, most events of which are invisible with Water Čerenkov detector, is estimated by the following ratio of the NC to the CC cross section according to [54].

$$\begin{aligned}\sigma(\nu p \to \nu p) &= 0.153 \times \sigma(\nu n \to e^- p) &\text{(B.10)}\\ \sigma(\nu n \to \nu n) &= 1.5 \times \sigma(\nu p \to \nu p) &\text{(B.11)}\end{aligned}$$

B.1.2 Single-Pion Production

This interaction produces one lepton and one pion through following reactions:

- CC
  $\nu n \rightarrow l^- p \pi^0$
  $\nu n \rightarrow l^- n \pi^+$
  $\nu p \rightarrow l^- p \pi^+$
- NC
  $\nu n \rightarrow \nu n \pi^0$
  $\nu p \rightarrow \nu p \pi^0$
  $\nu n \rightarrow \nu p \pi^-$
  $\nu p \rightarrow \nu n \pi^+$

These interactions are simulated based on Rein-Sehgal's model [55]. The single-pion production is mediated by a baryon resonance states as;

$$\nu N \rightarrow l N^*$$
$$N^* \rightarrow N' \pi$$

where N^* is a baryon resonance state, for which $\Delta(1232)$ and other 17 higher resonance states below 2 GeV/c^2 are considered, including interferences among them. The differential cross section $d^2\sigma/dQ^2 dE_\nu$ is expressed as following:

$$\frac{d^2\sigma}{dQ^2 dE_\nu} = \frac{1}{32\pi M_N E_\nu^2} \cdot \frac{1}{2} \cdot \sum_{spins} |T(\nu N \rightarrow l N^*)|^2 \cdot \delta(W^2 - M^2) \tag{B.12}$$

where E_ν is the neutrino energy, M_N is the nucleon mass and W is the invariant mass of hadronic system. Figure B.2 shows calculated cross sections with the experimental data [56, 57, 58].

Angular distribution of pions from $\Delta(1232)$ is calculated using the Rein-Sehgal's method. For the decay of other resonance states, the pion direction is assumed to be isotropic in the resonance rest frame.

B.1.3 Multi-Pion Production

This interaction produces more than one pion with the invariant mass of hadronic system W to be greater than 1.3 GeV/c^2. The cross section of the CC multi-pion production is calculated

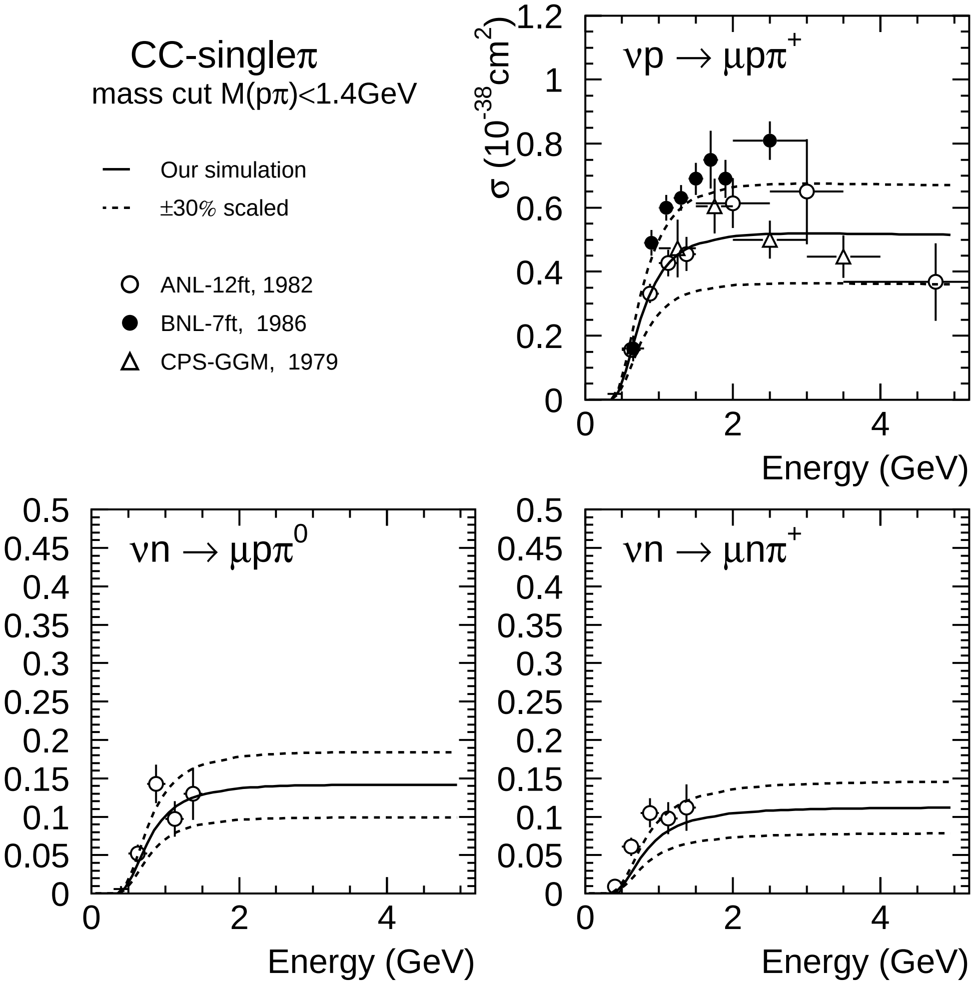

Figure B.2: Cross section for the CC single-pion production (solid line) with experimental data (ANL:[56], BNL:[57], GGM:[58]). Dashed lines are ±30% scaled ones.

based on Bjorken scaling, expressed as following:

$$\begin{aligned}
\frac{d^2\sigma^\nu}{dxdy} &= \frac{G_F^2 M_N E_\nu}{\pi} \cdot \Big[(1 - y + \frac{1}{2}y^2 + C_1)F_2(x) + y(1 - \frac{1}{2}y + C_2)[xF_3(x)]\Big] \qquad \text{(B.13)} \\
C_1 &= \frac{M_l^2(y-2)}{4M_N E_\nu x} - \frac{M_N xy}{2E_\nu} - \frac{M_l^2}{4E_\nu^2} \\
C_2 &= -\frac{M_l^2}{4M_N E_\nu x}
\end{aligned}$$

where $x = Q^2/(2M_N(E_\nu - E_l) + M_N^2)$ and $y = (E_\nu - E_l)/E_\nu$ are the Bjorken scaling variables, M_N, M_l, E_ν and E_l are nucleon mass, lepton mass, initial neutrino energy and final lepton energy, respectively. The nucleon structure functions, F_2 and xF_3, are given by GRV-94[59].

The multiplicity of pion is calculated from the measurement at Fermilab 15-foot bubble chamber experiment [60], which is found to be $(0.06 \pm 0.06) + (1.22 \pm 0.03)lnW^2$. The averaged pion multiplicity including neutral pion are estimated by assuming $\langle n_{\pi^+}\rangle = \langle n_{\pi^-}\rangle = \langle n_{\pi^0}\rangle = 1/2\langle n_c\rangle$ as following:

$$\langle n_\pi \rangle = 0.09 + 1.83 lnW^2 \qquad \text{(B.14)}$$

The number of pions for each event is determined using KNO(Koba-Nielsen-Olesen) scaling [61]. To keep consistency with single-pion mode, the number of produced pion is required to be greater than or equal to 2 in $W < 2$ GeV/c^2 region. The charge of each hadron is randomly chosen under the charge conservation. The effect of Δ resonance in the final state is considered since a bubble chamber experiment at Argonne clearly shows a signal of Δ in multi-hadron final states [62]. The forward-backward asymmetry of pion multiplicity is also taken into account to be [63];

$$\frac{\langle n_\pi^F \rangle}{\langle n_\pi^B \rangle} = \frac{0.35 + 0.41 lnW^2}{0.50 + 0.09 lnW^2} \qquad \text{(B.15)}$$

For the NC multi-pion production, ratio of NC/CC is estimated from results shown in [64, 65]:

$$\frac{\sigma(NC)}{\sigma(CC)} = \begin{cases} 0.26 & (E_\nu < 3 \text{ GeV}) \\ 0.26 + 0.04(E_\nu/3 - 1) & (3 \text{ GeV} < E_\nu < 6 \text{ GeV}) \\ 0.30 & (6 \text{ GeV} < E_\nu) \end{cases} \qquad \text{(B.16)}$$

For events with $W > 2$ GeV/c^2, kinematics are determined by JETSET/PYTHIA [66].

B.1.4 Coherent Pion Production

In this interaction, a neutrino interacts with a nucleus as a whole instead of individual nucleon, without any change of charge or isospin for recoil nucleus. Angular distribution of recoil lepton is sharply peaked in the forward direction and the nucleus does not break up due to the small momentum transfer.

The cross section calculation for oxygen nucleus is based on Rein-Sehgal model [67]:

$$\begin{aligned}
\frac{d^3\sigma}{dxdyd|t|} &= \frac{G_F^2 M_N E_\nu}{2\pi^2} f_\pi^2 A^2 (1-y) \frac{1}{16\pi} \Big[\sigma_{tot}^{\pi N}\Big]^2 (1 + r^2) \Big(\frac{M_A^2}{M_A^2 + Q^2}\Big)^2 e^{-b|t|} F_{abs}, \qquad \text{(B.17)} \\
r &= \frac{Ref_{\pi N}(0)}{Imf_{\pi N}(0)}
\end{aligned}$$

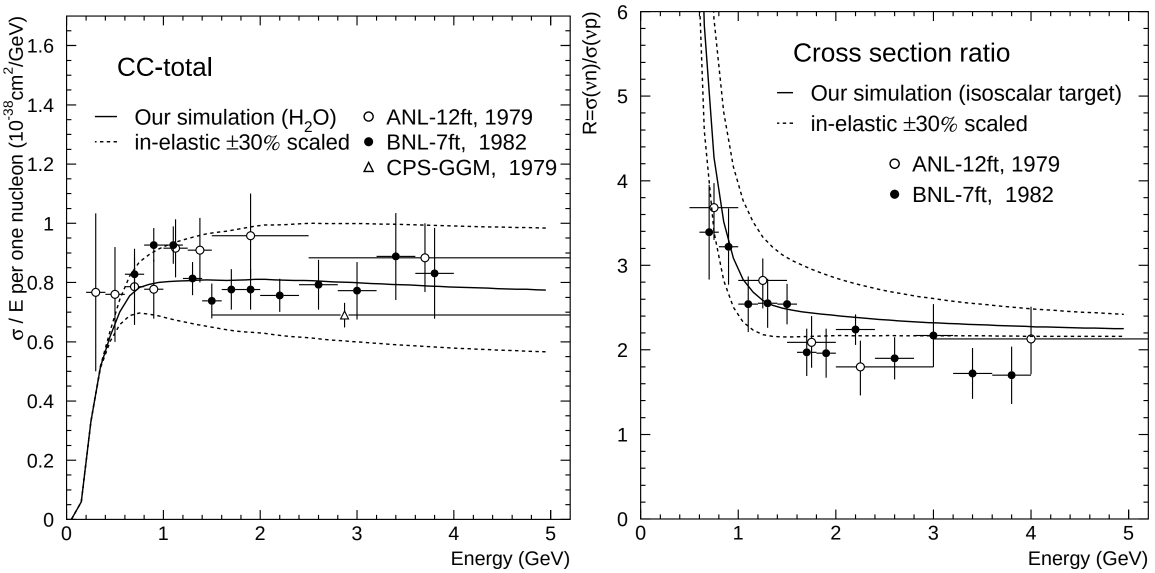

Figure B.3: σ(CC-total)$/E_\nu$ (left) and $\sigma(\nu n)/\sigma(\nu p)$ (right) as a function of the neutrino energy. Their absolute values are normalized to water (H_2O). Various Measurements (ANL: [62], BNL: [68], GGM: [69]) are overlaid. Dotted lines are the cases for weighted inelastic cross sections by ±30%.

where t is square of 4-momentum transfer to the nucleus, $f_\pi = 0.93 m_\pi$ is the decay constant, A is atomic number ($A = 16$ for oxygen) and $b = \frac{1}{3}(R_0 A^{1/3})^2$ is of the order of traverse dimensions of the nucleus. F_{abs} is t-independent term for pion absorption in the nucleus.

B.1.5 Experimental Constraint of the CC Total Cross Section

The CC total cross section is compared with bubble chamber measurements [62, 68, 69]. Figure B.3 shows the CC total cross section and $\sigma(\nu n)/\sigma(\nu p)$ ratio. In these figures, cross sections are corrected to the water target by the ratio of proton and neutron while coherent interaction is neglected. Most of the experimental data are covered if the inelastic (single pion production and multi pion production) cross sections scaled by ±30%.

B.1.6 Nuclear Effect for Hadrons

Hadrons produced in a ^{16}O nucleus often make secondary interactions before leaving the nucleus. Interaction for pion and Δ are considered in the simulation. Nuclear effect for proton, neutron and lepton are no considered.

- **Nuclear effect for pion**
  Considered nuclear interactions for pion are: inelastic scattering, charge exchange and absorption. The interaction position (r) of a neutrino, and the production position of the

pion, in the ^{16}O nucleus is calculated using Wood-Saxon type density distribution:

$$\rho_p(r) \quad = \quad \frac{Z}{A}\bar{\rho}\left\{1+\exp(\frac{r-c}{a})\right\}^{-1} \tag{B.18}$$

where A is the atomic number, Z is the number of protons in nucleus, $\bar{\rho} = 0.48m_\pi^3$ is the average density, $a = 0.41$ fm and $c = 2.69$ fm are density parameters of nucleus.

Each cross section is calculated by Oset model [70]. Fremi motion of nucleons and Pauli blocking effect are taken into account.

- **Nuclear effect for Δ**
  The absorption of Δ is taken into account. Its probability is estimated to be 20% [71].

B.2 Detector Simulation

Simulated kinematics of neutrino interaction are taken over by a detector simulation program based on GEANT [35]. The same water Čerenkov detector simulation is used at Super-Kamiokande and the 1kt detector. It simulates the propagation of particles, Čerenkov radiation, propagation of Čerenkov photons in water, the response of PMTs and electronics.

CALOR [33] program is used for the hadronic interaction in water. For energy range of $E_\pi < 500$ MeV in which CALOR does not reproduces experimental data well, a custom hadron simulator, which uses cross sections estimated from the experimental data of π-^{1}2C scattering [72] and π-p scattering [73], is developed.

Čerenkov photons are generated according to Equation 4.1 and 4.2, and traced until detected by a PMT or absorbed. Reflection of Čerenkov photons at the black sheet on the detector wall and at the surface of the PMT are considered as a function of the incident angle [29]. For Čerenkov photon attenuation, Rayleigh scattering, Mie scattering and absorption are taken into account. Figure 4.14 shows the attenuation length of Čerenkov photon as a function of wavelength.

For simulating PMT response in photon detection, measured quantum efficiency shown in Figure 4.4 is used. The signal from the PMT, which is smeared according to the measured single p.e. distribution and timing resolution, are finally converted to TDC and ADC information.

Appendix C

Event Reconstruction

C.1 Outline

In Super-Kamiokande and the 1kt detector, selected events are reconstructed by following procedures:

1 TDC-fit
TDC-fit reconstructs the vertex point and direction using hit time (TDC) information of inner PMTs.

2 Ring counting
The number of Čerenkov ring is estimated.

3 Particle identification
Each Čerenkov ring is distinguished between showering type (electron-like) and non-showering type (muon-like).

4 MS-fit
For an event identified as single-ring in the second step, a more precise fitter using particle type information, is applied.

5 Momentum determination
The momentum of each particle is estimated from the intensity of the Čerenkov light.

C.2 TDC-Fit

TDC-fit reconstructs the vertex point and direction using hit time (TDC) information of inner PMTs. The principle of the TDC-fit is to search for a position where timing residuals of all the hit PMTs are equal. The timing residual t_i of the $i-$th hit PMT is defined as following:

$$t_i = t_i^0 - \frac{n}{c} \times |\vec{P}_i - \vec{O}|$$

where t_i^0 is the hit time of the $i-$th PMT, n is the refractive index of water, c is the light velocity, $\vec{P}_i$ is the position of the $i-$th PMT and $\vec{O}$ is the assumed position of the vertex. The timing residuals are expected to have a common value in entire hit PMTs if all the Čerenkov photons are emitted at the vertex position and if Čerenkov photons are not scattered.

TDC-fit consists of following three steps;

1 ”point fit”, which searches a rough vertex from only the timing information of PMTs,

2 ”ring edge search”, which searches the direction and opening angle of the Čerenkov cone produced by the most energetic charged particle,

3 ”fine vertex fit”, which determines more precise vertex by taking account of the track length of the charged particle.

The second and third steps are iterated until the distance between the previous vertex and the latest one becomes less than 50 cm.

C.2.1 Point Fit

Point fit searches for a position where the timing residual of all the hit PMTs are approximately equal. An estimator G_p is used as a goodness of the point fit:

$$G_p = \frac{1}{N_{hit}} \sum_i \exp\left(-\frac{1}{2}\left(\frac{t_i - t_0}{1.5\sigma}\right)^2\right) \tag{C.1}$$

where N_{hit} is the number of hit PMTs in the inner detector, σ is a typical time resolution of a PMT (2.5 nsec) and t_0 is an offset value of the time residual which is adjusted so that G_p takes the maximum value. The factor 1.5 in the denominator is chosen to optimize the fitter performance. By changing the estimated vector $\vec{O}$, the point fit searches the vertex position $\vec{O}_0$ where G_p is the maximum.

C.2.2 Ring Edge Search

In this step, the edge of the Čerenkov ring is estimated using the angular distribution of p.e.s, $PE(\theta)$, as a function of opening angle θ between the particle direction $\vec{d_p}$ and each hit PMT. The particle direction $\vec{d_p}$ is calculated from the weighted average of observed p.e.s:

$$\vec{d_p} = \sum_i q_i \frac{\vec{P_i} - \vec{O_0}}{|\vec{P_i} - \vec{O_0}|}. \tag{C.2}$$

where q_i is the p.e.s of the i-th hit PMT. Figure C.1 shows the $PE(\theta)$ distribution. The Čerenkov ring edge is obtained at the nearest zero-crossing point of $d^2PE(\theta)/d\theta^2$ outer than the peak of $PE(\theta)$.

To determine the ring direction, an estimator Q is defined as following:

$$Q\left(\theta_{edge}\right) = \frac{\int_0^{\theta_{edge}} PE(\theta)d\theta}{\sin\theta_{edge}} \cdot \left(\left|\frac{dPE(\theta)}{d\theta}\right|_{\theta_{edge}}\right)^2 \cdot \exp\left(-\frac{(\theta_{edge} - \theta_C)^2}{2\sigma_\theta^2}\right) \tag{C.3}$$

where θ_C is the Čerenkov angle expected from the total charge in the cone, and σ_θ is its resolution. Q is maximized by changing the particle direction $\vec{d_p}$.

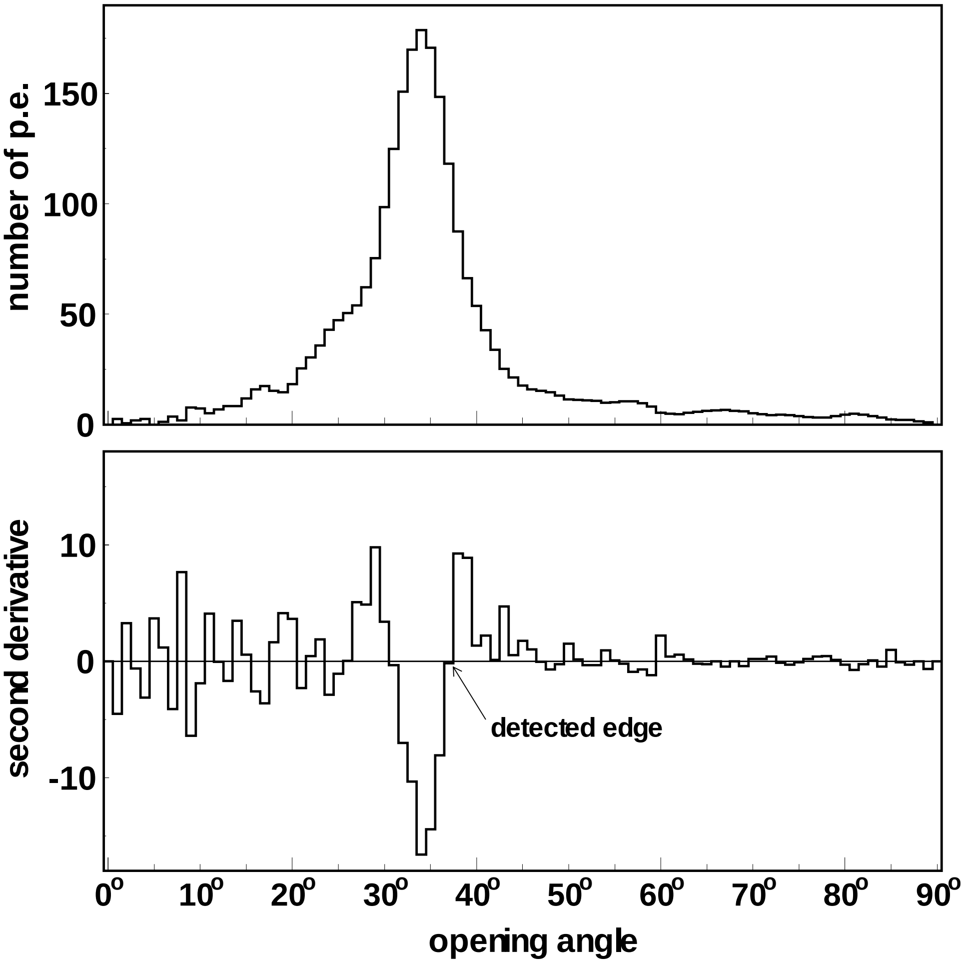

Figure C.1: Effective charge $PE(\theta)$ distribution (upper) and its second deviation (lower), as functions of opening angle θ.

C.2.3 Fine Vertex Fit

The final step is a fine vertex fitting using the results of previous steps. The timing residual t_i for the PMTs are re-calculated by taking account of the particle velocity, which is assumed to be the light velocity, and position along the track where Čerenkov photons are emitted. It is calculated as:

$$t_i = \begin{cases} t_i^0 - \frac{1}{c} \cdot |\vec{X}_i - \vec{O}| - \frac{n}{c} \cdot |\vec{P}_i - \vec{O}| & \text{PMTs inside of the Čerenkov edge,} \\ t_i^0 - \frac{1}{c} \cdot |\vec{X}_i - \vec{O}| & \text{PMTs outside of the Čerenkov edge,} \end{cases} \tag{C.4}$$

where $\vec{X}_i$ is the estimated point where Čerenkov photons are emitted to the $i-$th PMT.

Three estimators, G_I, G_{O_1} and G_{O_2}, are calculated in this step. G_I is for PMTs inside of the Čerenkov edge, defined as following:

$$G_I = \sum_i \frac{1}{\sigma_i^2} \exp\left(-\frac{1}{2} \left(\frac{t_i - t_0}{1.5\sigma} \right)^2 \right), \tag{C.5}$$

where σ_i is the timing resolution of the $i-$th PMT as a function of q_i and σ is the timing resolution averaged over all the hit PMTs.

G_{O_1} and G_{O_2} are for PMTs outside of the Čerenkov edge, with consideration of the scattered lights;

$$\begin{aligned} G_{O_1} &= \sum_i \frac{1}{\sigma_i^2} \left\{ \max \left[\exp\left(-\frac{1}{2} \left(\frac{t_i - t_0}{1.5\sigma} \right)^2 \right), G_{\text{scat}}(t_i, t_0) \right] \cdot 2 - 1 \right\}, \quad (\text{for } t_i > t_0 \text{ PMTs }) \\ G_{O_2} &= \sum_i \frac{1}{\sigma_i^2} \left\{ \exp\left(-\frac{1}{2} \left(\frac{t_i - t_0}{1.5\sigma} \right)^2 \right) \cdot 2 - 1 \right\}, \quad (\text{for } t_i \leq t_0 \text{ PMTs }) \end{aligned} \tag{C.6}$$

where

$$G_{\text{scat}}(t_i, t_0) = \frac{R_q}{1.5^2} \exp\left(-\frac{1}{2} \left(\frac{t_i - t_0}{1.5\sigma} \right)^2 \right) + \left(1 - \frac{R_q}{1.5^2} \right) \exp\left(-\frac{t_i - t_0}{T_l} \right). \tag{C.7}$$

T_l is the typical timing delay of scattered photons, estimated by a Monte Carlo simulation, and set to be 60 nsec. R_q is a fractional p.e.s detected within the Čerenkov ring;

$$R_q = \frac{\sum_{\theta < \theta_c + 3^\circ} q_i}{\sum_{\theta < 70^\circ} q_i}. \tag{C.8}$$

Finally, a fitting estimator G_T is defined by summing up those estimators:

$$G_T = \frac{G_I + G_{O_1} + G_{O_2}}{\sum_i \frac{1}{\sigma_i^2}} \tag{C.9}$$

These procedures are iterated several times until both the vertex position and the direction are determined at the maximum G_T.

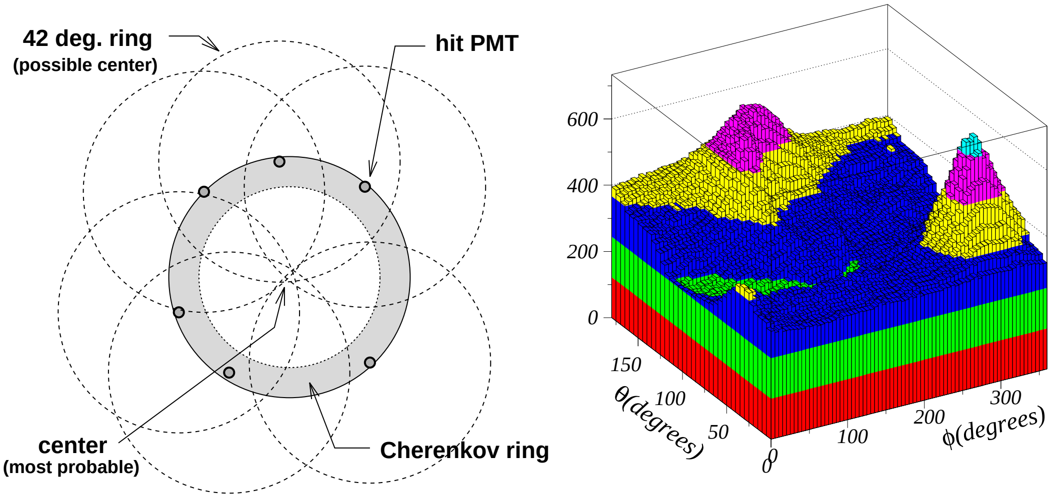

Figure C.2: Schematic view of the ring counting. Left figure shows the basic concept of the search for the center of a Čerenkov ring. The most overlapping point is the candidate of the center. Right figure shows the (Θ, Φ) map for a typical two ring event. Two peaks correspond to the directions of Čerenkov rings.

C.3 Ring Counting

After reconstructing the vertex position and the most energetic Čerenkov ring direction by the TDC-fit, a ring counting program finds and reconstructs the other possible rings. Figure C.2 shows the basic concept to find Čerenkov ring candidates. The image of the Čerenkov ring is projected to a plane perpendicular to the particle direction. The ring counting program picks up hit PMTs and draws circles at each hit PMT with opening angle of 42°. The most overlapping point is estimated to be the center of the ring.

Practically, a two dimensional p.e.s map of polar angle Θ and azimuthal angle Φ from the vertex (36×72 bins) is used. First of all, expected p.e.s of the Čerenkov ring which were already found is subtracted for each PMT. Instead of drawing a circle, the residual p.e.s are mapped to the (Θ, Φ) map with a weight function $f_e(\theta)$, which is an expected angular distribution of p.e.s for a Čerenkov ring generated by a 500 MeV/c electron. θ is the opening angle from the ring direction to the hit PMT. A typical (Θ, Φ) map is shown in Figure C.2. In this figure, the p.e.s of the first ring are not subtracted.

Each ring candidate found in the map are check by a likelihood method to determine whether the ring is probable or not. The test for the $(N + 1)$-th ring is performed by comparing the likelihood for $(N + 1)$ rings assumption and that of N rings. The ring counting procedure is iterated until no more candidate is found.

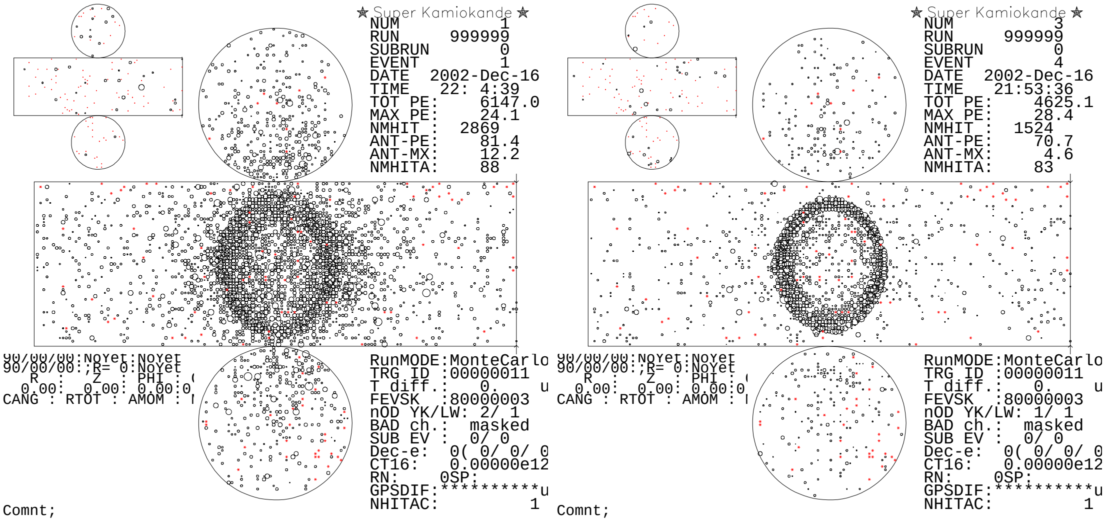

Figure C.3: Typical Čerenkov ring image for an electron (left) and a muon (right), shown in the exploded view of the cylindrical tank. The ring produced by the electron is diffused while the ring produced by the muon have sharp edge. These events are generated by a Monte Carlo simulation. An electron (muon) with momentum of 700 MeV/c is injected horizontally from the center of the detector.

C.4 Particle Identification

A particle identification program determines the particle type of each ring using its Čerenkov ring pattern and opening angle of the cone. Each Čerenkov ring is classified as a showering particle (electron-like) or a non-showering type (muon-like).

Čerenkov rings produced by electrons are diffused due to the electromagnetic shower and multiple scattering, while those produced by muons are characterized by their sharpness of the ring edge because muons propagate in water with a simple dE/dx energy loss (Figure C.3). The opening angle is important for the identification of low energy muons because the opening angle and the particle velocity are related (Equation4.1).

The observed p.e.s for each PMT is compared with expectation for electron assumption and for muon assumption. One of two particle types which better reproduces the observed p.e.s is selected as a reconstructed particle type.

C.5 MS-Fit

The vertex fitter described in Section C.2 uses mainly timing information. It has a relatively poor vertex resolution along the ring direction for the single-ring event, because the change in time residuals of the PMTs are almost equal when the vertex position shifts along the direction.

The vertex position of single ring events are improved by a vertex fitter called "MS-Fit". It uses not only the timing information but also the Čerenkov ring pattern information. The ob-

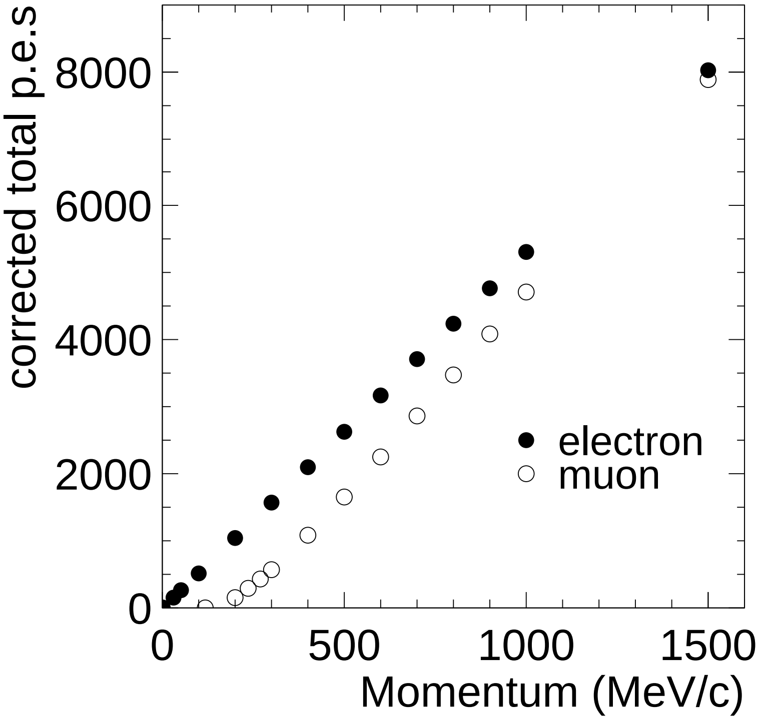

Figure C.4: The relation between corrected total p.e.s and the momentum for muon and electron.

served Čerenkov ring pattern is compared to the expectation calculated according to its particle type determined by the particle identification program. The vertex position is selected where the expectation most reproduces the observation.

C.6 Momentum Determination

The momentum is estimated from the total number of p.e.s detected within 70° half opening angle towards the reconstructed ring direction.

The observed p.e.s of each PMT is corrected for attenuation length, scattered photons, PMT acceptance and gain. In the cases of muon-like event, muon track length is taken into account for the calculation of photon flight length. A timing cut is applied to eliminate the effect of possible muon-decay electrons. The timewindow is set to be -50 to 250 nsec from the peak of the timing residual.

The relation between the corrected total number of p.e.s and the momentum of particles are estimated from a Monte Carlo simulation (Figure C.4).

Bibliography

[1] S.L. Glashow, Nucl. Phys. **22**, 579 (1961).

[2] S. Weinberg, Phys. Rev. Lett. **19**, 1264 (1961).

[3] A. Salam, “Elementary particle physics”, Nobel Symp. No.8

[4] Particle Data Group, Eur. Phys. J. **C15**, 1-878 (2000), and http://pdg.lbl.gov/.

[5] K. Assamagan *et al.*, Phys. Rev. **D53**, 6065 (1996).

[6] Y. Fukuda *et al.*, Phys. Lett. **B335**, 237 (1994).

[7] R.Becker-Szendy *et al.*, Phys. Rev. **D46**, 3720 (1992).

[8] T.Kajita for the Super-Kamiokande Collaboration, Nucl. Phys. Proc. Suppl. **77**, 123 (1999).

[9] K. Daum *et al.*, Z. Phys. **C66** 417 (1995).

[10] M. Aglietta *et al.*, Europhys. Lett. **8**, 611 (1989).

[11] W. W. M. Allison *et al.*, Phys. Lett. **B449**, 137 (1999).

[12] M. Ishitsuka for the Super-Kamiokande Collaboration, *Proceeding of the XVI International Conference on Particles and Nuclei*, to be published.

[13] The Super-Kamiokande Collaboration, Phys. Rev. Lett. **86**, 5651 (2001); Phys. Rev. Lett. **86**, 5656 (2001); Phys. Rev. Lett. **82**, 2430 (1999).

[14] H. Noumi *et al.*, Nucl. Instrum. Meth. **A398**, 399 (1997).

[15] T. Maruyama, Ph.D thesis of Tohoku University (2000), unpublished.

[16] K. Nishikawa *et al.*, ”Proposal for a Long Baseline Neutrino Oscillation experiment, using KEK-PS and Super-Kamiokande” KEK-PS proposal (E362) (1995).

[17] M. Kohama, Master thesis of Kobe University (1997), unpublished, in Japanese.

[18] Y. Yamanoi *et al.*, KEK preprint 97-225; Y. Yamanoi *et al.*, KEK preprint 99-178.

[19] T. Inagaki, Master thesis of University of Tokyo (1998), unpublished, in Japanese.

[20] HAMAMATSU PHOTONICS K.K. "PHOTOMULTIPLIER TUBE -principle to application-".

[21] Y. Kobayashi, Master thesis of University of Tokyo (1999), unpublished, in Japanese.

[22] A. Suzuki *et al.*, Nucl. Instr. and Meth. **A453**, 165 (2000).

[23] T. Ishii *et. al.*, Nucl. Inst. and Meth. **A482** 244 (2002).

[24] Y. Asano *et al.*, Nucl. Instr. and Meth. **A259**, 430 (1987). Y. Ikegami *et al.*,

[25] Y. Hayato *et. al.*, Phys. Rev. Lett. **83**, 1529 (1999); M. Shiozawa *et. al.*, Phys. Rev. Lett. **81**, 3319 (1998).

[26] A. Suzuki *et al.*, Nucl. Inst. and Meth. **A329**, 299 (1993).

[27] KEK Data Acquisition Development Working Group, "TKO Specification", KEK Report 85-10 (1985).

[28] T.Tanimori, H.Ikeda, M.Mori, K.Kihara, H.Kitagawa and Y.Haren, IEEE Trans. Nucl. Sci., bf NS-36, 497 (1989).

[29] M. Shiozawa, Ph.D thesis of University of Tokyo (1999), unpublished ; K. Ishihara, Ph.D thesis of University of Tokyo (1999), unpublished ; K. Okumura, Ph.D thesis of University of Tokyo (1999), unpublished.

[30] M. Nakahata *et al.*, Nucl. Instr. and Meth. **A421** 113 (1999).

[31] A. Shima, Master thesis of Kyoto University (2001), unpublished, in Japanese.

[32] T. Inagaki, Ph.D thesis of Kyoto University (2001), unpublished.

[33] T. A. Gabriel, J. D. Amburgey and B. L. Bishop, "'Calor': A Monte Carlo Program Package For The Design And Analysis Of Calorimeter Systems" ORNL/TM-5619.

[34] A. Ferrari and P.R. Sala, "A new model for hadronic interactions at intermediate energies for the FLUKA code," *In *Tallahassee 1993, Monte Carlo simulation in high energy and nuclear physics* 277-288.*

[35] GEANT–Detector Description and Simulation Tool, Application Software Group, Computing and Networks Division (1993).

[36] J. R. Sanford and C. L. Wang, Brookhaven National Laboratory, AGS internal report, 1967 (unpublished); C. L. Wang, Phys. Rev. Letters **25** 1068 (1970); C. L. Wang, Phys. Rev. **D16** 2196 (1977).

[37] R. A. Lundy *et al.*, Phys. Rev. Lett. **14** 504 (1966).

[38] D. Dekkers *et al.*, Phys. Rev. **137** B962 (1965).

[39] W.F. Baker *et al.*, Phys. Rev. Lett.**7** 101 (1961).

[40] A. Yamamoto, "Study On Low-Energy Intense Kaon Beam," KEK 81-13.

[41] Y. Cho *et al.*, Phys. Rev. **D 4** 1967 (1971).

[42] J. G. Asbury etal, Phys. Rev. **178** 2086 (1969).

[43] G. J. Marmer *et al.*, Phys. Rev. **179** 1294 (1969).

[44] G. J. Marmer *et al.*, Phys. Rev. **D 3** 1089 (1971).

[45] J. V. Allaby *et al.*, CERN Report No. CERN-TH-70-12 (unpablished).

[46] M. Nakahata *et al.*[KAMIOKANDE Collaboration], J. Phys. Soc. Jap. **55**, 3786 (1986).

[47] C. H. L. Smith, Phys. Rep. **3C**, 261 (1972).

[48] K. L. Miller *et al.*, Phys. Rev. **D26**, 537 (1982).

[49] S. J. Barish *et al.*, Phys. Rev. **D16**, 3103 (1977).

[50] N. J. Baker *et al.*, Phys. Rev. **D23**, 2499 (1981).

[51] S. Bonetti *et al.*, Nuovo Cimento **A38**, 260 (1977).

[52] S. V. Belikov *et al.*, Z. Phys. **A320**, 625 (1985).

[53] F. A. Brieva and A. Dellafiore, Nucl. Phys. **A292**, 445 (1977).

[54] K. Abe *et al.*, Phys. Rev. Lett. **56**, 1107 (1986) ; C. H. Albright *et al.*, Phys. Rev. **D14**, 1780 (1976).

[55] D. Rein and L. M. Sehgal, Ann. of Phys. **133**, 79 (1981); D. Rein, Z. Phys. **C35**, 43 (1987).

[56] G. M. Radecky *et al.*, Phys. Rev. **D25**, 1161 (1982).

[57] T. Kitagaki *et al.*, Phys. Rev. **D34**, 2554 (1986).

[58] M. Pohl *et al.*, Lett. al Nuovo Cimento **24**, 540 (1979).

[59] M. Glück, E. Reya, and A. Vogt, Z. Phys. **C67**, 433 (1995).

[60] S. J. Barish *et al.*, Phys. Rev. **D17**, 1 (1978).

[61] H. Sarikko, *Proc. of the NEUTRINO'79*, 507 (1979).

[62] S. J. Barish *et al.*, Phys. Rev. **D19** 2521 (1979).

[63] S. Barlag, *et. al.*, Z. Phys. **C11**, 283 (1982).

[64] P. Musset and J. P. Vialle, Phys. Rep. **C39**, 1 (1978).

[65] J. E. Kim *et al.*, Rev. Mod. Phys. **53**, 211 (1981).

[66] T. Sjöstrand *et al.*, CERN-TH-7112-93 (1994).

[67] D. Rein and L. M. Sehgal, Nucl. Phys. **B223**, 29 (1983) ; P. Marage *et al.*, Z. Phys. **C31**, 191 (1986).

[68] N. J. Baker *et al.*, Phys. Rev. **D25**, 617 (1982).

[69] S. Ciampolillo *et al.*, Phys. Lett. **84B**, 281 (1979).

[70] L. L. Salcedo, E. Oset *et. al.*, Nucl. Phys. **A484**, 557 (1988).

[71] T. S. Kosmas and E. Oset, Phys. Rev. **C53**, 1409 (1996).

[72] A.S.Carrol *et al.*, Phys. Rev. **C14** 635 (1976).

[73] E.Bracci *et al.*, CERN/HERA 72-1 (1972).

List of Figures

List of Tables